TWO STAGGERED SURFACE-MOUNTED FINITE-HEIGHT CYLINDERS IN A CROSS-FLOW

A Thesis Submitted to the College of
Graduate and Postdoctoral Studies
In Partial Fulfillment of the Requirements
For the Degree of Master of Science
In the Department of Mechanical Engineering
University of Saskatchewan

By

Hayden K Reitenbach

Permission of Use

In presenting this thesis in partial fulfillment of the requirements for a Postgraduate degree from the University of Saskatchewan, I agree that the Libraries of this University may make it freely available for inspection. I further agree that permission for copying of this thesis in any manner, in whole or in part, for scholarly purposes may be granted by the professor who supervised my thesis work or, in his absence, by the Head of the Department or the Dean of the College in which my thesis work was done. It is understood that any copying or publication or use of this thesis or parts thereof for financial gain shall not be allowed without my written permission. It is also understood that due recognition shall be given to me and to the University of Saskatchewan in any scholarly use which may be made of any material in my thesis.

DISCLAIMER

Reference in this thesis to any specific commercial products, process, or service by trade name, trademark, manufacturer, or otherwise, does not constitute or imply its endorsement, recommendation, or favoring by the University of Saskatchewan. The views and opinions of the author expressed herein do not state or reflect those of the University of Saskatchewan, and shall not be used for advertising or product endorsement purposes.

Requests for permission to copy or to make other uses of materials in this thesis in whole or part should be addressed to:

Head of the Department of Mechanical Engineering
University of Saskatchewan
57 Campus Drive
Saskatoon, Saskatchewan S7N 5A9
Canada

Dean of the College of Graduate and Postdoctoral Studies
University of Saskatchewan
110 Science Place
Saskatoon, Saskatchewan S7N 5C9
Canada

Abstract

Two surface-mounted finite-height cylinders in a staggered configuration immersed in a cross-flow can be used to represent a broad variety of engineering applications. The centre-to-centre pitch ratio, P/D, incidence angle, α, and Reynolds number, Re, are known to strongly influence the aerodynamic loading on the cylinders and vortex shedding, however the effects of cylinder aspect ratio, AR (= height/diameter) and the boundary layer thickness on the ground plane, δ/D, are not yet well understood. Most studies of the flow around two surface-mounted finite-height cylinders have focused on two main configurations, tandem ($\alpha = 0°$) and side-by-side ($\alpha = 90°$).

In the present research, the flow around two finite cylinders in a staggered configuration was systematically studied, to better understand the effects of the cylinder aspect ratio. Wind tunnel experiments were conducted at $Re = 6.5\times10^4$ with a relative boundary layer thickness of $\delta/D = 1.4$ for cylinders of AR = 9, 7, 5, and 3. The pitch ratio was varied from $1.125 \leq P/D \leq 4.5$ in 12 discrete steps and the incidence angle was varied from $0° \leq \alpha \leq 90°$ in small increments. Of specific interest were the effects of AR on the mean drag coefficient, C_D, mean lift coefficient, C_L, and Strouhal number, St, experienced by the upstream and downstream cylinders in each staggered configuration, and any differences between the behaviour of two finite cylinders compared to more extensively studied case of two infinite (two-dimensional) cylinders.

The results for the two finite cylinders in tandem showed a relatively smooth transition from the reattachment flow pattern to the co-shedding flow pattern, in contrast to what is seen for two infinite cylinders. A reduced range of P/D was found where the downstream cylinder experienced a thrust force. These changes were attributed to downwash entering the gap between the cylinders and impinging on the downstream cylinder.

For the side-by-side configuration, the biased flow pattern continued to be observed for two finite cylinders, but the proximity interference effects were strengthened compared to two infinite cylinders. For closely spaced finite cylinders ($P/D \leq 1.75$) near $\alpha = 90°$, hysteresis was found over a small range of incidence angle where C_D and C_L could attain different values depending on whether α was incremented positive or negative. At the upper and lower ends of this range of incidence angle, a sudden change in the wake state and the values of C_D and C_L occurred. Many aspects of the hysteresis were found to be complex functions of AR and P/D.

For the staggered configuration, the behaviours of C_D, C_L, and St were found to be complex functions of P/D, α, and AR. In many cases, but not all, the general effect of reducing aspect ratio was to weaken the wake and proximity interference effects. The data for the two cylinders of AR = 3 behaved distinctly from those of AR = 9, 7, and 5, which showed that these cylinders were less than the critical aspect ratio.

Acknowledgements

The author would like to thank his supervisor, Dr. David Sumner, for his motivation, direction, and encouragement throughout the author's entire post-secondary education. Your abundant knowledge, curiosity, and enthusiasm in the fascinating realm of fluid mechanics is a constant inspiration to those you work with.

The author would also like to thank Shawn Reinink for his problem solving and technical ability with the entirety of the experimental apparatus, as well as Rob Peace for his knowledge and assistance in machining. Further thanks to Engineering Shops for their expertise in the design and construction of the cylinder models. Additional acknowledgement to the author's advisory committee, Dr. Jim Bugg and Dr. Donald Bergstrom, for their guidance in the initial stages of the research program.

A thank you is also offered to the students in the author's research group, Adam Beitel, Obiora Ugo-Okeke, and Herman Heng, for their assistance in the experiments and the analysis of the data as well as the author's girlfriend Kylie Gerwing, his friends, and his family for their support throughout his post-secondary education.

A final acknowledgement to the Department of Mechanical Engineering at the University of Saskatchewan, Dr. David Sumner, and the Natural Sciences and Engineering Research Council of Canada (NSERC) for their financial assistance throughout the author's M.Sc. program.

Table of Contents

List of Symbols

English Symbols

AR	Aspect ratio, H/D
C_D	Mean drag force coefficient
C_L	Mean lift force coefficient
C_{MP}	Mean pitching moment coefficient
C_{MR}	Mean rolling moment coefficient
C_{MY}	Mean yawing (bending) moment coefficient
C_N	Mean wall-normal force coefficient
D	Cylinder diameter [m]
f	Vortex shedding frequency [Hz]
F_D	Mean drag force [N]
F_L	Mean lift force [N]
F_N	Mean wall-normal force [N]
H	Cylinder height [m]
M_P	Mean pitching moment [N·m]
M_R	Mean rolling moment [N·m]
M_Y	Mean yawing (bending) moment [N·m]
P	Centre-to-centre cylinder spacing or pitch [m]
P_0	Stagnation pressure [Pa]
P_∞	Freestream static pressure [Pa]
q_∞	Freestream dynamic pressure [Pa]
Re	Reynolds number based on cylinder diameter
S	Sutherland temperature [K]
St	Strouhal number
T_0	Reference temperature for Sutherland’s equation [K]
T_∞	Freestream temperature [K]
u	Local streamwise velocity [m/s]
U_∞	Freestream velocity [m/s]
$U(z)$	Boundary layer mean velocity profile [m/s]

x	Streamwise coordinate [m]
y	Transverse coordinate [m]
z	Wall-normal coordinate [m]

Greek Symbols

α	Incidence angle [°]
δ	Ground plane boundary layer thickness [m]
δ^*	Ground plane boundary layer displacement thickness [m]
θ	Ground plane boundary layer momentum thickness [m]
μ_0	Reference viscosity for Sutherland's equation [kg/m·s]
μ_∞	Freestream dynamic viscosity [kg/m·s]
ρ_∞	Freestream density [kg/m^3]

Chapter 1 Introduction

1.1 Background

The study of bluff bodies immersed in a cross-flow may be applied to a wide range of applications. Many wind and marine engineering projects can be modelled using simplified geometric shapes, such as cylinders. A cylinder that is sufficiently long and slender such that the end effects are negligible, and for which the flow and geometry can be considered two-dimensional (2D), is often referred to as an "infinite" cylinder. For a sufficiently high Reynolds number, a pair of separated shear layers forms from the sides of the cylinder and a low-pressure wake develops downstream of the cylinder. This low pressure region downstream, coupled with the high pressure exerted by the fluid impacting the upstream side of the cylinder, are largely responsible for the high drag forces (or wind loading) experienced by a cylinder. Like with many bluff bodies, the skin-friction exerts much smaller forces relative to the pressure acting on solid surfaces. The separated shear layers that produce the low pressure wake roll up on alternating sides of the cylinder before being shed, one at a time, into the wake as vortices; this is the familiar Kármán vortex shedding phenomenon. The frequency of vortex shedding is also a concern, as frequencies near a natural frequency of the structure may lead to vortex-induced vibration.

The flow around an infinite cylinder has been extensively studied, and there are several key review articles and references (Coutanceau and Defaye, 1991; Williamson, 1996; Zdravkovich, 1977) on the subject; however, an infinite or 2D cylinder is not often a close match to actual engineering applications. A truncated finite-height cylinder mounted in a cantilevered manner to a flat surface more closely resembles many engineering applications, and the effects of the free end and surface mounting can be profound on the resulting wind loads and vortex shedding frequency. The low pressure wake behind this three-dimensional (3D), surface-mounted, finite-height cylinder causes flow over and around the free end to be deflected towards the ground plane. The resulting "downwash" and streamwise counter-rotating tip vortices cause the entire flow and wake to become much more complex and strongly 3D. Additionally, the cylinder wall-junction and ground plane boundary layer lead to the formation of the horseshoe vortex upstream and surrounding the cylinder, and the flow varies significantly along the cylinder's height or span. The slenderness of the surface-mounted finite-height cylinder is found

to have strong effect on the resulting flow behaviour. Flow around surface-mounted finite-height cylinders has not been as extensively studied, however, compared to infinite cylinders.

Isolated cylinders of both infinite and finite-height configurations represent only a small portion of flows possible with cylindrical shapes. Two cylinders placed parallel to each in a staggered configuration (Figure 1.1) are subject to a large range of wind loads and vortex shedding frequencies based on their relative positions, due to wake and proximity interference and complex shear layer interactions. A cylinder placed within the wake of another can experience severely reduced wind loads as it is sheltered from the incoming flow, while cylinders placed side-by-side can experience a large repulsive side force as the flow is forced through the gap between the cylinders. The flow around two infinite cylinders has been extensively studied (Sumner, 2010; Zhou and Alam, 2016), whereas the flow around two surface-mounted finite-height cylinders has not received much attention, and this is the main focus of, and motivation for, the present research.

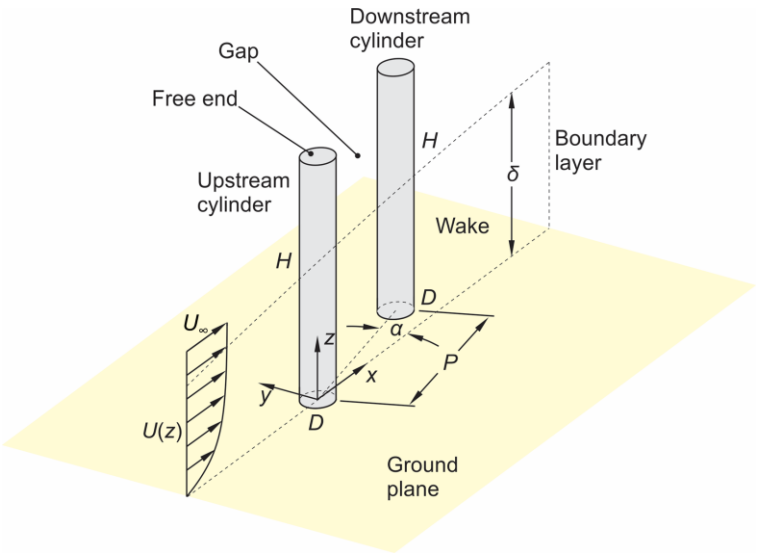

Figure 1.1: Schematic of geometric properties associated with the flow around two surface-mounted finite-height cylinders of diameter, D, and height, H, mounted in a general, staggered configuration. The centre-to-centre spacing, P, and incidence angle, α, define the staggered configuration. Note the coordinates: streamwise, x; transverse, y, and wall-normal, z. The flow itself is defined by the boundary layer mean velocity profile, $U(z)$, the freestream velocity, U_∞, and the boundary layer thickness, δ, on the ground plane. Key regions of the flow include the wake, gap, and free end.

A schematic of two surface-mounted finite-height cylinders (of diameter, D, and height, H) can be found in Figure 1.1. The cylinder slenderness or aspect ratio, AR = H/D, is the most important influencing parameter for the finite cylinders. The flow itself is characterized by the Reynolds number, Re (= $\rho_\infty U_\infty D/\mu_\infty$, where U_∞ is the freestream velocity, ρ_∞ is the fluid density, and μ_∞ is the fluid dynamic viscosity) and the boundary layer mean streamwise velocity profile, $U(z)$, which extends from zero at the ground plane to U_∞. The boundary layer thickness, δ, is defined as the wall normal position, z, at which $U(z) = 0.99U_\infty$ and the relative thickness of the boundary layer, δ/D, is a key influencing parameter for the finite cylinders. For the two staggered cylinders, the proximity and wake interference effects will be determined by the pitch ratio, P/D (where P is the centre-to-centre spacing of the cylinders), and the incidence angle, α. With different combinations of P/D and α, many flow patterns are possible that are sensitive to AR, Re, and δ/D across the entire range of possible cylinder configurations, from tandem ($\alpha = 0°$) to side-by-side ($\alpha = 90°$) and the staggered arrangements in between ($0° < \alpha < 90°$) as seen in Figure 1.2.

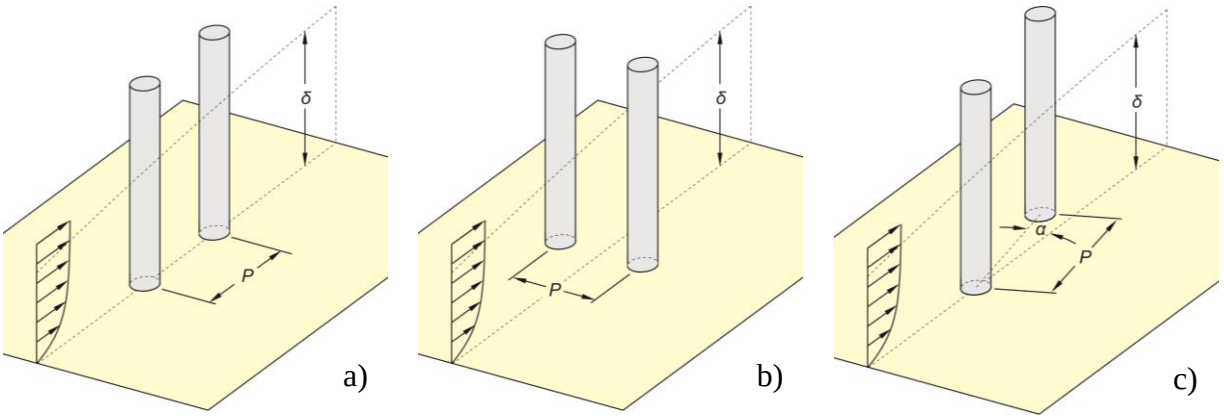

Figure 1.2: Configurations of two surface-mounted finite-height cylinders: a) tandem ($\alpha = 0°$); b) side-by-side ($\alpha = 90°$); and c) staggered ($0° < \alpha < 90°$).

The focus of the thesis research was on three main parameters that are functions of AR, P/D, α, Re, and δ/D. The mean coefficient of drag, C_D (= $2F_D/(\rho_\infty U_\infty^2 DH)$), is based on the time-averaged drag force, F_D, which is positive in the streamwise direction. The mean coefficient of lift, C_L (= $2F_L/(\rho_\infty U_\infty^2 DH)$), is based on the time-averaged lift (side) force, F_L, which is positive when there is a repulsive force between the cylinders; see ahead to Figure 1.3. Finally, the Strouhal number, St (= fD/U_∞, where f is the vortex shedding frequency), is the dimensionless

vortex shedding frequency, which, for the present thesis, was measured at the mid-height of the cylinders. The two aerodynamic force coefficients, C_D and C_L, represent the majority of the wind loading for each cylinder in the staggered configuration, while St represents the dominant vortex shedding frequency of each cylinder. Together these three parameters (C_D, C_L, and St) are of value to engineering applications involving the flow around surface-mounted finite-height cylinders in a staggered configuration.

1.2 Objectives

Three objectives were set for the research program detailed in this thesis:

1. Determine the influence of aspect ratio (AR) on the mean coefficient of drag (C_D), mean coefficient of lift (C_L), and Strouhal number (St) of both the upstream and downstream cylinders in staggered configurations between tandem and side-by-side inclusive, and compare the observed trends to the behaviour of two infinite cylinders in a staggered configuration in the literature.
2. Determine the effect of aspect ratio (AR) on the pitch ratio (P/D) and incidence angle (α) boundaries that produce the different flow patterns as described in the literature.
3. Examine the effect of aspect ratio (AR) and pitch ratio (P/D) on the hysteretic wind loading of the cylinders near the side-by-side configuration.

1.3 Scope and Methodology

Within the context of surface-mounted finite-height cylinders in a staggered configuration there are many aspects dependent on a variety of geometric and flow conditions. In the interest of completion time, the scope of this thesis was limited in both the number of measured quantities and the number of variables systematically changed. The main focus of this thesis is on the wind loading and the mid-height vortex shedding frequency. The wind load experienced by a finite cylinder can be divided into three orthogonal forces and moments (drag force, F_D, and rolling moment, M_R, along the streamwise direction, x; lift force, F_L, and yawing (bending) moment, M_Y, along the transverse direction, y; and normal force, F_N, and pitching moment, M_P, along the wall-normal direction, z) as shown in Figure 1.3. Time limitations limited the scope of wind loading to only the primary two forces found with staggered cylinders, namely the mean drag and lift forces (F_D and F_L) experienced by each of the two cylinders (non-dimensionalized as C_D and

C_L). The vortex shedding frequency, f, (non-dimensionalized as St) is also an important flow feature for bluff bodies. A finite cylinder of sufficiently high AR may exhibit a variation in St along its height, but to limit the testing time measurements of St were only taken at the mid-height ($z = H/2$) of both cylinders.

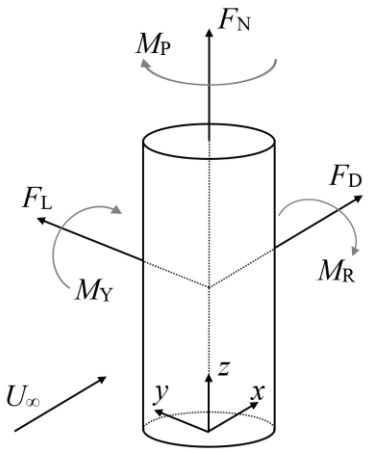

Figure 1.3: Aerodynamic forces and moments exerted on a surface-mounted finite-height cylinder: drag force, F_D; lift force, F_L; normal force, F_N; rolling moment, M_R; yawing (bending) moment, M_Y; and pitching moment, M_P. The coordinate system is centred at the cylinder-wall junction.

A summary of the independent variables and the ranges covered during the experiments can be found in Table 1.1. The effects of AR across the entire staggered range were the focus, and as such four aspect ratios (AR = 9, 7, 5, and 3) were chosen. These same aspect ratios have been tested previously under similar experimental conditions (Sumner et al., 2004; Adaramola et al., 2006; Igbalajobi et al., 2013; Rostamy et al., 2012; Sumner et al., 2015; Beitel and Sumner, 2017) and ensured that cylinders above the critical AR (AR = 9, 7, and 5) and below the critical AR (AR = 3) would be tested. The critical aspect ratio is found between AR = 3 and 5, though it is dependent on Re and δ/D, and cylinders below this point have a distinct wake structure (Sumner et al., 2004). The size of the cylinders were chosen to minimize blockage factor, maximize the measurable drag and lift forces, as well as maximize the range of P/D within the limited size of the existing turntable in the wind tunnel. Discrete pitch ratios (Table 1.1) were chosen similar to that of Sumner et al. (2005) to allow for direct comparison to infinite cylinder data, with additional P/D tested to help identify flow pattern boundaries that may change as a

function of AR. The highest pitch ratio of $P/D = 4.5$ was determined by the size of the turntable apparatus, as discussed later in Section 3.3. The adjustment of incidence angle, α, was incremented finer than AR and P/D, with increments of 1° across the entire staggered range between tandem ($\alpha = 0°$) and side-by-side ($\alpha = 90°$) used for C_D and C_L. In order to save experiment time, a coarser increment in α was used for measuring St for configurations where St was only slowly varying; a map of the α increment for each combination of AR and P/D can be found in Appendix A. For experiment-specific test trajectories, see ahead to Section 3.4 for C_D and C_L and Section 3.5 for St.

Table 1.1: List of independent parameters and their range covered within the scope of the research program.

Variable	Range
Aspect Ratio, AR	3, 5, 7, 9
Pitch Ratio, P/D	1.125, 1.25, 1.5, 1.75, 2.0, 2.25, 2.5, 2.75, 3.0, 3.5, 4.0, 4.5
Incidence Angle, α	0° to 90° (for exact increment see Appendix A)
Reynolds Number, Re	$6.5 \pm 0.1 \times 10^4$ (subcritical)
Boundary Layer Thickness, δ/D	1.4 ± 0.1

Though the Reynolds number, Re, and boundary layer thickness, δ/D, have a significant influence on the resultant flow field, wind loads, shear layer behaviour, and vortex shedding, they were kept constant to reduce experimental testing time. A subcritical Re (6.5×10^4) was chosen to remain consistent with previous work (Beitel, 2017), and to attain larger lift and drag forces so as to reduce the measurement uncertainty (discussed in Section 3.4). A subcritical Re is characterized by laminar boundary layers on the cylinder surface with early separation from the cylinder sides. The chosen δ resulted from the "untripped", natural development of the boundary layer from the rounded leading edge of the wind tunnel's ground plane, which ensured a fully developed turbulent flat-plate boundary layer at the location of the two cylinders. Discussion on Re and δ/D may be found in Section 3.2. Increased surface roughness of the cylinders can have a similar effect as increasing Re, however only smooth cylinders were tested.

1.4 Outline of Thesis

The thesis is divided into five main chapters and five Appendices. Chapter 2 is a review of present literature on the topics of infinite (2D) cylinders in a staggered configuration (Section 2.2), isolated surface-mounted finite-height cylinders (Section 2.3), and two surface-mounted finite-height cylinders in a staggered configuration (Section 2.4). Chapter 3 details the apparatus used to conduct the experiments, focusing on the wind tunnel (Section 3.2), cylinder models and positioning system (Section 3.3), and the instruments and methodology used to collect data for C_D, C_L, (Section 3.4) and St (Section 3.5). Chapter 4 contains an extensive discussion on the data gathered, separated into three main cylinder configurations. Section 4.2 encompasses the tandem configuration ($\alpha = 0°$) with Sections 4.2.1 and 4.2.2 covering C_D and St, respectively. Section 4.3 details the side-by-side configuration ($\alpha = 90°$) with discussion for C_D, C_L, St, and the hysteresis phenomenon found in Sections 4.3.1, 4.3.2, 4.3.3, and 4.3.4, respectively. Section 4.4 covers the remaining staggered configurations with Sections 4.4.1, 4.4.2, and 4.4.3 covering C_D, C_L, and St, respectively. Finally, Chapter 5 summarizes the conclusions of the thesis (Section 5.1), the contributions of this work (Section 5.2), and the recommendations for future work (Section 5.3).

Appendix A shows a visual representation of the AR, P/D, and α configurations used for the measurement of C_D, C_L, and St. Appendix B contains all of the measured data in plots for C_D, C_L, and St as a function of α, separated by P/D for the four aspect ratios. Appendix C details a method used to further capture the intermittent gap bias switching found for closely spaced cylinders in a side-by-side configuration. Appendix D is a detailed discussion on the C_L findings of Alam et al. (2003a) for infinite cylinders in a side-by-side configuration. Appendix E shows additional plots describing the hysteresis phenomenon for AR = 7 and AR = 5 that are relevant for Section 4.3.4. Appendix F contains the permissions from various publishers to reproduce figures from the literature.

Chapter 2 Literature Review

2.1 Introduction

Cylinders immersed in a cross-flow are common in present engineering applications, with a variety of flow characteristics carrying importance in the design. Their round cross-section and reduced stress concentrations contribute to strength when used in pressure vessels, storage tanks, and bins (ASME, 2012), making them commonplace in many industries. In many applications, these structures are exposed to potentially large wind loads, which can vary in strength and direction. Proximity and wake interference effects become an additional contribution to the wind loading experienced in storage tank farms or clusters of cylindrical bins (Portela and Godoy, 2005 and 2007). Exhaust stacks for factories, power generation facilities, and refineries are also commonly found in groups, with the local air flow around the cylindrical bodies of significance to ensure proper exhaust dispersion (Gerhardt and Kramer, 1981). The effectiveness of many cooling systems often relies on the flow of coolant or air around clusters of cylinders, whether they are in the form of cooling lines or pin fin arrays (Igarashi et al., 2004). Engineering applications involving cylinder groups are both varied and numerous (some examples are shown in Figure 2.1), with the flow characteristics being a key component.

The aerodynamic forces, vortex shedding, wake patterns, and flow-induced vibrations associated with two infinite cylinders in a staggered configuration (Figure 2.2) have been extensively studied and reviewed (Sumner, 2010; Zhou and Alam, 2016). The two-cylinder configuration is the simplest case of multiple cylinders, and has received the most attention in the literature. Section 2.2 contains a brief review of the literature pertaining to the flow around two infinite cylinders. Less well studied, however, is the flow around two surface-mounted finite-height cylinders in a staggered configuration. A literature review for the flow around an isolated finite cylinder, which better resembles the engineering applications described above (and illustrated in Figure 2.1), may be found in Section 2.3 that details the additional 3D effects caused by the fixed and free end. The research in this thesis is focused on the flow around two surface-mounted finite-height cylinders in a staggered configuration, and a literature review for this arrangement of cylinders is found in Section 2.4.

Figure 2.1: Common examples of cylinder groups in cross-flow: a) grain storage bins, b) electrical components, c) chemical storage tanks, and d) smoke stacks.

2.2 Flow around Two Infinite Cylinders in a Staggered Configuration

Two infinite cylinders of equal diameter D arranged in a staggered configuration (Figure 2.2), at arbitrary centre-to-centre spacing or pitch, P, and incidence angle, α, relative to the approach flow (with uniform freestream velocity U_∞), is the most general arrangement. This configuration is of value in describing the flow field and associated fluid-structure interactions for cylinders in a 2D plane. Comprehensive reviews on two infinite cylinders in a staggered configuration have been compiled recently by Sumner (2010) and Zhou and Alam (2016) and cover many of the key topics, such as wake and proximity interference, shear layer reattachment, vortex shedding behaviour, mean and fluctuating aerodynamic forces, pressure distributions on the cylinders, and the flow patterns.

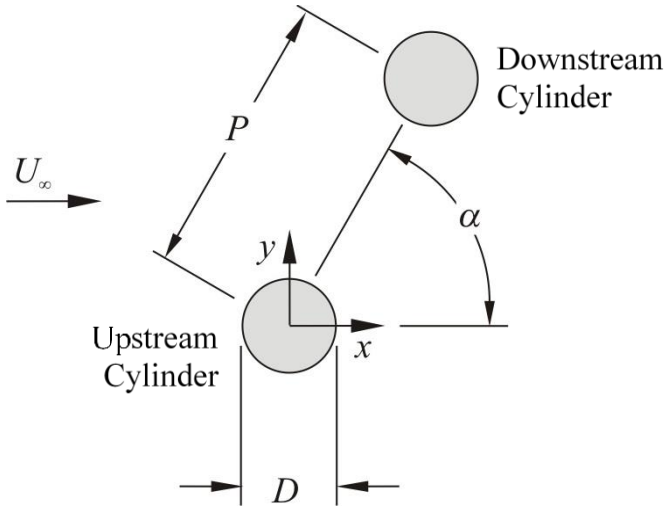

Figure 2.2: Schematic of two infinite cylinders in a staggered configuration.

There are many contributing geometric and flow parameters that influence the overall flow field. The pitch ratio, *P*/*D*, coupled with the incidence angle, α (Figure 2.2), allow for an infinite number of cylinder arrangements. Ranges of *P*/*D* and α fall into either wake and/or proximity interference regions, accounting for many of the flow regimes possible. The Reynolds number, Re, also has a strong influence on whether a given configuration of *P*/*D* and α will produce wake and/or proximity interference. For example, studies by Ljungkrona and Sundén (1993), Said et al. (2008), and Zhou et al. (2009) found the behaviour of shear layer separation, reattachment, and roll-up was found to be sensitive to Re. Consequently the flow structures, wake profile, wind loading, and vortex formations found at various *P*/*D* and α are all sensitive to Re as well.

Wake interference occurs when the downstream cylinder falls entirely or partially within the wake of the upstream cylinder as found in tandem configurations and staggered configurations at small α. The ultimate effect on the wake patterns becomes largely dependent on *P*/*D* as it dictates the ability of the upstream cylinder's shear layers to reattach onto the downstream cylinder, although Re has some influence. Flows in the near tandem configuration can be classified as extended body, reattachment, and co-shedding regimes contingent on how the shear layers shed from the upstream cylinder interact with the downstream cylinder (Zhou and Alam, 2016).

Proximity interference occurs when the wakes of both cylinders are influenced by the presence of the other cylinder, though neither body is immersed directly in a wake. This is found with side-by-side configurations and staggered configurations at large α. The strength of the interference is also largely dependent on P/D. When P/D is reduced the proximity effects become stronger as the fluid flowing through the gap between the cylinders is accelerated and may be deflected to one side. Flows experiencing proximity interference can be classified as base bleed, biased flow, and co-shedding regimes depending on the behaviour of the gap flow (Zhou and Alam, 2016).

2.2.1 Infinite Cylinders in a Tandem Configuration

Two cylinders arranged such that one is directly downstream from the other is a fundamental configuration. The wake interference resulting from tandem (or inline) cylinders can result in a significant reduction in drag (wind loading). Flow dynamics are dictated by the Reynolds number and P/D, with patterns classified into the extended body, reattachment, and co-shedding regimes (Figure 2.3).

The extended body flow regime (Figure 2.3a) is found at very small pitch ratios ($P/D \leq 1.125$), although it can persist to higher P/D at lower Reynolds numbers (Igarashi, 1981). This flow regime is characterized by the downstream cylinder residing entirely within the separated shear layers from the upstream cylinder without any reattachment. The two cylinders function as one body, with negligible flow between them and Kármán vortices rolling up on alternating sides behind the downstream cylinder at a Strouhal number, St, higher than that of an isolated cylinder (Sumner, 2010). The mean drag coefficient, C_D, for the upstream cylinder remains similar to that of an isolated cylinder (Sumner et al., 2005). The downstream cylinder, however, experiences significantly different mean wind loads, as the leading edge of the downstream cylinder experiences very low pressure stagnant gap fluid acting on it. Also, as it is enveloped in the separated shear layers from the upstream cylinder, the entire surface of the downstream cylinder is at a negative pressure coefficient (Alam et al., 2003b), resulting in an upstream-directed thrust force (or negative drag force). The magnitude of the thrust force is a strong function of P/D, with values able to reach $C_D = -0.50$ (Sumner et al., 2005). As the cylinders are arranged symmetrically with the flow and the vortices are produced in an alternating fashion, the time-averaged lift coefficient remains at zero (Sumner, 2010).

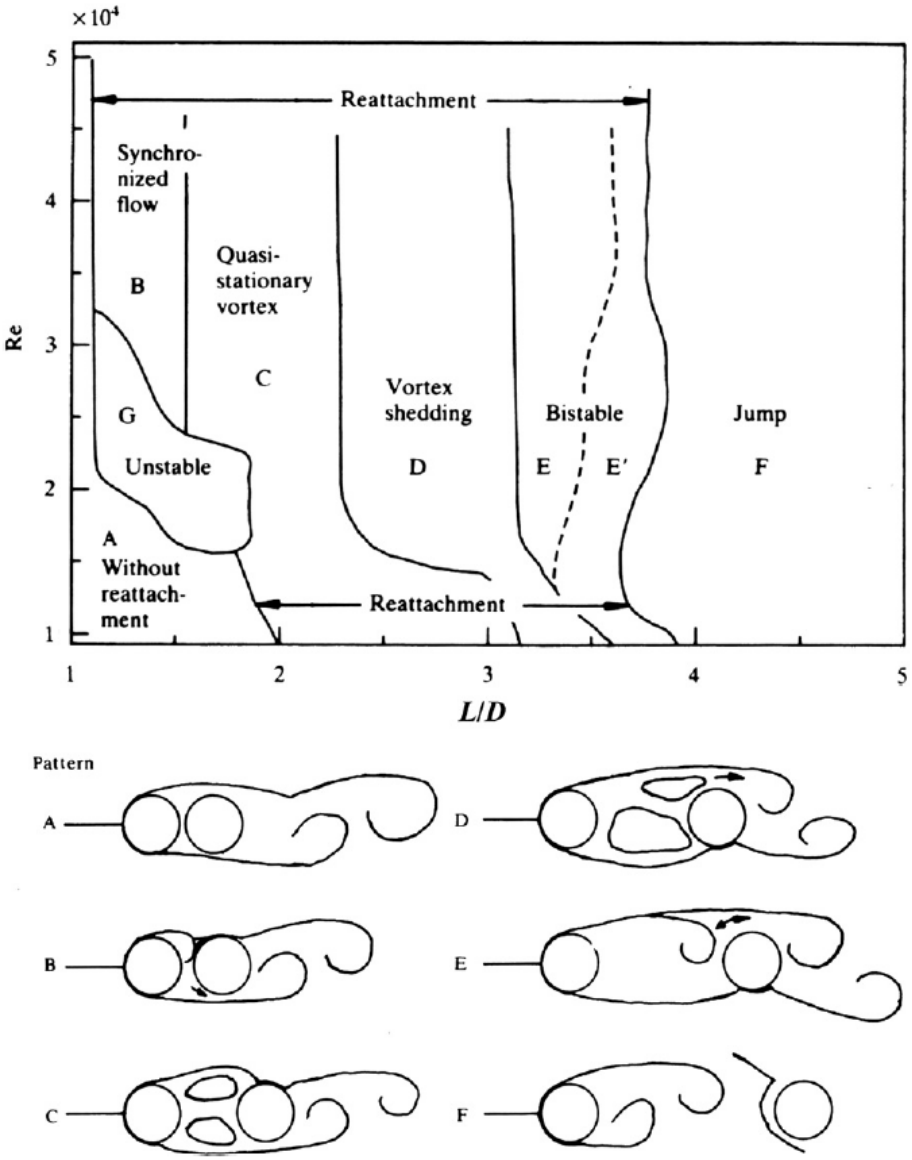

Figure 2.3: Tandem infinite cylinder flow regimes: a) extended-body, b-e) reattachment, and f) co-shedding. Figure taken from Sumner (2010); original source Igarashi (1981).

The reattachment regime (Figure 2.3b-e) is found at intermediate P/D (between values of 2.0 and 4.0), with higher Reynolds numbers allowing reattachment at P/D = 1.1 (Igarashi, 1981). This flow regime exhibits reattachment of the upstream cylinder's separated shear layers onto the surface of the downstream cylinder. As P/D increases, the reattachment behaviour can take different forms as illustrated in Figure 2.3b-e (Igarashi, 1981).

At P/D = 1.1 – 1.6 (Figure 2.3b) one shear layer will envelop and the other will reattach onto the downstream cylinder, which occurs in an alternating fashion. The reattaching shear layer splits into two, with the downstream portion separating further along producing a Kármán vortex and the upstream portion able to reattach to the base region of the upstream cylinder (Alam et al., 2003b). A strong thrust force is experienced by the downstream cylinder in this region (Sumner et al., 2005). At P/D = 1.6 – 2.5 (Figure 2.3c-d) both shear layers continuously reattach onto the downstream cylinder, with a similar upstream and downstream directed shear layer split upon reattachment. The symmetric shear layer behaviour produces a pair of counter-rotating gap vortices and a single Kármán vortex street (Alam et al., 2003b). The C_D (which is negative) of the downstream cylinder increases as P/D increases, peaking around a neutral drag force (Sumner et al., 2005). At P/D = 2.5 – 4.0 (Figure 2.3e) one shear layer will reattach to the downstream cylinder while the other rolls up into a vortex that impinges on the downstream cylinder, occurring intermittently. This produces asymmetric counter-rotating gap vortices while maintaining the single Kármán vortex street found with all reattachment flow regimes at a St number lower than an isolated cylinder (Sumner et al., 2005).

The co-shedding regime (Figure 2.3f) is found beyond a critical pitch ratio of P/D = 3.5 to 5.0 (dependent on Re), with the transition from the reattachment regime occurring abruptly (as a discontinuous change in C_D). The upstream cylinder sheds Kármán vortices which impinge on the leading face of the downstream cylinder triggering vortex shedding from the downstream cylinder. Both cylinders shed at the same frequency (St is similar to an isolated cylinder (Alam et al., 2003b)), only with a phase shift related to the distance between the cylinders (Sumner, 2010). During co-shedding, the downstream cylinder falls outside of the upstream cylinder's "vortex formation length". The vortex formation length is the streamwise distance downstream from the cylinder where the separated shear layers roll up and are shed into the wake as vortices, however the exact definition of this length has taken many forms from many authors (Noca et al., 1998). The vortex formation length has been defined as the point where the streamwise velocity fluctuations reach a peak, the point on the wake centreline where the streamwise Reynolds normal stress reaches a peak, the point along the wake centreline where the time-averaged streamwise velocity is zero (also known as the mean recirculation zone), and many others. Though the precise definitions vary, they all show similar trends, and as the vortex formation length of a cylinder depends strongly on Re (Noca et al., 1998), the P/D at which the upstream

cylinder can shed vortices becomes strongly dependent on Re as well (Sumner, 2010). A thorough study by Zhou et al. (2009) into the Re effects on the flow structures produced with staggered cylinders show that an increase in Re shortens the vortex formation length, causing the abrupt transition from the reattachment regime to the co-shedding regime to occur at lower P/D. Both upstream and downstream cylinders experience a sudden and large increase in C_D when transitioning into the co-shedding regime, with the downstream cylinder going from a mean thrust force to a mean drag force (Sumner, 2010).

Infinite cylinders in a tandem configuration generally have been well documented. Use of flow visualization techniques alongside both instantaneous and time-averaged measurements have given a fairly comprehensive view of how both P/D and Re affect the applied forces and shear layer behaviour. Identifying regions of strong vortex production and fluctuating lift forces are crucial for structural applications where strength can be compromised if vortex-induced vibration occurs near a resonant frequency. Abrupt changes in wake profiles like found at the onset of the co-shedding regime may also result in impulse-type (gust) loading, which is an important consideration in the design of structures.

2.2.2 Infinite Cylinders in a Side-by-Side Configuration

Two infinite cylinders arranged in a side-by-side configuration perpendicular to the incident freestream are another well-documented fundamental arrangement. Two side-by-side cylinders are a simplified version of a prevalent arrangement, with rows of adjacent cylinders often found as coolant lines in heat exchangers, as support cables in suspension bridges, or as a cluster of closely spaced high-rise buildings or smokestacks. Three predominant flow regimes (or flow patterns), namely the base bleed, biased flow, and co-shedding regimes (Figure 2.4), can be found in this configuration with the presence of each dependent on P/D and Re. Though the configuration is geometrically symmetric, strong proximity effects can cause close and moderate P/D to experience significant asymmetry in the wake profiles producing large mean lift coefficients and dissimilar vortex shedding frequencies and mean drag coefficients between the two cylinders.

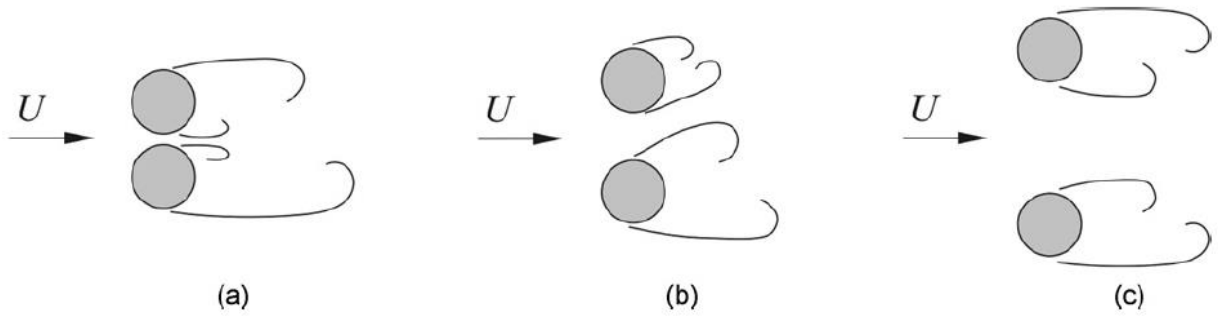

Figure 2.4: Side-by-side infinite cylinder flow regimes a) base bleed, b) biased flow, and c) co-shedding (where U is the freestream velocity). Figure taken from Sumner (2010).

The base bleed flow regime (Figure 2.4a) is found at $P/D \leq 1.2$, though the exact range is dependent on Re (Alam and Zhou, 2007). Alternating Kármán vortex shedding off the outer sides of the cylinders dominate the wake structure with both cylinders producing a single vortex street like a single wider bluff-body. Limited gap flow between the cylinders does not produce vortices, however it does bias strongly to one side. As the gap flow wraps behind one cylinder it ultimately joins the outer shear layer as it rolls into a vortex. Two modes of asymmetric gap flow may exist (Figure 2.5), with one prevalent at $P/D = 1.1$, the other at $P/D = 1.2$, and intermittent switching between both at P/D values between 1.1 – 1.2. With the gap bias direction also able to intermittently switch sides, a resulting "quadri-stable" flow regime is possible at $P/D = 1.13$ as found by Alam and Zhou (2007).

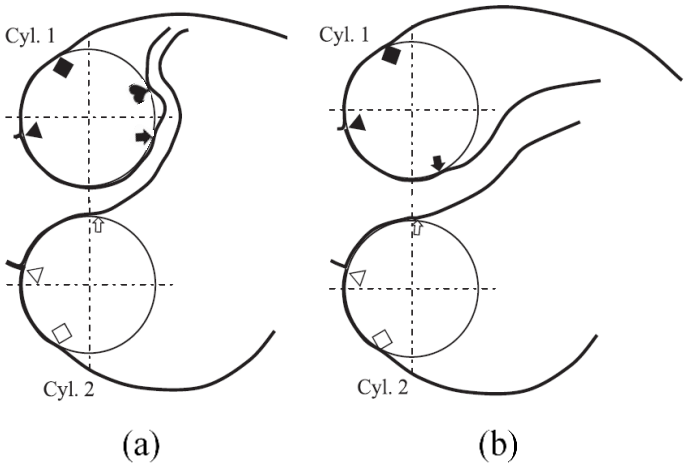

Figure 2.5: Side-by-side infinite cylinder base bleed flow patterns found at a) $P/D = 1.1$ and b) $P/D = 1.3$. ▼/▽, stagnation points; ■/□, outer separation points; ➡/⇨, inner seperation points; ♥, reattachment point. Figure adapted from Alam and Zhou (2007).

At P/D = 1.1 (Figure 2.5a) the gap flow remains attached to the inner face up to 175° from the leading edge of the "narrow wake" cylinder. A separation bubble occurs for approximately 40° along the base region of the cylinder, after which the flow reattaches and subsequently separates, joining the outer shear layer. The attached flow over the entire inner face and base region of the narrow wake cylinder produces a large area of low pressure, resulting in the mean lift force on the narrow cylinder being inward directed (toward the gap and the "wide wake" cylinder) (Alam and Zhou, 2007; Sumner, 2010) and the mean drag force to be significantly higher than the wide wake cylinder (Sumner, 2010). The strong proximity interference and significantly less negative base pressure causes the non-biased wide wake cylinder to experience a strong outward directed (away from the gap and the narrow wake cylinder) mean lift force coefficient, C_L, (Alam and Zhou, 2007) and a relatively low C_D (Sumner, 2010). Though the gap flow between the cylinders is highly asymmetric, the single bluff-body type vortex shedding occurs from only the outermost shear layers of the two cylinders at a single Strouhal number approximately half that of an isolated cylinder (Sumner, 2010).

A similar biased base bleed flow pattern may be found at P/D = 1.2 (Figure 2.5b) where the gap flow follows the inside face of one cylinder, though the deflection angle of the gap flow is much smaller. Separation from the inner face of the narrow wake cylinder is found at 112° from the leading edge, with the deflected gap flow joining the outer shear layer in a similar manner as P/D = 1.1. Though proximity effects are weaker and the gap flow does not remain attached for as long as at P/D = 1.1, the cylinders still have dissimilar wind loads. The narrow wake cylinder experiences a more repulsive C_L and a higher C_D whereas the wide wake cylinder is found to have a less repulsive C_L and a lower C_D (Sumner et al., 2005). In a similar fashion to P/D = 1.1, the weak base bleed gap flow does not contribute significantly to the outer shear layer "single bluff-body" behaviour resulting in a similar value of St (Sumner, 2010).

The biased flow regime (Figure 2.4b) may be found between P/D = 1.2 and 2.0, depending on Re. Both cylinders undergo vortex shedding despite the strong proximity interference and gap flow deflection. The deflection angle is proportional to the proximity effects, with smaller P/D values leading to higher deflection angles. Narrow and wide near wakes form behind the cylinders, with the narrow wake associated with a higher C_D, C_L, and St and the wide wake associated with a lower C_D, C_L, and St (Sumner et al., 2005).

The transition from the biased flow regime to the co-shedding flow regime (Figure 2.4c) occurs near $P/D \geq 2.0$, though the exact boundary is both Re dependent and a subtle, smooth transition. As P/D increases the proximity interference weakens, reducing the gap flow deflection until the overall flow field is symmetric and there are two parallel vortex streets in the wakes of the cylinders (Sumner, 2010). Though the wake patterns become more akin to those found behind an isolated cylinder, the mutual influence of the other cylinder results in vortex shedding synchronization. Anti-phase synchronization is most commonly found, with in-phase synchronization also possible though much less stable (Sumner, 2010). Both cylinders experience similar wind loads and vortex shedding frequency near the onset of the co-shedding regime (Sumner, 2010). Values of C_D, C_L, and St asymptotically approach that of an isolated infinite cylinder as P/D tends toward a value of 5.0 (Sumner, 2010).

In summary, side-by-side infinite cylinders may experience a wide range of wind loading and vortex shedding behaviour across the range of P/D. Closely spaced cylinders ($P/D \leq 1.2$) show very dissimilar values for C_D, C_L, and St as the limited gap flow wraps around to the base region of one of the cylinders. Abrupt changes in wind loading occur as the near wake profile changes mode and when the gap flow changes sides. The asymmetric flow field for moderately spaced cylinders ($1.2 < P/D \leq 2.0$) is characterized by a narrow wake and a wide wake, with the narrow wake cylinder experiencing relatively higher C_D, C_L, and St. Some studies report the asymmetric flow pattern to be bi-stable, in that the direction of the gap flow (and the narrow and wide wakes) can intermittently switch from one cylinder to another, or be stably biased to one of the cylinders for many vortex shedding periods (Sumner, 2010). Widely spaced side-by-side cylinders ($P/D \geq 2.0$) each shed vortices similar to isolated cylinders though the vortex formation is synchronized either anti-phase or in-phase.

2.2.3 Infinite Cylinders in a Staggered Configuration

A staggered configuration of two infinite cylinders represents any configuration whose angle of incidence lies between tandem ($\alpha = 0°$) and side-by-side ($\alpha = 90°$). The oblique angles found in staggered configurations lead to complex shear layer interactions that can produce new flow patterns in addition to variants of the flow regimes previously discussed. As with tandem and side-by-side configurations, the exact boundaries between flow regimes are functions of P/D and Re, with the addition of α as a third influencing parameter. Studying the flow around staggered cylinders is a more practical approach to understanding wake and proximity interference effects as a very limited number of real engineering applications will be exposed to exclusively parallel or perpendicular freestream conditions, notably so in outdoor conditions where the freestream is comprised of wind that may come from any direction or change direction over a time period.

Many varying flow regimes are possible within the scope of P/D, α, and Re. Classification of these modes may differ with the flow characteristic of focus. Sumner et al. (2000) found nine different flow patterns at Re = 850 – 1900, which were grouped into single bluff-body, small incidence angle, and large incidence angle flow patterns (Figure 2.6). The defining feature of each flow pattern was the shear layer behaviour in the near wakes of the two cylinders. Hu and Zhou (2008) characterized the observable flow patterns at Re = 7000 by the number of vortex streets found in the wake, with further classification based on the vortex behaviour in the far wake. Zhou et al. (2009) studied the effect of Re on pre-existing vortex formation patterns in the near wake, with many individual modes described. Many of the flow pattern classifications overlap, though due to varying Re used for each classification system the boundaries in P/D and α vary.

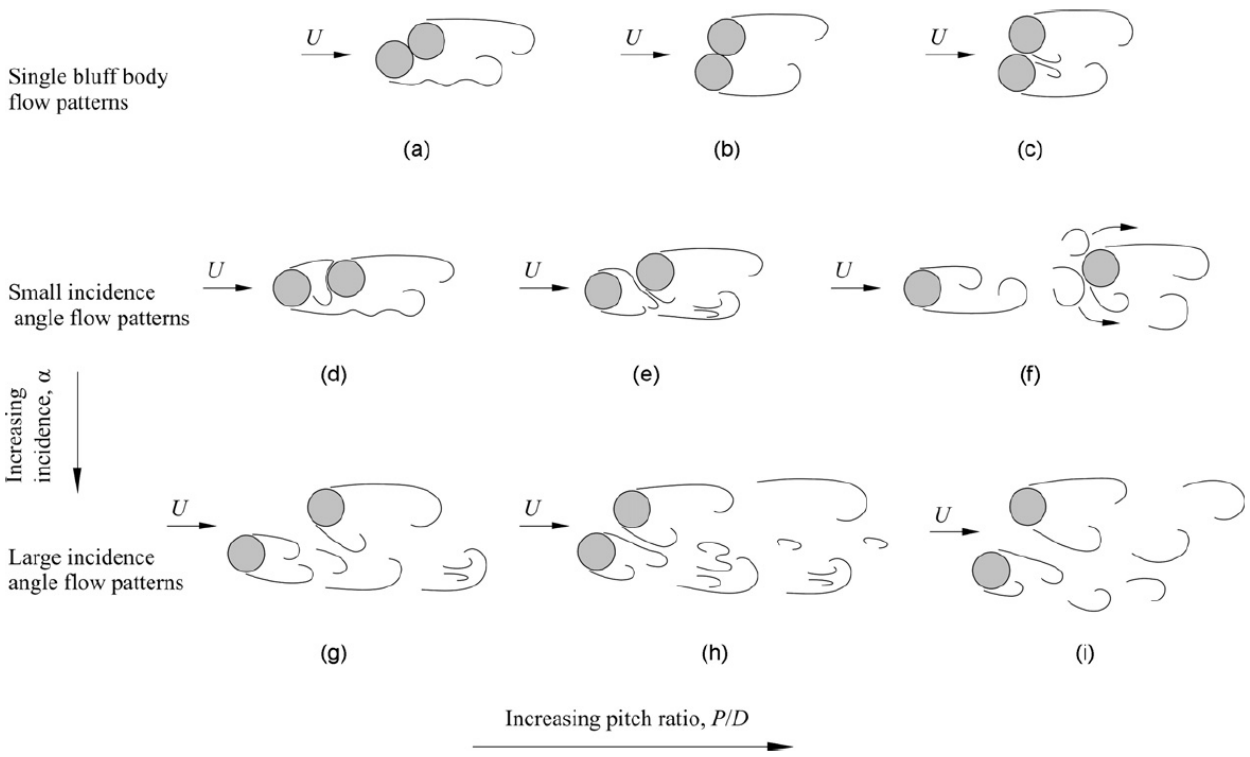

Figure 2.6: Staggered infinite cylinder flow regimes as classified by Sumner et al. (2000). Figure taken from Sumner (2010); original source Sumner et al. (2000).

Single bluff-body (Figure 2.6a-c) flow patterns are found at all α when $P/D \leq 1.25$ and are characterized by negligible gap flow between the cylinders and a single vortex street formed by the outer shear layers. Single bluff-body type 1 (SBB1 found in Figure 2.6a) is found near tandem (α = 0° - 45°) at very close spacing ($P/D < 1.125$) and is marked by uneven length shear layers between the upstream and downstream cylinders. At angles very near tandem ($\alpha < 15°$) the downstream cylinder is shielded by the upstream cylinder and resides within its low pressure base region, resulting in a thrust force (up to $C_D = -0.53$). Around $\alpha = 9°$ the "inner lift peak" is found, which corresponds to the rapid development of an inward-directed lift force experienced by the downstream cylinder (up to $C_L = -0.67$). At the inner lift peak the mean drag coefficient for the downstream cylinder attains a local minimum value (Sumner et al., 2005). Both cylinders shed vortices off their outer sides at the same frequency throughout this regime, with a maximum value at the inner lift peak of St = 0.25 (Sumner et al., 2005). Single bluff-body type 2 (SBB2 found in Figure 2.6b) is found near side-by-side (α = 45° - 90°) and very small pitch ratios (P/D

< 1.125) though unlike SBB1 the outer shear layers are of equal length and shed at the same frequency like a single body at St = 0.12 (Sumner et al., 2005).

The base bleed flow pattern (BB found in Figure 2.6c) is the third single bluff-body flow pattern and is observed near side-by-side (α = 45° - 90°) with closely spaced cylinders (P/D = 1.125 – 1.25) (the BB flow pattern closely resembles the base bleed flow regime for two side-by-side cylinders discussed previously). The data presented by Sumner et al. (2005) show dissimilar wind loading on the cylinders near α = 90° with one cylinder experiencing a significantly higher C_D and lower C_L (analogous to the findings of Alam and Zhou (2007) for closely spaced side-by-side cylinders). The three single bluff-body flow patterns described by Sumner et al. (2000) (SBB1, SBB2, and BB) broadly coincide with the S-Ia mode identified by Hu and Zhu (2008).

Small incidence angle flow patterns (Figure 2.6d-f) are found at all but the smallest P/D where the cylinders are near tandem (α < 20° - 30° depending on P/D). These flow patterns have a single vortex street and strong wake interference as the upstream shear layers interact directly with the downstream cylinder. The shear layer reattachment flow pattern (SLR in Figure 2.6d) is found very near tandem (α < 15°) and with moderately to closely spaced cylinders (1.125 < P/D < 3.0). The SLR flow pattern is characterized by the inner shear layer from the upstream cylinder reattaching onto the outer surface of the downstream cylinder. As the shear layer envelops the downstream cylinder there is no appreciable gap flow. The SLR flow pattern overlaps with the S-Ib mode found by Hu and Zhou (2008). Similar to SBB1, the shielding from the upstream cylinder allows the downstream cylinder to experience a thrust force proportional to the closeness of the cylinders (Sumner et al., 2005). The inner lift peak described earlier persists in the SLR regime as well, for example Sumner et al. (2005) found the downstream cylinder at P/D = 1.5 would experience the local peak value of lift at α = 9°.

The induced separation flow pattern (IS in Figure 2.6e) is found at the same pitch ratios as SLR (1.125 < P/D < 3.0) but at slightly higher incidence angles (α = 15° - 25°). The upstream cylinder's inner shear layer now moves next to the inner surface of the downstream cylinder, with the deflected gap flow between the cylinders triggering early separation off the inner face of the downstream cylinder. With the downstream cylinder outside of the upstream cylinder's shear layer and able to produce vortices off both inner and outer faces, there is a rapid reduction in the magnitude of attractive C_L and increase in C_D. As found by Sumner et al. (2005) at P/D = 2.0,

moving away from the inner lift peak by just 7° the value of C_L for the downstream cylinder increases from −1.16 to −0.43 with C_D also increasing from −0.28 to +0.48. This sudden change in wind loading (and in the vortex shedding frequency) with a small change in wind direction may be problematic for structural engineers.

The vortex impingement flow pattern (VI found in Figure 2.6f) is found at similar incidence angles as SLR and IS ($\alpha < 20° - 30°$) but at higher pitch ratios ($P/D > 3.0$). Here the cylinders are far enough apart that the upstream cylinder's shear layers can roll up into vortices, which once shed then impact the leading face of the downstream cylinder. A less prominent "outer lift peak" is found where the downstream cylinder aligns with the outer edge of the wake of the upstream cylinder; the outer lift peak is found at a higher α than the inner lift peak. The outer lift peak is far less sensitive to α, and at $P/D = 4.0$ it occurs at $\alpha = 18°$ with no corresponding local minimum in C_D. Since the upstream cylinder is far upstream and the wake interference effects are relatively small, it acts similar to an isolated cylinder throughout this flow pattern (Sumner et al., 2005). Both the IS and VI flow patterns reside within the P/D and α range described as S-II by Hu and Zhou (2008).

Large incidence angle flow patterns (Figure 2.6g-i) occur at between $P/D = 1.5 – 5.0$ and over the majority of the staggered range away from tandem ($20° - 30° < \alpha < 90°$ depending on P/D). Proximity interference influences the vortex shedding that occurs behind both cylinders, with the far-wake interactions dictating whether two vortex streets persist or if one envelops the other (Hu and Zhou, 2008). The vortex pairing and enveloping flow pattern (VPE in Figure 2.6g) occurs between $P/D = 1.25 – 3.5$ at $\alpha = 20° - 45°$. This region is a narrow band adjacent to the induced separation flow pattern, though instead of the upstream cylinder's inner shear layer reattaching onto the inner face of the downstream cylinder, it rolls up into a vortex and is forced into a narrow wake behind the upstream cylinder. The inner face of the downstream cylinder also forms a vortex that is drawn in behind the upstream cylinder. As both of the paired weaker gap vortices progress downstream they are enveloped by the stronger outer shear layer from the upstream cylinder, resulting in a single vortex street.

A variant of the VPE flow pattern is the vortex pairing, splitting, and enveloping flow pattern (VPSE in Figure 2.6h). Both gap vortices still pair up, though the outer shear layer splits the downstream cylinder's gap vortex in two as it envelops the pair. What is left of the split

vortex remains between the two larger vortices formed from the outer shear layers as the wake proceeds downstream. As the only difference between the VPE and VPSE regime is a subtle change in the far wake, the wind loading characteristics are fairly similar. Also, as both VPE and VPSE ultimately revert back to a single vortex street in the far wake, they both fall under the S-II mode defined by Hu and Zhou (2008).

The synchronized vortex shedding flow pattern (SVS found in Figure 2.6i) is found over a large range of moderately to widely spaced staggered configurations, essentially as long as the downstream cylinder is situated more than 1.5D away from the upstream cylinder in the transverse direction. No vortex enveloping occurs, but the twin vortex streets formed behind the cylinders synchronize as either in-phase or more commonly anti-phase. Proximity effects still influence the wakes, and in a similar manner to the biased flow pattern for side-by-side cylinders, the staggered cylinders in the SVS regime experience a larger disparity in their wake widths the closer they are spaced. As the SVS flow pattern produces twin vortex streets it falls into the T-I and T-II modes identified by Hu and Zhou (2008), with the T-I mode covering the vast expanse of the SVS region, and the T-II mode only applying in the very near side-by-side region (within an α of 2°). Data from Sumner et al. (2005) show trends for either end of the SVS spectrum at P/D = 1.5 and 4.0. At P/D = 1.5 the downstream cylinder has the wide wake with a lower C_D, C_L and St. The upstream cylinder maintains a narrow wake with a higher C_D, C_L and St. As P/D increases the proximity effects weaken, causing the cylinders to behave more independent of each other, like isolated cylinders, at P/D = 4.0.

With the large number of cylinder arrangements within the range of P/D = 1.0 – 5.0 and α = 0° - 90° summarized in Figure 2.6 there follows that a vast amount of data can be produced to capture the flow's behaviour. Complex shear layer interactions in the near wake found at very low P/D can produce abrupt changes in surface pressure and mean wind load. Equally complex vortex interactions in the far wake found at intermediate to large P/D can produces vastly different vortex shedding frequencies between the cylinders. Research into the numerous possible modes of flow for two infinite cylinders in a staggered configuration helps to provide a comprehensive view for use in engineering applications.

2.3 Flow around an Isolated Surface-Mounted Finite-Height Cylinder

A cylinder of diameter *D* and height *H* affixed to a ground plane on one end and immersed freely in the flow on the other end, as seen in Figure 2.7, is a common geometry that covers a wide range of scales and applications. Details on the wind loading and vortex shedding frequency for these surface-mounted, finite-height cylinders are of value as many structures such as cooling towers, grain bins, and fuel storage tanks (Figure 2.1) can be approximated as cantilevered cylinders. Vortex induced vibration of large structures can have devastating effects, and research in this field has benefited the safe design of many engineering structures (Wu et al., 2012). The vortex dynamics around surface-mounted finite-height cylinders plays a significant role in air quality studies as well with exhaust gas entrainment behind smokestacks and pollution dispersion around buildings in cities (Petersen et al., 2002).

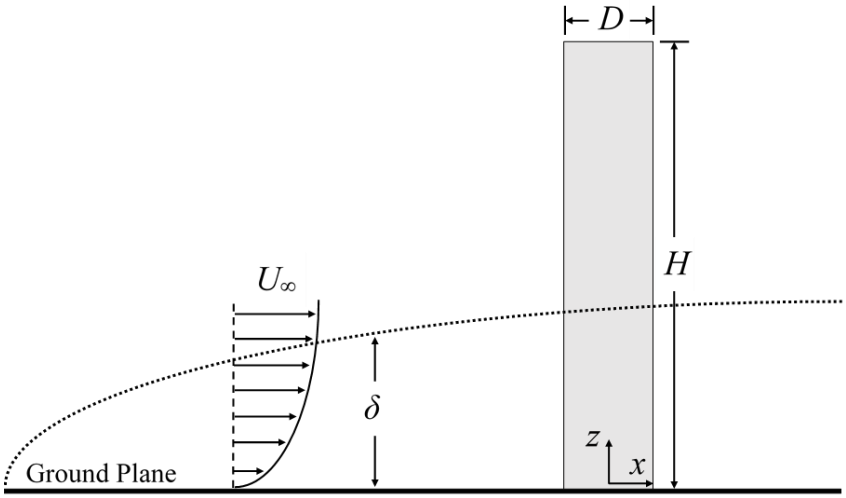

Figure 2.7: Schematic of the flow around a surface-mounted finite-height cylinder (of diameter *D* and height *H*) partially immersed in a flat-plate boundary layer (of thickness δ). The origin of the co-ordinate system (*z* being wall-normal (vertical) and *x* being streamwise) is at the centre of the cylinder at the junction with the ground plane.

There are several parameters that influence the flow patterns produced by finite cylinders. The aspect ratio, AR, of the cylinder is a measure of its slenderness and is the most important of these parameters. Additionally, the relative thickness of the ground plane boundary layer, δ/D, and the Reynolds number, Re, can influence how different flow patterns develop.

The Kármán vortex shedding found with infinite (2D) cylinders represents one of the four main vortex structures found once 3D effects are introduced via the free end (or tip) and the fixed end (cylinder-wall junction) flow conditions (Wang et al., 2006). Complex vortex systems and structures occur above the free end (Sumner, 2013), in the wake of the cylinder (Sumner et al., 2004), and near the ground plane (Sumner et al., 2017). For cylinders above a critical AR, streamwise tip vortex structures, Kármán vortices shed from the sides of the cylinder, streamwise base vortex structures, and a horseshoe vortex at the cylinder-wall junction, are present (Figure 2.8b and Figure 2.9). Below the critical AR, the base vortices are absent and the Kármán vortices connect near the free end to form an arch (Figure 2.8a) (Porteous et al., 2014). The additional vortex systems have an effect on the mean drag coefficient, C_D, and the Strouhal number, St, for the cylinder as well as the overall wake structure.

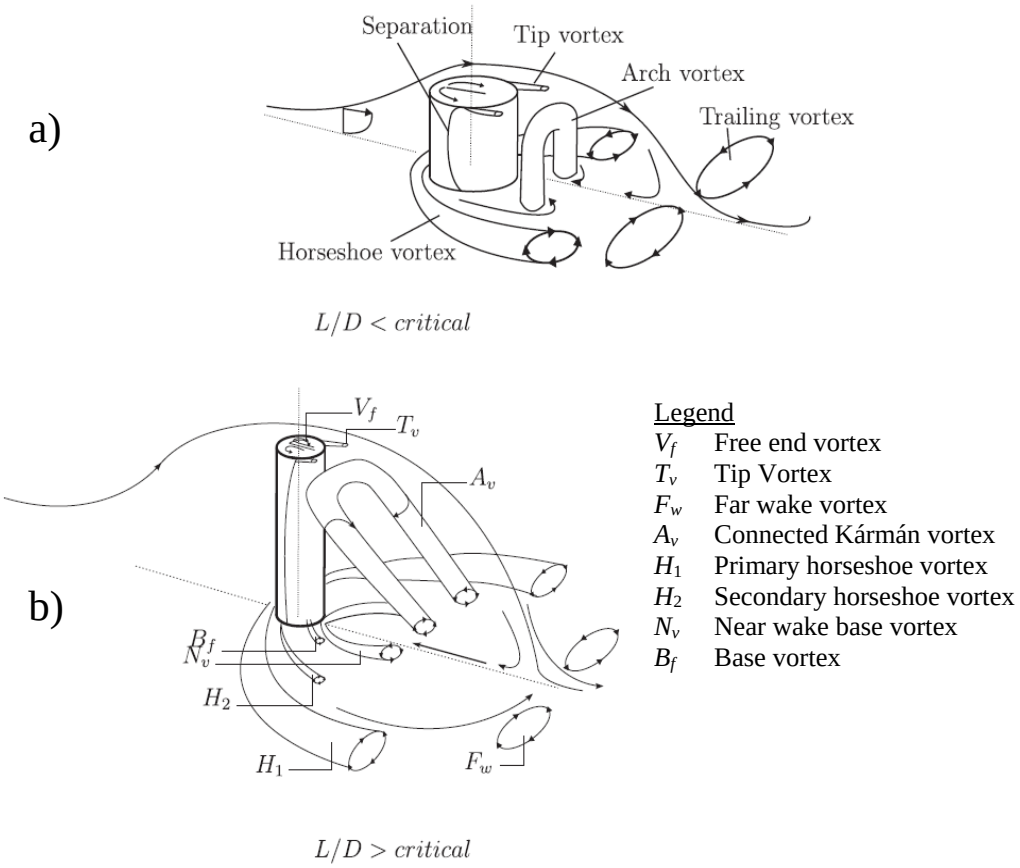

Figure 2.8: Surface-mounted finite-height cylinder (for cylinder height or length, L) vortex dynamics (a) below the critical aspect ratio and (b) above the critical aspect ratio (Porteous et al. 2014).

2.3.1 Free and Fixed End Effects for a Surface-Mounted Finite-Height Cylinder

Complex three-dimensional vorticity enters the fluid as it is allowed to flow over the free end of the finite cylinder and is obstructed by the ground plane at the fixed end. Additional vortex structures that strongly affect the near wake of a surface-mounted finite-height cylinder are the streamwise tip vortices, streamwise base vortices, and the horseshoe vortex. The tip vortices are a symmetric pair of counter-rotating vortices anchored at the tip of the cylinder that extend primarily in the streamwise direction but are angled slightly toward the ground plane. They rotate such that downwash is created along the wake centreline downstream of the free end in the upper part of the wake, deflecting the freestream fluid that passes over the free end of the cylinder towards the ground plane. The freestream entrainment adds momentum to the near wake, increases the base pressure, and reduces C_D (compared to an infinite cylinder). Tip vortices are stronger than base vortices (Sumner et al., 2004), and their effects contribute more to the overall wake profile. Though the reduced wind load on the cylinder is favourable for most structures, the entrainment of fluid from above the cylinder can bring exhaust fumes from smoke stacks back to the ground, causing air quality problems directly downstream of a stack if the stack exit momentum is too low (Adaramola et al., 2010). In a similar manner to the tip vortices, base vortices form as a symmetric pair anchored to the cylinder-wall junction region of the cylinder that rise away from the ground plane as they move downstream. The orientation of the base vortices produces “upwash” along the centreline of the cylinder wake near the ground plane, suppressing Kármán vortex shedding near the ground plane (Sumner et al., 2004). Effects from the base vortices are not as strong as the tip vortices. The horseshoe vortex is formed from the presence of the cylinder-ground plane junction. The boundary layer rolls up in front of the cylinder and the resultant vortex is diverted around either side of the cylinder base with the strength of the vortex proportional to δ/D (Sumner, 2013).

A surface-mounted finite-height cylinder’s wake vortex structure is highly dependent on AR, with a critical aspect ratio identified between AR = 3 – 5 by Heseltine (2003) and AR = 3 by Lee (1997). Far above the critical aspect ratio the vortex structures near the ends of the cylinder are weaker relative to the Kármán vortices formed at the mid-height, allowing the Kármán vortices to form uninterrupted at all but either end of the cylinder as seen in Figure 2.9. Near the critical AR the Kármán vortex shedding that normally occurs is more strongly influenced by the

tip and base vortices as they pinch off the mid-height region, inclining or bending the axes of the Kármán vortices (Figure 2.8b). Below the critical AR the base vortices no longer appear, and Kármán vortices that are usually shed from alternating sides connect at the free end forming an arch that is shed as one vortex (Figure 2.8a). Under the critical aspect ratio the tip vortices remain and become a large contributor to the wake profile. In this configuration the downwash is often strong enough to cause the freestream passing over the free end to reattach to the ground plane (Porteous et al., 2014).

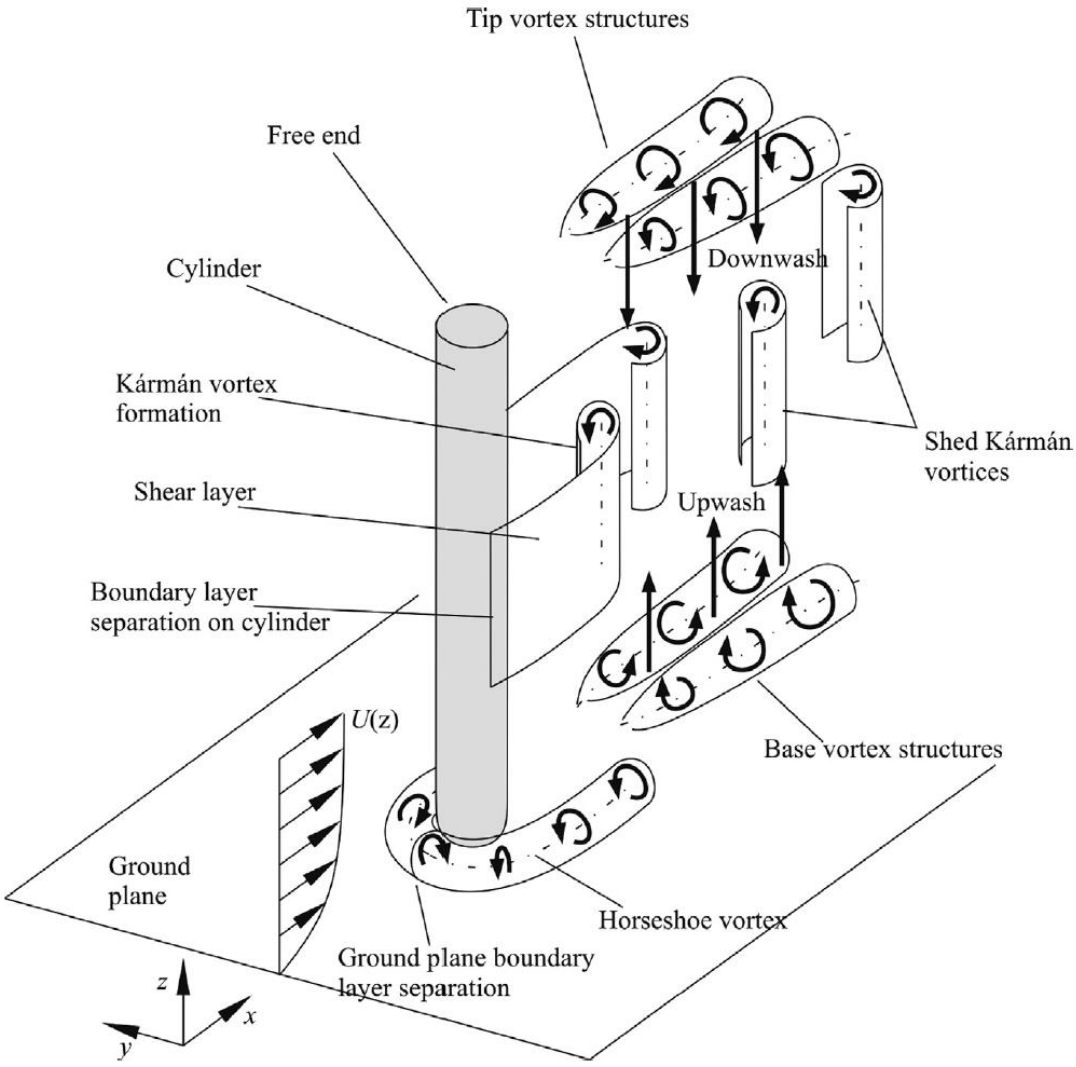

Figure 2.9: Surface-mounted finite-height cylinder vortex dynamics for significantly above the critical aspect ratio (taken from Sumner (2013); original source Sumner et al. (2004)). Here, $U(z)$ is the mean streamwise velocity profile of the boundary layer on the ground plane.

2.3.2 Near Wake of a Surface-Mounted Finite-Height Cylinder

It has been shown that the downwash induced from the tip vortices and the upwash induced by the base vortices can suppress the strength and the formation length of the Kármán vortices. Sumner et al. (2004) showed that lowering the cylinder aspect ratio from AR = 9 to AR = 3 results in weaker vortex shedding peaks near the mid-height position as the relative strength of the end effects grows. One of the definitions for vortex formation length offered by Noca et al. (1998) is the peak in velocity fluctuations measured by a hot-wire probe on the centreline of the wake. At AR = 9, the vortex formation length is longest just below the mid-height of the cylinder. The vortex formation lengths are shorter near the ends of the cylinder, with no discernable peak velocity fluctuation near the free end. This follows as the tip vortices are stronger than the base vortices, causing the pinching of the wake to be more severe from the top. A similarly shaped mean recirculation region (defined by the point of zero streamwise velocity) was found by Rostamy (2012) for AR = 7 and 5 likely due to the inclined Kármán vortices induced by the tip and base vortices requiring a longer formation length closer to the ground plane. Rostamy (2012) found that the vortex formation length increased with AR (from AR = 3 to AR = 7), where AR = 9 had a shorter and more constant vortex formation length (see Figure 2.10) along its mid-height. This is likely due to the diminished end effects allowing Kármán vortices to being produced uninterrupted along the majority of the cylinder height at a formation length similar to an infinite cylinder.

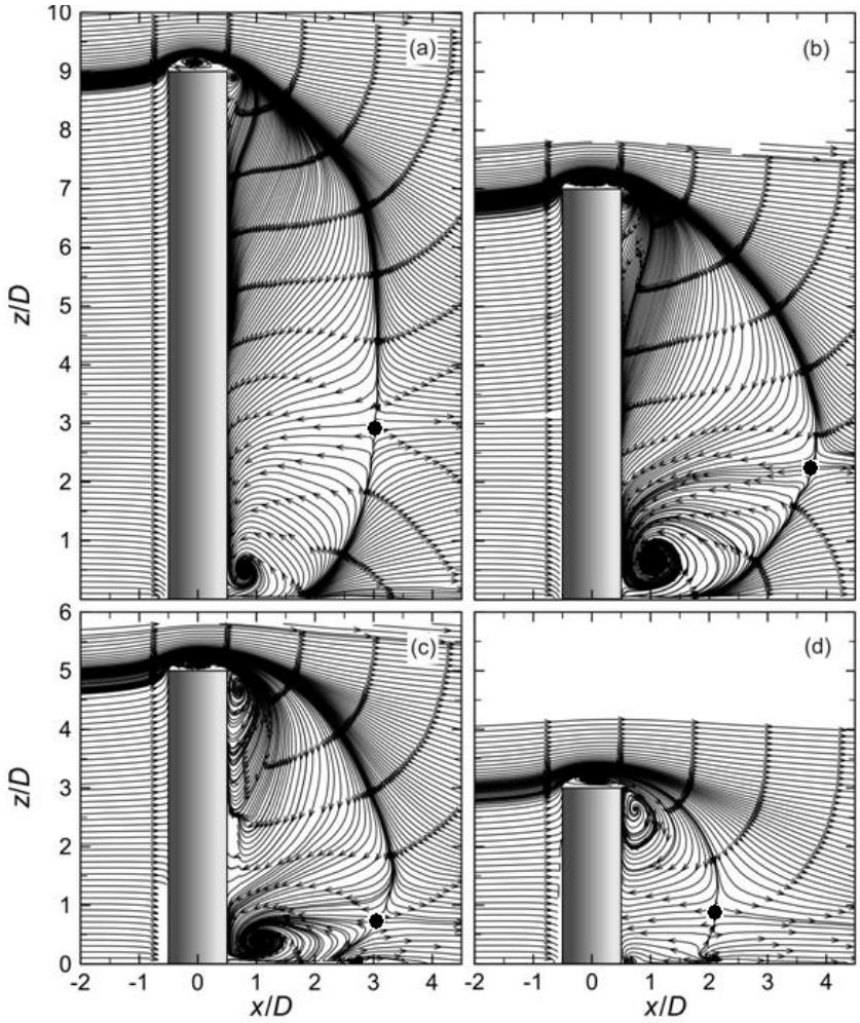

Figure 2.10: Mean streamlines in a vertical plane on the wake centreline for a) AR = 9, b) AR = 7, c) AR = 5, and d) AR = 3. Figure taken from Rostamy (2012) and reproduced with the permission of the student's supervisor, D. Sumner.

2.4 Flow around Two Surface-Mounted Finite-Height Cylinders in a Staggered Configuration

Groups of surface-mounted finite-height cylinders represent a large portion of structures and components in engineering applications today. Cooling towers, power transmission poles, storage tanks, high-rise buildings and many more large scale structures can be approximated as groups of cantilevered cylinders of various aspect ratios. The wake and proximity interference effects of two staggered cylinders, combined with the additional vortex structures produced by

finite-height cylinders, result in a highly complex flow field that is sensitive to P/D, α, AR, δ/D, and Re (Figure 2.11). Though this configuration (Figure 2.11) is the most applicable to design problems, the literature is far more limited than for infinite staggered cylinders or isolated finite-height cylinders. Contributions can be made regarding the effects of AR specifically on when different flow regimes develop, as well as the behaviour of C_D, C_L, and St across the entire staggered range (P/D = 1.0 – 5.0 and α = 0° – 90°).

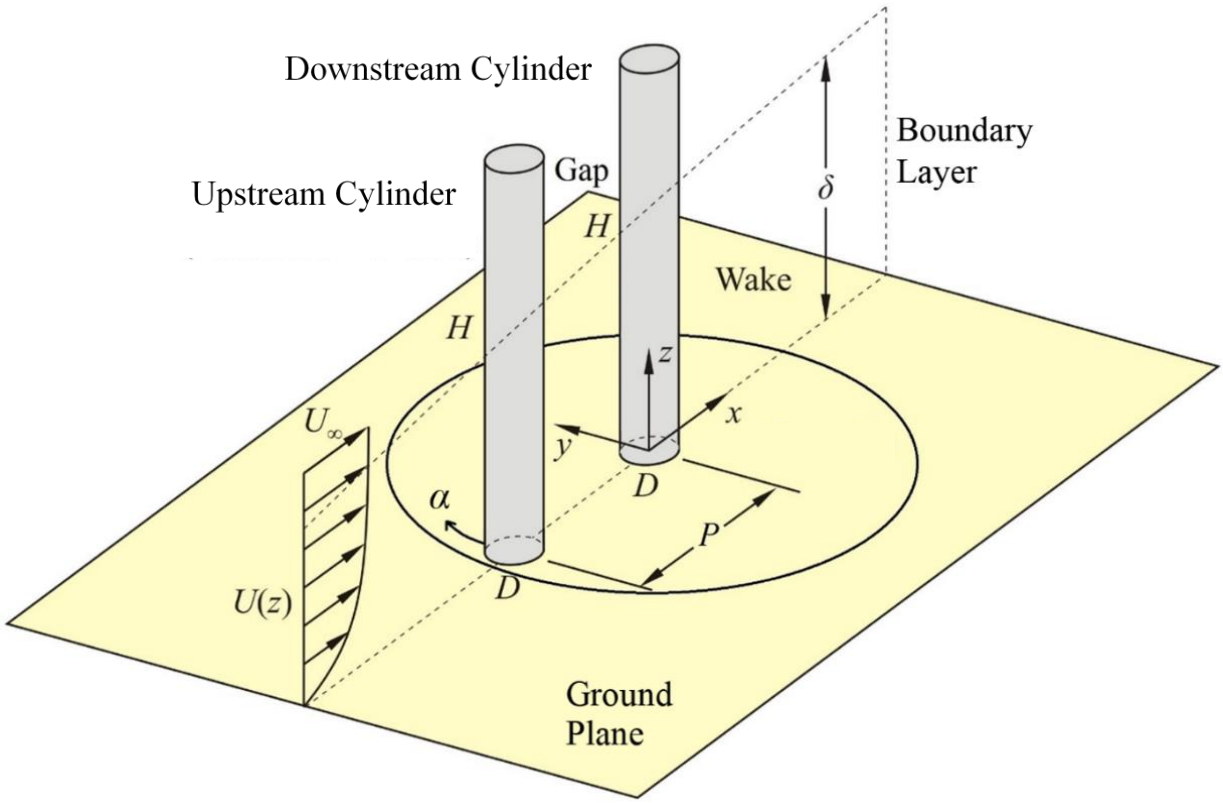

Figure 2.11: Schematic of two surface-mounted finite-height cylinders (each of the same diameter, height, and aspect ratio) in a staggered configuration.

A key feature of the finite-height cylinders is the modification to Kármán vortex shedding due to the finite height and end conditions. For finite cylinders, Kármán vortex shedding is only found at the mid-height well above the critical aspect ratio. As tip and base vortices pinch the wake, the mid-height vortex formation length of a finite-height cylinder is longer and the near-wake region becomes wider (outwards from the centre line) than those of an infinite cylinder (Rostamy, 2012). These differences potentially allow the closely spaced flow

patterns to be maintained at higher P/D; for example, Li and Sumner (2009) reported two finite cylinders of AR = 9 experiencing reattachment behaviour at P/D = 3.0, a point at which infinite cylinders would typically exhibit co-shedding. The shear layers of finite-height cylinders also roll up into vortices farther away from the wake centreline in the transverse direction, potentially allowing shear layer reattachment at higher α away from tandem; for example, Taniguchi et al. (1982) found that inner lift peak for two staggered finite cylinders of AR = 3 was at α = 15° for P/D < 3.0, compared to α = 8° for infinite cylinders in this P/D range (Sumner et al., 2000). Variation of the vortex formation length along the heights of the finite-height cylinders could potentially even allow multiple flow patterns to co-exist at different locations along the heights of the cylinders, provided the aspect ratio is sufficiently high (Sumner and Li, 2014). For example, at moderate P/D the upstream cylinder's shortened vortex formation length near the free end may result in a co-shedding regime over the upper portion while the mid-span shear layers remain reattached to the downstream cylinder.

Isolated surface-mounted finite-height cylinders experience a lower C_D and St than infinite cylinders due to the downwash and upwash entraining high momentum freestream into the wake fluid and weakening the Kármán vortex shedding. This reduction in drag when compared to infinite cylinders is reported for most staggered configurations, with a notable exception within the extended body regime for tandem cylinders. In this configuration infinite cylinders experience a strong thrust force as the entire downstream cylinder resides within the separated shear layers. The extended vortex formation length allows the downstream cylinder to maintain shear layer reattachment at wider P/D, up to P/D = 5.0 as found by Luo et al. (1996). Additionally, the freestream impingement on the upper portion at smaller P/D results in a weaker overall thrust force (Taniguchi et al., 1982; Luo et al., 1996). Said et al. (2008) found with AR = 2.67 cylinders at P/D = 5.33 that the lower portion of the cylinders would experience co-shedding, where a large portion of the downstream cylinder would be exposed to the entrained freestream. Local minima and maxima in the C_D and C_L curves (with α) are lower in magnitude and less sensitive to changes in P/D when compared to infinite staggered cylinders. Spanwise (along the height) variation in shear layer behaviour can cause transitions between flow regimes to happen at different times along the height of the cylinder as opposed to abrupt changes as the entire shear layers reattach or begin shedding as vortices, as found by Luo et al. (1996) with AR = 8 cylinders at P/D = 3.0 for the height between z/D = 0.65 and 0.85.

Finite-height effects are also apparent on cylinders in a side-by-side configuration. Zhang et al. (2015) found that, as noted previously, C_D for finite-height cylinders is lower than that of infinite cylinders at similar P/D. The local spanwise (sectional) values of C_D and C_L are also a function of P/D for staggered finite cylinders, with Lui and Cui (2006) noting the cylinder-wall junction and free end regions showing local maximum values of C_D at larger P/D, while smaller P/D produced higher magnitude mid-span C_L with a gradient to zero near the free end. Reddy and Poddar (2008) performed experiments focusing on the P/D effects for side-by-side cylinders of AR = 8.95 and found that, similar to finite-height cylinders in a tandem configuration, proximity effects were present in the force data for larger spacing than found with infinite cylinders (up to $P/D \leq 3.0$). Additionally, the behaviour of the biased flow regime at small P/D was very sensitive to Re. A subcritical regime ($Re = 2.0\times10^5$) caused one cylinder to obtain a C_D higher than an isolated cylinder while the other cylinder had a C_D lower. Conversely, a supercritical regime ($Re = 6.5\times10^5$) caused both cylinders have C_D values closer to each other and above an isolated cylinder.

An important staggered configuration between tandem and side-by-side is the configuration associated with the "inner lift peak" found at small P/D. Infinite cylinders experience distinct local maximum values of C_L and St for the downstream cylinder at $\alpha = 9°$ (Sumner et al., 2005). For two finite cylinders, however, this inner lift peak is less prominent: Rooney et al. (1995) observed a broader peak in St at a wider incidence angle near $\alpha = 15°$; Taniguchi et al. (1982) observed similar behaviour in their C_L data for AR = 3 cylinders, with only $P/D = 1.2$ producing a distinctive peak, and $P/D \geq 1.35$ producing weaker, broad peaks similar to the "outer lift peak" described by Sumner et al. (2005).

In general, there is limited literature on the wind loading and vortex shedding of finite-height staggered cylinders. Thus, systematically varying AR, P/D, and α to explore the finite-height effects on C_D, C_L, and St is the focus of this thesis. Beyond the scope of this thesis, there are still areas of potential future work, include studying the effects of Re and δ/D. Additionally, flow visualization or particle image velocimetry could give valuable insight to the complicated vortex dynamics that occur in these highly three-dimensional flows.

Chapter 3 Experimental Apparatus

3.1 Introduction

An experimental approach was followed in the research described in this thesis. Measurements of the mean drag coefficient, C_D, mean lift coefficient, C_L, and Strouhal number, St, as functions of aspect ratio, AR, pitch ratio, P/D, and incidence angle, α, for two surface-mounted finite-height cylinders in a staggered configuration, were collected with the use of a low-speed closed-return wind tunnel at the University of Saskatchewan. The experimental methods used were similar to those of Sumner et al. (2004), Adaramola et al. (2006), Rostamy et al. (2012), and Igbalajobi et al. (2013) for an isolated finite-height cylinder, and to Sumner et al. (2005) and Li and Sumner (2009) for two staggered cylinders. Section 3.2 details the wind tunnel, freestream measurements, and flow conditions. Section 3.3 describes the cylinder models and turntable positioning system. Section 3.4 provides information on the measurement of the mean drag and lift coefficients, and Section 3.5 details the measurement of the Strouhal numbers.

3.2 Wind Tunnel and Freestream Measurements

The testing program made use of the low-speed closed-return wind tunnel in the Department of Mechanical Engineering at the University of Saskatchewan. A 100 hp, constant speed, variable pitch fan supplies the wind, which passes through a set of turbulence reduction screens comprised of a coarse mesh and a fine mesh. The airflow passes through an area reduction of 7:1 before entering the test section (measuring 1.96 m in length, 1.13 m in width, and 0.91 m in height). For a schematic of the wind tunnel, see Figure 3.1.

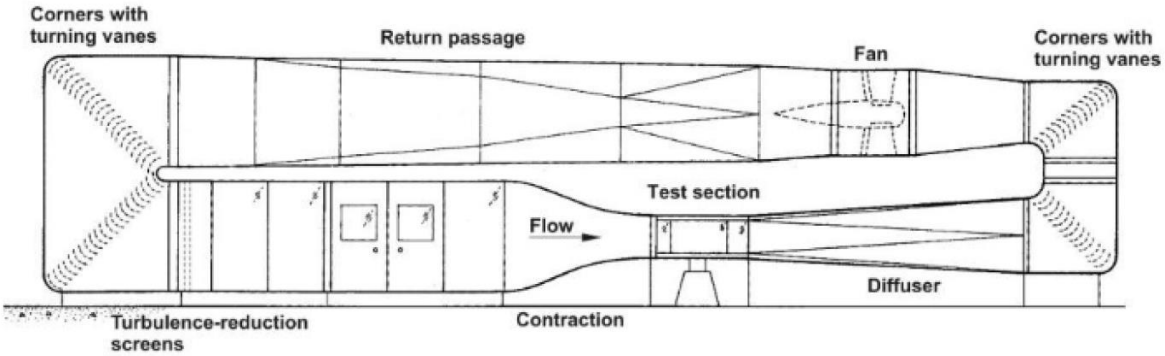

Figure 3.1: Low-speed, closed-return wind tunnel used for the experiments.

Instrumentation for measuring the freestream conditions was controlled by a desktop computer via LabVIEW Virtual Instruments (VI's). The data acquisition system used a 16-bit National Instruments PCIe-6295 card. The VI measuring the freestream static pressure, P_∞, dynamic pressure, q_∞, and temperature, T_∞, acquired 10,000 instantaneous samples at a rate of 1 kHz before averaging each of the individual parameters.

Measurements of the freestream static (P_∞) and stagnation (P_0) pressure were made with a 3.2 mm United Sensor Pitot-static probe mounted from the side wall of the test section. The static pressure (P_∞) line was connected to a Datametrics Barocel Type 600A-1000T-513-H21X-4 absolute pressure transducer and the reference side of a Datametrics Barocel Type 590D-10W-2QB-VIX-4D differential pressure transducer. The stagnation pressure (P_0) line was connected to the opposing inlet of the differential pressure transducer providing the measurement of the freestream dynamic pressure, $q_\infty = P_0 - P_\infty$, for use in calculating the freestream velocity (U_∞). The United Sensor Pitot-static probe affixed to the test section wall also contained a T-type thermocouple for measuring the freestream temperature (T_∞).

Using the averaged measured values of P_0, P_∞, and T_∞, the freestream air density (ρ_∞), dynamic viscosity (μ_∞), U_∞, and Reynolds number (Re) were calculated. The density was calculated using the ideal gas law, $\rho_\infty = P_\infty/RT_\infty$, where R (= 287 J/(kg·K)) is the specific gas constant for air. The dynamic viscosity was calculated using Sutherland's Law,

$$\mu_\infty = \mu_0 \frac{(T_\infty/T_0)^{3/2}(T_0+S)}{(T_\infty+S)} \ , \tag{3.1}$$

where the constants are chosen for air at a specific reference temperature ($\mu_0 = 1.725\times10^{-5}$ kg/(m·s), $T_0 = 273$ K, and $S = 110.4$ K). The freestream velocity was calculated from the freestream dynamic pressure using equation 3.2.

$$U_\infty = \sqrt{2\frac{q_\infty}{\rho_\infty}} \tag{3.2}$$

Conditions for the experiments were dictated by U_∞, and it was manually set such that the Reynolds number, Re (= $\rho_\infty U_\infty D/\mu_\infty$ where $D = 31.5$ mm is the cylinder diameter) was $6.5 \pm 0.1\times10^4$. The wind tunnel did not have any form of active temperature control, therefore the slowly rising temperature that occurred throughout each test had the effect of slowly reducing Re. Each test conducted remained within a Re range of 6.4×10^4 and 6.6×10^4, however.

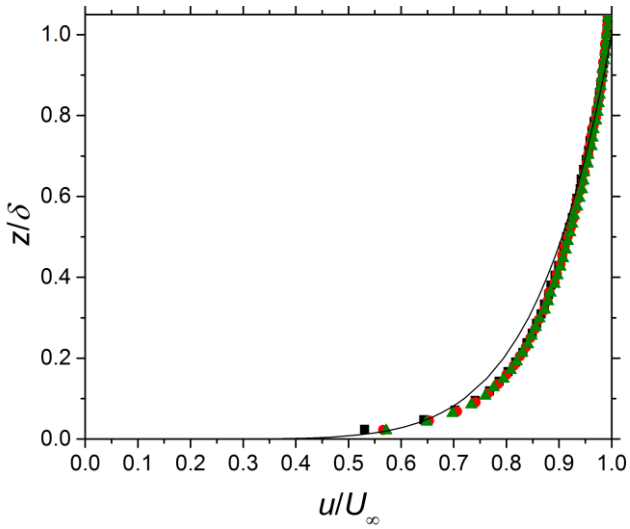

Figure 3.2: Boundary layer mean streamwise velocity profile at $x/D = -5.0$ (■), $x/D = 0$ (●), $x/D = 5.0$ (▲), and the 1/7th power law (–), where $x/D = 0$ is the location of the central cylinder.

The wind tunnel ground plane was a flat plate of aluminum with a rounded leading edge 897 mm upstream from the centre of the instrumented central cylinder (of the pair of staggered cylinders). A fully turbulent boundary layer was developed over the ground plane with a thickness defined as the vertical position, z, where the local streamwise velocity, $U(z)$, achieved 99% of U_∞. The velocity profile, $U(z)$, was calculated using the stagnation pressure measured with a 0.85 mm diameter boundary layer Pitot probe and P_∞ from the freestream Pitot-static probe. These pressures were connected to a Validyne Model P55D differential pressure transducer to acquire the local dynamic pressure used to calculate the local velocity in a similar manner as the freestream velocity. The boundary layer characteristics for the streamwise position of the central cylinder as well at 5D upstream and downstream may be found in Table 3.1. The respective non-dimensional velocity profiles may be found in Figure 3.2 alongside the 1/7th power law for a turbulent boundary layer.

Table 3.1: Ground plane boundary layer characteristics with respect to central cylinder position.

x	δ [mm] (δ/D)	δ^* [mm] (δ^*/D)	θ [mm] (θ/D)	δ^*/θ
−5D	42 (1.3)	4.4 (0.1)	3.6 (0.1)	1.2
0D	44 (1.4)	4.5 (0.1)	3.7 (0.1)	1.2
5D	47 (1.5)	4.8 (0.1)	3.9 (0.1)	1.2

3.3 Cylinder Models and Positioning

The wind tunnel models representing surface-mounted finite-height cylinders in a staggered configuration (Figure 3.3) were machined out of solid aluminum on CNC machines. For the four pairs of cylinders the diameter was D = 31.5 mm, with heights of H = 283.5, 220.5, 157.5, and 94.5 mm providing AR = 9, 7, 5, and 3, respectively. The solid blockage ratio of the cylinders was minimal, with two AR = 9 cylinders in a side-by-side configuration providing a blockage of only 1.7 %. The eccentricity, surface roughness, and tolerance in H and D due to machining were considered negligible compared to the uncertainty in the mounting and positioning of the cylinders. The central cylinder was positioned with a centering ring to the force balance as seen in Figure 3.4. Though the central cylinder was machined to a small tolerance, thermal effects associated with the heating of the wind tunnel caused the ground plane to lift up past the bottom edge of the cylinder when tests were conducted. The swelling was limited to under 2 mm, which for the AR = 3 cylinder provides an uncertainty of ~2 %.

Systematic variation of P/D and α was accomplished using the turntable shown in Figure 3.5 and Figure 3.6. Holes in the turntable were drilled to mount the outer cylinder at P/D = 1.125, 1.25, 1.5, 1.75, 2.0, 2.25, 2.5, 2.75, 3.0, 3.5, 4.0, and 4.5. A large pulley was attached to the bottom of the turntable along with a securely fastened timing belt. A stepper motor controlled by a VI on the main computer allowed for full control over the turntable and outer cylinder angle (α). For specification on the speed of angular rotation, see Table 4.4 in Section 4.3.4.

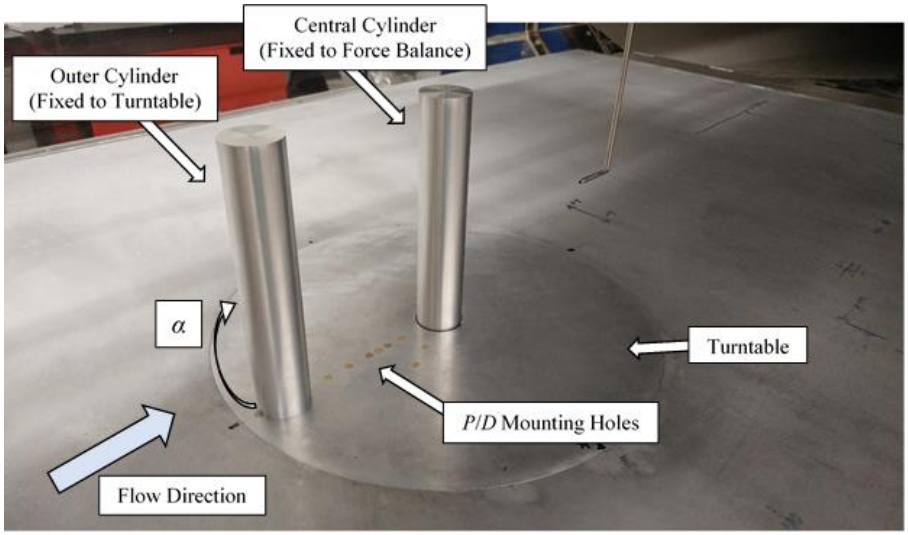

Figure 3.3: Staggered cylinder apparatus in the wind tunnel.

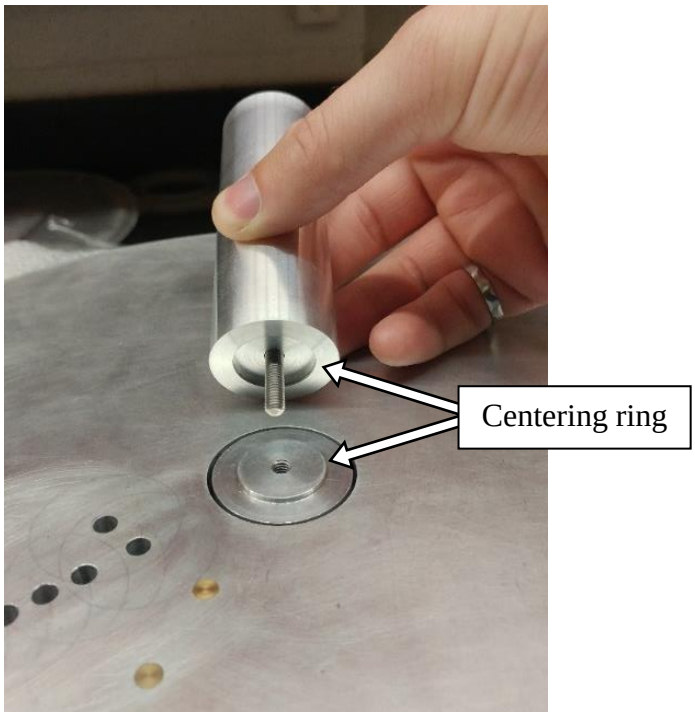

Figure 3.4: Central cylinder connection to force balance.

The assembly and operation of the apparatus induced a small uncertainty into P/D and α (values summarized in Table 3.2). Unlike the central cylinder, the outer cylinder was not sensitive to T_∞ although it did not utilize a centering ring to set P/D. The bolted connection through a clearance hole in the aluminum turntable resulted in an uncertainty in P of ± 0.2 mm. Additionally, the ground plane (connection to the outer cylinder) and force balance (connection to central cylinder) were not connected, and the ground plane could move approximately 0.5 mm in any direction. This resulted in a total uncertainty in P of ± 0.7 mm, which at its most severe (P/D = 1.125) is ~2 %. The stepper motor and timing belt could only provide precision to ± 0.5° and this coupled with the centering uncertainty provided an angular uncertainty of ± 1.6° at its most severe (P/D = 1.125).

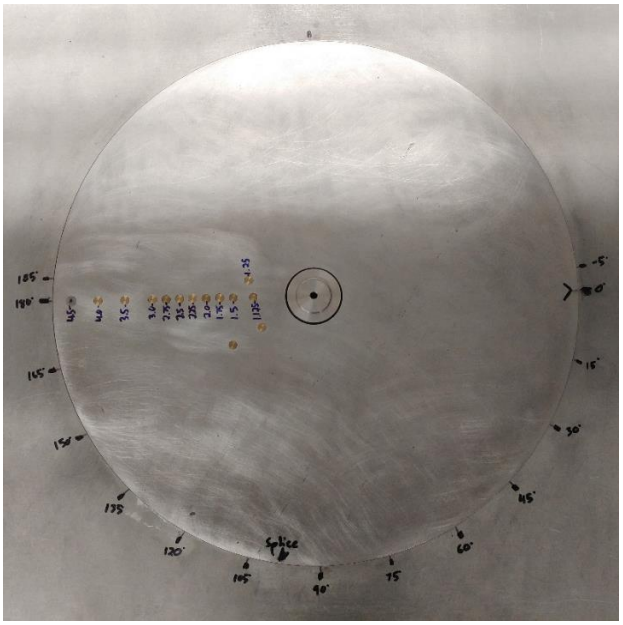

Figure 3.5: The turntable with outer cylinder mounting holes to set *P*/*D* (filled with brass plugs to have a smooth upper surface). The turntable rotates from $\alpha = -5°$ to 185° in increments of 1°. The central cylinder mounts to the force balance adapter in the centre of the turntable.

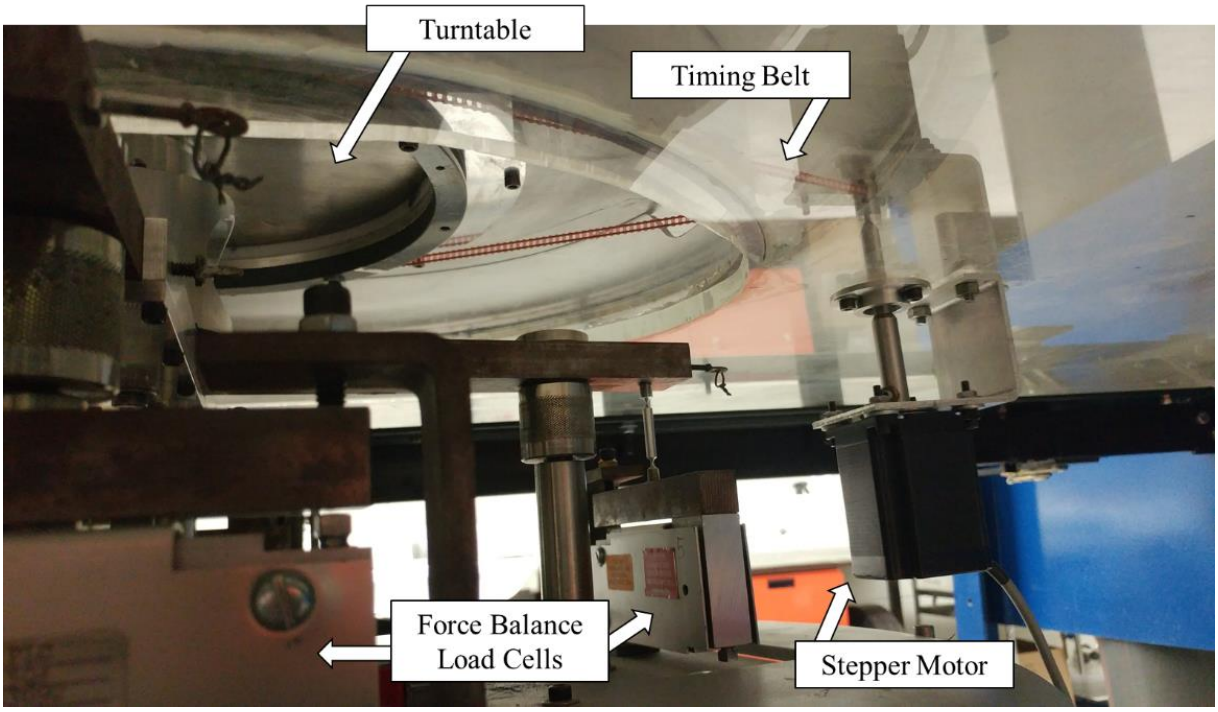

Figure 3.6: An underside view of the ground plane. The stepper motor rotates the turntable via a timing belt.

Table 3.2: Uncertainty in P/D and α at all P/D tested.

	Uncertainty			
P/D	P [mm]	P/D [mm]	P/D [%]	α [°]
1.125	± 0.7	± 0.02	± 2.0	± 1.6
1.25	± 0.7	± 0.02	± 1.8	± 1.5
1.5	± 0.7	± 0.02	± 1.5	± 1.3
1.75	± 0.7	± 0.02	± 1.3	± 1.2
2.0	± 0.7	± 0.02	± 1.1	± 1.1
2.25	± 0.7	± 0.02	± 1.0	± 1.1
2.5	± 0.7	± 0.02	± 0.9	± 1.0
2.75	± 0.7	± 0.02	± 0.8	± 1.0
3.0	± 0.7	± 0.02	± 0.7	± 0.9
3.5	± 0.7	± 0.02	± 0.6	± 0.9
4.0	± 0.7	± 0.02	± 0.6	± 0.8
4.5	± 0.7	± 0.02	± 0.5	± 0.8

3.4 Measurements of C_D and C_L

The measurement of the mean drag coefficient, C_D (= $2F_D/(\rho_\infty U_\infty^2 DH)$), and mean lift coefficient, C_L (= $2F_L/(\rho_\infty U_\infty^2 DH)$), were made at the central cylinder by a six-component force balance made of six HBM PLC single point load cells. The calibration used three of the load cells and measured the mean drag force, F_D, mean lift force, F_L, and mean pitching moment, M_P, simultaneously. Only the drag force and lift force were of interest in the present research, and the orientation of the forces can be found in Figure 3.7. Drag was oriented along the streamwise direction, and the sign of the lift was such that a positive lift represented a repulsive force away from the other cylinder. Typical values of F_D for a 31.5 mm diameter cylinder immersed in a 35 m/s freestream are 5 N and 1.5 N for AR = 9 and 3 respectively. The data acquisition was controlled by a VI on the main computer, and each data point represented the average of 10,000 instantaneous samples taken at 1 kHz.

The total uncertainty in C_D and C_L (Table 3.3) was calculated as the root-sum-square of the individual uncertainties associated with the force balance calibration, the offset (zero load) drift, and variance in repeated measurements. The uncertainty in the force balance calibration was based on a standard error estimate computed from the response equations for the force

balance. As the smaller AR cylinders produced smaller wind loads, the relative magnitude of the calibration uncertainty was larger, though this uncertainty represented the largest contribution to the total uncertainty for all AR. Additionally, the voltage offsets of the load cells were sensitive to T_∞ and extended tests would result in a small drift. It was assumed that for most configurations load cell 1 (primarily responsible for measuring drag) would experience the highest load. It was also found that load cell 1 was showed the highest temperature sensitivity. Therefore load cell 1 was used as the metric for maximum offset drift, and at the end of each experiment if the offset for load cell 1had drifted farther than 2 % of the value of C_D for an isolated finite cylinder of the same AR, the test would be rejected. Finally, the mean drag and lift forces were measured ten times for each AR with only one isolated cylinder, to provide a standard random uncertainty estimate. For all AR this type of uncertainty was very small relative to the uncertainty from the force balance calibration and the temperature sensitivity. For a summary of the total uncertainty in C_D and C_L see Table 3.3. For reference, across all measurements made in this thesis research, the force coefficients ranged from $-0.4 < C_D < 1.4$ and $-1.1 < C_L < 0.7$.

For a representative example of the uncertainty, the measured values at $P/D = 2.0$ and $\alpha = 90°$ are used: i) AR = 9, $C_D = 0.93 \pm 0.03$ and $C_L = 0.11 \pm 0.02$; ii) AR = 7, $C_D = 0.91 \pm 0.03$ and $C_L = 0.11 \pm 0.02$; iii) AR = 5, $C_D = 0.89 \pm 0.04$ and $C_L = 0.09 \pm 0.02$; and iv) AR = 3, $C_D = 0.87 \pm 0.07$ and $C_L = 0.08 \pm 0.03$.

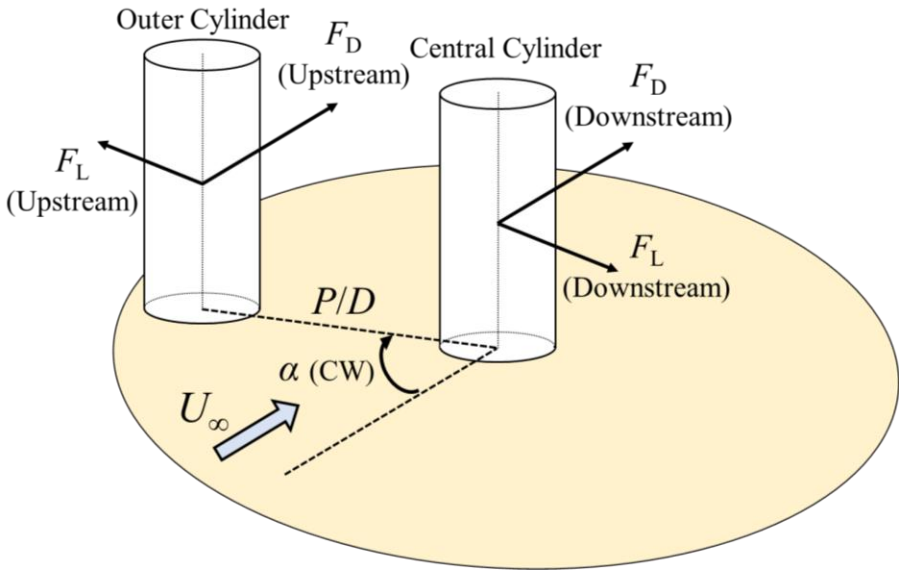

Figure 3.7: Force convention for staggered cylinder data.

Table 3.3: Uncertainty in force balance measurements at a 95 % confidence level.

AR	F_D [N]	F_L [N]	C_D [-]	C_L [-]
9	± 0.16	± 0.12	± 0.03	± 0.02
7	± 0.14	± 0.09	± 0.03	± 0.02
5	± 0.13	± 0.08	± 0.04	± 0.02
3	± 0.13	± 0.06	± 0.07	± 0.03

In order to systematically test the effects of AR, P/D, and α on C_D and C_L, a systematic test trajectory was developed. Initially the highest AR cylinders were mounted in the wind tunnel at the largest P/D. Forces were then measured from $\alpha = -5°$ to 185° in increments of 1°, with the central cylinder representing a downstream cylinder from $\alpha = -5°$ to 89° and an upstream cylinder from $\alpha = 91°$ to 185°. Once forces were measured at all α for the given AR and P/D, the outer cylinder was incremented to a smaller P/D and the entire α range was completed again. Then, once the forces were measured for all α and P/D at a given AR, the cylinders were swapped out for the next lowest AR and the cycle was repeated until force data had been captured for every combination of AR, P/D, and α. Special attention was given to small P/D (< 2.0) as a significant difference was found in the wind loads for certain combinations of AR and P/D near $\alpha = 90°$ (side-by-side) depending on whether α was increasing or decreasing. Thus, for small P/D, α was also varied from 185° to −5° in an increment of −1°. This hysteresis phenomenon is discussed at length in Section 4.3.4.

3.5 Measurements of St

The measurement of Strouhal number, St (= fD/U_∞), was completed for both upstream and downstream cylinders simultaneously at all of the AR and P/D combinations outlined previously in Section 3.4. The experimental apparatus for measuring St is shown in Figure 3.8. Velocity fluctuation power spectra were measured using a six-channel Dantec Streamware constant-temperature anemometer unit and two single-wire hot-wire probes. Time series voltage fluctuations for each probe were sampled for 1 s, and a fast Fourier transform was used to separate the signals into their component frequencies. Thirty (30) consecutive samples were averaged over 30 s for each configuration, and local peaks in the averaged power spectra were taken as the dominant vortex shedding frequencies and non-dimensionalized into values of St. A stationary probe holder was positioned behind the central cylinder and held a Dantec 55P11 straight single-wire probe. A Dantec 55P15 boundary layer single-wire probe was affixed to a traversing probe holder that was controlled by a VI on the main computer; this probe followed behind the outer cylinder as AR, P/D, and α were incremented.

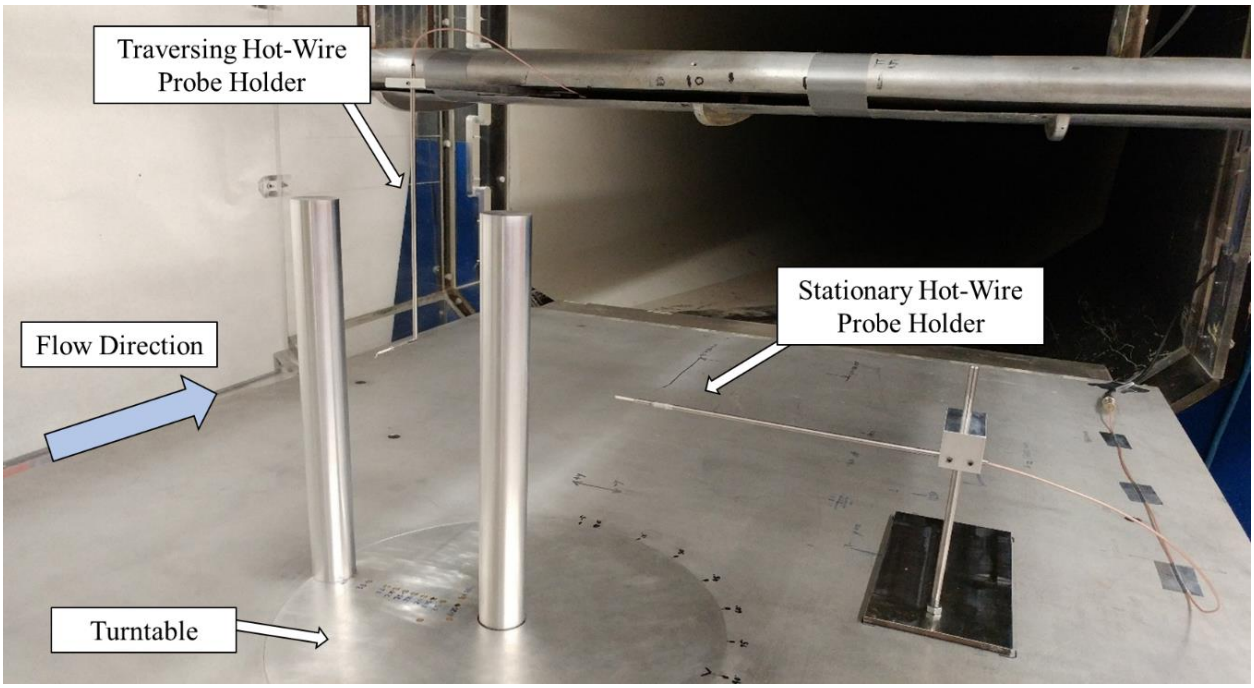

Figure 3.8: Full St measurement apparatus. AR = 9 cylinders shown in a side-by-side configuration at P/D = 4.5.

The positions of the probes relative to the cylinders were held constant for most configurations at $x/D = 3.0$, $y/D = 1.0$ (on the outer side), and $z/H = 0.5$ as seen in Figure 3.9 in the context of the upstream cylinder. For smaller P/D that produced more proximity interference and larger flow deflection angle, $y/D \leq 1.8$ was used to increase the clarity of the spectral peaks. The uncertainty in the position of the traversing system was very small, and therefore the uncertainty in the actual position of the outer cylinder as described in Table 3.2 represents the uncertainty in the traversing hot-wire probe's position. The central cylinder was fixed, however the stationary hot-wire probe was manually positioned to within an uncertainty of 1 mm in each direction representing less than a 3 % uncertainty in its position. The largest uncertainty associated with St was selecting the peaks from the velocity fluctuation power spectra. For reference, the typical vortex shedding frequencies for 31.5 mm diameter cylinders immersed in a 35 m/s freestream are approximately 200 Hz and 170 Hz for AR = 9 and 3 respectively. For many of the larger P/D with sharp well-defined peaks, the dominant frequency only varied by ~5 Hz (less than 4 % of the dominant frequency). The weaker vortex shedding found with AR = 3 produced weaker peaks that were more challenging to define, with an uncertainty upwards of 10-15 %. Configurations at small incidence angles near the inner lift peak (as described at length in Section 4.4.3) often did not show discernable peaks at all, and, if there were peaks, the uncertainty was often on the order of 25 %.

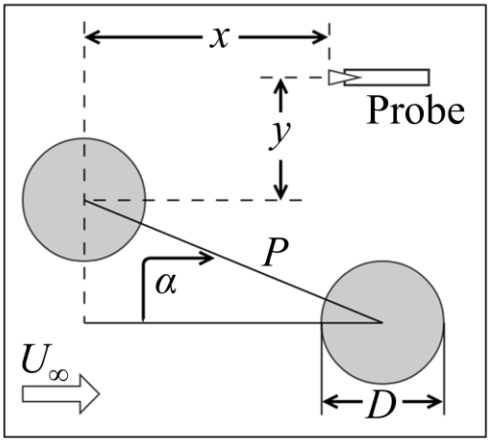

Figure 3.9: Schematic of traversing hot-wire probe positioning for upstream cylinder St measurement.

Systematic variation of AR, P/D, and α was accomplished in a similar manner as for C_D and C_L. The largest AR cylinders were mounted at the largest P/D, then α was incremented from 0° - 95° in increments as described in Appendix A. As St for both the upstream and downstream cylinders were measured simultaneously by two probes, the entire α range of the turntable was not required. Once α was finished incrementing, P/D was incremented down to the next largest mounting hole. Once all α and P/D were completed for a given AR, the cylinders were swapped for the next lower AR and the process continued. For AR and P/D configurations that previously resulted in hysteresis, measurements above $\alpha = 95°$ were made as well as with incrementing α in the negative direction. For several reasons as discussed in Section 4.4.3, hysteresis near $\alpha = 90°$ was not apparent in the St data as it was for C_D and C_L.

Chapter 4 Results and Discussion

4.1 Introduction

In the present research, measurements of C_D, C_L and St were made for both the upstream and downstream finite cylinders for each staggered configuration, while AR, P/D, and α were systematically varied. By comparing these results to data for two infinite cylinders in a staggered configuration (from Sumner et al. (2005) and other studies in the literature), the influence of finite-cylinder height and the presence of the ground plane can be better understood.

The overall results from the research show that AR has a significant effect on the magnitudes of C_D, C_L, and St, the directions of C_D and C_L in some of the cases, the behaviour of C_D, C_L, and St with α, as well as the P/D boundaries between the various flow patterns. The results are presented in the following sections primarily with respect to how C_D, C_L, and St vary with α, for given ranges of P/D and values of AR (similar to the approach adopted by Sumner et al. (2005) and Li and Sumner (2009)). Also discussed are the general trends found in the C_D, C_L, and St data with respect to AR and P/D. Section 4.2 describes the findings for the two finite-height cylinders in a tandem configuration ($\alpha = 0°$). Section 4.3 shows the results for the two finite-height cylinders in a side-by-side configuration ($\alpha = 90°$), with an additional discussion on hysteretic behaviour found for closely spaced cylinders near $\alpha = 90°$. Section 4.4 details the findings for the two finite-height cylinders in the more general staggered configuration, i.e., for α between 0° and 90°.

Based on earlier work using similar cylinders in the same wind tunnel, at similar Reynolds numbers and boundary layer thicknesses (Sumner et al., 2004; Adaramola et al., 2006; Igbalajobi et al., 2013; Rostamy et al., 2012; Sumner et al., 2015), it was known that the cylinders of AR = 3 were below the critical aspect ratio. Therefore, the results for the cylinders of AR = 3 were expected to show distinct behaviour compared to AR = 5, 7, and 9.

4.2 Tandem Finite-Height Cylinders

Cylinders arranged in tandem ($\alpha = 0°$) such that the upstream cylinder shields the downstream cylinder from the incident freestream represent one of the most basic configurations of staggered cylinders. Three main flow types (Section 2.2.1) are well-documented for infinite cylinders with P/D being a major influence at a constant Re. Closely spaced cylinders ($P/D \leq 1.125$) represent the extended-body regime, moderately spaced cylinders ($P/D = 1.25 – 4.0$) represent the reattachment regime, and widely spaced cylinders ($P/D > 4.0$) represent the co-shedding regime. Key features of C_D and St with respect to varying AR and P/D (as found in Figure 4.1 and Figure 4.2) are discussed in the following sections. Since both cylinders in the tandem configuration are aligned with the flow, there is no mean lift force experienced by the cylinders.

4.2.1 Mean Drag Coefficient

Mean drag coefficient (C_D) data for both the upstream and downstream cylinders in the tandem configuration, with varying P/D, are shown in Figure 4.1. The behaviour of C_D with P/D demonstrates clearly how the wind loading of the two cylinders can be drastically different because of wake interference effects.

For the upstream finite cylinder, the behaviour of C_D is mostly similar to that of two infinite cylinders, but the magnitude of C_D is lower. The discontinuous jump in C_D seen for infinite cylinders at higher P/D, which occurs at the boundary between the reattachment and co-shedding regimes, is not seen in the finite-cylinder C_D data. It is possible that this jump has shifted to a higher pitch ratio, beyond the range ($P/D = 1.125$ to 4.5) considered in the present research. As the vortex formation length is longer for finite cylinders (Igbalajobi et al., 2013), the critical spacing needed to attain co-shedding (vortex shedding from both cylinders) may be greater than the maximum pitch ratio ($P/D = 4.5$) tested. However, with the variation of the vortex formation length along the heights of the finite cylinders, it may be that the discontinuity seen for tandem infinite cylinders has been smoothed out or eliminated. In other words, as the vortex formation length of a finite cylinder varies along its span it is possible that no clear jump may exist at all as different points along the span may develop vortices gradually as P/D is increased.

The complexity of the flow in the gap between two tandem finite cylinders can be seen in the results of Kim and Christensen (2018), for two cylinders of AR = 2.37. At P/D = 2.0 they showed two counter-rotating recirculation zones in the gap flow, one at the mid-height and the other near the ground plane. This may indicate that the reattachment found at the mid-height location does not extend fully to the fixed end of the cylinder, resulting in weak co-shedding near both ends of the cylinders coexisting with reattachment at the mid-height.

If a very small increment in P/D had been used in the present research, it may have been possible to better clarify the behaviour of C_D at higher pitch ratios. The result may be a smooth continuous transition in C_D as the co-existing reattachment and co-shedding regimes contribute less and more, respectively, to the overall flow field. Perhaps the finite cylinders never truly experience the reattachment regime across their entire height, as the tip and base vortices interfere with the shear layers at both ends of the cylinder, and downwash continues to enter the gap between the cylinders, more so as the cylinders are spaced farther apart. Further discussion follows in Section 4.2.2 alongside presentation of the St data.

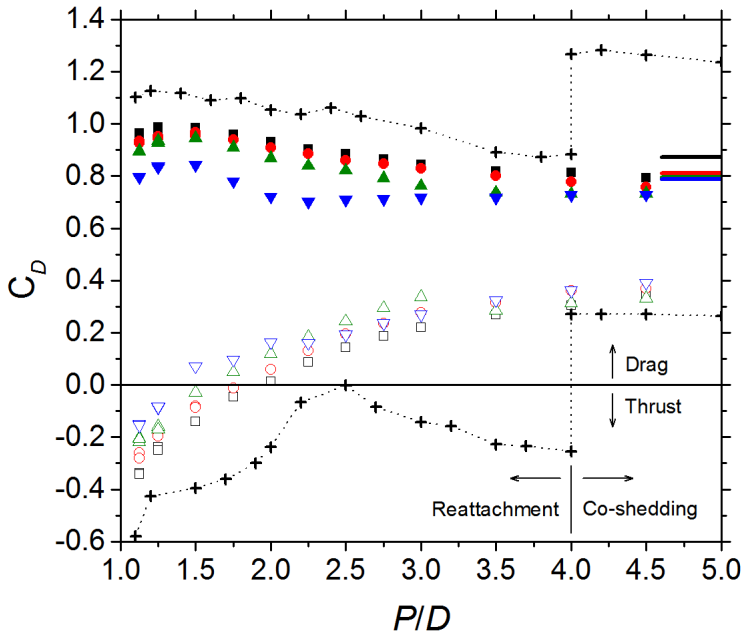

Figure 4.1: Mean drag coefficient, C_D, data for upstream (closed symbols), downstream (open symbols), and isolated (solid colour line) cylinders in tandem as function of P/D and AR: ■/□/–, AR = 9; ●/○/–, AR = 7; ▲/△/–, AR = 5; ▼/▽/–, AR = 3; and +, infinite (Alam et al., 2003b).

For the downstream cylinder, the C_D data for the finite cylinders are shifted upwards compared to the data for the infinite cylinders, resulting in a weaker thrust force at low pitch ratios but a higher drag force elsewhere; the wake interference effects are basically weaker for finite cylinders. The range of P/D where the downstream cylinder experiences a thrust force is also greatly reduced for the case of the finite cylinders which may be due to the effects of downwash. Similar to what is seen for the upstream cylinder, a discontinuous jump in C_D for the downstream cylinder at higher pitch ratios is not apparent, in contrast to what is seen for two infinite cylinders in tandem. This may be due to the gradual increase of freestream impingement (onto the downstream cylinder) as P/D increases. At the P/D where the mid-span shear layers completely roll up into vortices, the portion of the span that actually results in vortex impingement is of comparable size to the portion of the span that contains entrained freestream, causing the "jump" to have a diminished effect on C_D.

It is possible that if a smaller increment in P/D had been used in the present research, a small discontinuous change in C_D for the downstream cylinder could have been detected (it might have better captured the downstream cylinder leaving the recirculation region behind the upstream cylinder, which may result in an abrupt change in drag alongside the onset of co-shedding). A change in shear layer reattachment behaviour will have an effect on the entire surface of the downstream cylinder and its near wake as opposed to just the near wake of the upstream cylinder, which may result in a more obvious change in C_D. A smaller increment in P/D would also have been beneficial between $P/D = 1.25$ and 1.5, where shear layer interaction with the downstream cylinder is very strong and the magnitude of C_D is changing rapidly.

When compared directly to infinite cylinder tandem data from Alam et al. (2003b) (Figure 4.1) at the widest $P/D = 4.5$, the upstream finite cylinder has a far lower C_D, likely from the residual reattachment experienced by finite cylinders as opposed to the co-shedding experienced by infinite cylinders at this P/D. The downstream finite cylinder has a C_D slightly higher than the infinite cylinder, possibly due to the freestream impingement causing a larger drag on the upper portion of the cylinder than would have been felt from lower momentum vortex impingement in the infinite case.

Aspect ratio was found to have a large effect on C_D across much of the P/D range shown in Figure 4.1. From the perspective of the upstream cylinder, a decrease in AR corresponds to a decrease in C_D for all P/D considered. This could be due in part to the lower AR cylinders being more fully immersed in the lower momentum ground-plane boundary layer. Additionally, the increased significance of downwash behind the upstream cylinder at lower aspect ratio may entrain more high energy flow into the gap region, increasing base pressure near the free end and reducing C_D. The upstream cylinder for AR = 3 has a significantly lower C_D for $P/D < 3.0$, which may be a consequence of being below the critical aspect ratio, giving the cylinder different near wake characteristics. As the finite cylinders of AR = 3 have a significantly different near-wake structure than cylinders that are above the critical AR, it follows that the P/D range that is strongly influenced by shear layer reattachment should also be different for AR = 3. Drag coefficient data for all four aspect ratios tested asymptotically approach a lower C_D than their respective isolated cylinder, with lower aspect ratio cylinders approaching these values quicker. For AR = 3, C_D measured for the upstream cylinder becomes independent of pitch ratio for $P/D \geq 2.0$; this coincides with the maximum extent of the mean recirculation region, found at $x/D = 2.0$ by Rostamy et al. (2012) for an isolated finite cylinder of AR = 3. This would suggest that once the pitch ratio exceeds 2.0, the downstream cylinder no longer sits within the recirculation zone of the upstream cylinder, and therefore the zone's effect is greatly reduced. In a similar fashion for finite cylinders above the critical aspect ratio (AR = 9,7, 5), the maximum extent of the mean recirculation zone is higher, extending to $x/D = 3.0 – 4.0$ (Rostamy et al., 2012). Consequently, for tandem finite cylinders above the critical aspect ratio, the drag coefficient becomes independent of pitch ratio at higher P/D.

In the context of the downstream cylinder, for cylinders above the critical AR (cylinders of AR = 9, 7, 5) the AR effects across the entire P/D range tested can be observed in Figure 4.1. As AR decreases from AR = 9 to AR = 5, more of the downstream cylinder's height is exposed to downwash impinging on it from the cylinder upstream, providing a more consistent level of drag on the downstream cylinder than the various shear layer interactions found as P/D increases from 1.125 to 4.5. Consequently for $P/D \leq 3.0$, the AR = 5 configuration has a higher C_D than AR = 7 and AR = 9 as it benefits less from the shear layer reattachment that occurs over a smaller portion of its span. Conversely for $P/D > 3.0$, where shear layer reattachment potentially only occurs over a small band in the middle and lower portion of the cylinders, where the vortex

formation length is the longest, the shorter AR = 5 cylinder has a lower C_D than AR = 7 and AR = 9 as a larger portion of its span is within the lower momentum boundary layer.

Aspect ratio has a large effect on C_D measured for the downstream cylinder at smaller P/D (found in Figure 4.1). The mean thrust force experienced by the downstream cylinder, which occurs for $P/D < 4.0$ for infinite cylinders (Alam et al., 2003b), becomes weaker and occurs over a more limited range of P/D as AR is decreased. For AR = 9, the downstream cylinder experiences a mean thrust force for $P/D < 2.0$ whereas for AR = 3 it only occurs for $P/D < 1.5$. Though the longer and wider near wake found at lower AR might tend to extend the P/D range where a thrust force is found, stronger downwash behind the upstream cylinder may cause more of the higher momentum freestream fluid to impinge on the leading face of the downstream cylinder near its free end, thereby increasing its C_D (making it less negative, as the case may be). The base vortices also disrupt the shear layer reattachment near the cylinder-wall junction which increases the pressure in the gap region, with a similar effect from the tip vortices. Ultimately, an increase in C_D (reduction in thrust) for the downstream cylinder results. As AR is decreased the very high thrust forces found at very small P/D become further suppressed.

4.2.2 Strouhal Number

The Strouhal number (St) was measured for both cylinders simultaneously at their mid-height via two hot-wire probes and the data may be found in Figure 4.2. The probe associated with the downstream cylinder was affixed to a stationary probe holder, while the probe associated with the upstream cylinder was affixed to a computer-controlled traversing system able to reposition the probe during tests. As repositioning the stationary probe required the wind tunnel to be shut down, it was not feasible to take St data as a function of position relative to the cylinder. Consequently, the streamwise and transverse positions (relative to the centre-line of the cylinders) of the probes were fixed for all measurements. From the power spectra of the velocity fluctuations, the vortex shedding frequency was identified as the strongest peak (in some cases more than one peak was identified). The traversing probe was initially used to identify the streamwise (between $x/D = 2.5$ and 3.0) and transverse (between $y/D = 1.0$ and 1.8) position that provided the sharpest power spectra peak for both the upstream and downstream cylinders. Following the selection of probe positions, the stationary probe was manually set behind the

downstream cylinder while the traversing probe was positioned behind the upstream cylinder allowing for a simultaneous measurement of the power spectra. Though the height of the probe relative to the cylinders has an effect on the power spectra measured, only measurements at the mid-height were conducted for simplicity in the experiments and for the stronger vortex shedding found away from the ends of the cylinders.

Considerably more scatter was found in the St measurements, in terms of the dependence on P/D, than with C_D, due to the spectral peaks becoming less defined as AR was reduced, representing a weakening of the vortex shedding (at the location of the hot-wire probe in the wake, specifically). The following section discusses the effects of P/D, then the effects of AR and spanwise (heightwise) variation in flow regime in the context of St.

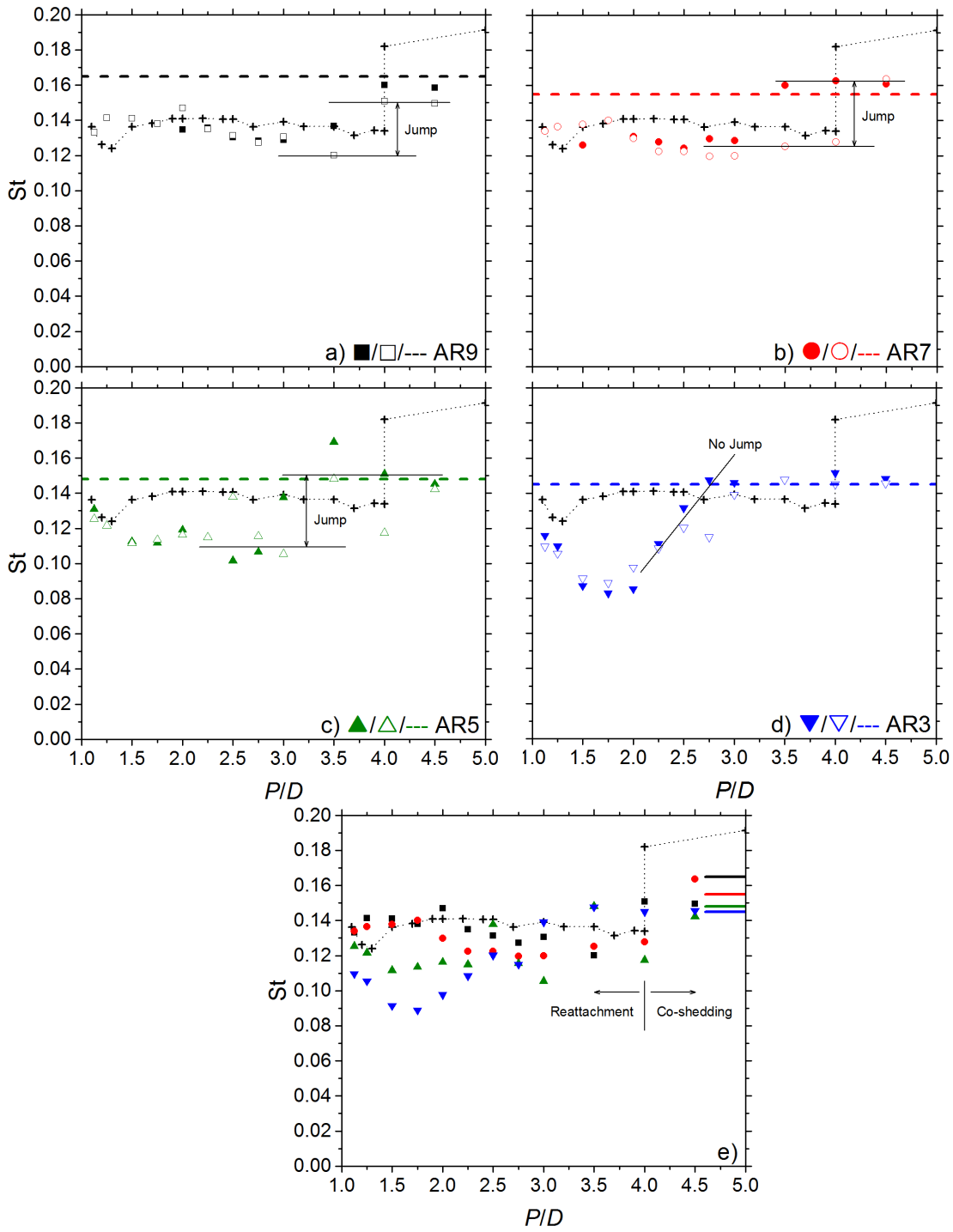

Figure 4.2: Strouhal number, St, measured at mid-height for upstream (closed symbols), downstream (open symbols), infinite (+ from Alam et al., 2003b) and finite-height isolated (solid colour lines, from Wang et al. (2012)) cylinders in tandem as functions of *P*/*D* and AR: a) ■/□/– AR = 9; b) ●/○/– AR = 7; c) ▲/△/– AR = 5; d) ▼/▽/– AR = 3; and e) only downstream cylinder data shown for all AR alongside infinite data from literature.

From the results in Figure 4.2, it can be seen that both the upstream and downstream cylinders have the same values of Strouhal number, which is consistent with the results in the literature for two infinite cylinders, i.e., there is one dominant frequency in the flow field for cylinders in tandem.

For $P/D < 3.0$ (Figure 4.2) the upstream and downstream cylinders at a given AR have similar values of St that are lower than those found with an isolated cylinder of the same AR. Falling within the extended-body and shear layer reattachment regimes, it follows that the two cylinders acting together as one larger body would shed vortices at a lower frequency than one of the bodies on its own, consistent with what is seen for a finite cylinder with a splitter plate (Igbalajobi et al., 2013). For the larger AR (AR = 9 and 7), the value of St increases from P/D = 1.125 to P/D = 1.25. This marks the transition from extended-body to shear layer reattachment as the reattached shear layers produce a narrower near wake with a higher shedding frequency than found in the extended-body regime. As P/D increases from 1.25 the value of St gradually reduces as the reattached shear layers still cause the cylinders to behave as one pseudo-body, only one that is increasing in effective length. At P/D = 3.5 for AR = 9 and 7 (P/D = 3.0 for AR = 5) the upstream cylinder seems to experience a small increase or jump in St corresponding to the onset of co-shedding. Past this critical P/D the values of St for the upstream cylinder become reasonably close to those of their respective isolated finite cylinders.

As found in Figure 4.2a at AR = 9, both the upstream and downstream cylinders have the same critical values of pitch ratio, between P/D = 3.5 and 4.0.The finite cylinders of AR = 7 and AR = 5 have different critical P/D for the upstream and downstream cylinders, however, more data are needed to make conclusions about the delay in downstream cylinder critical P/D. Measurements made in a similar fashion as the present study (dual hot-wire probes simultaneously measuring velocity fluctuation power spectra) could be expanded to a fine increment of height along the cylinders in the range where the onset of co-shedding is delayed (P/D between 3.0 and 4.0). As there is likely no exact boundary between flow regimes and the production of vortices at each height is likely intermittent, a shorter time period for each power spectra measurement made several times may lead to more clarity in the spectra data as well.

The discrepancy in upstream and downstream critical P/D marking the onset of co-shedding (Figure 4.2d) is not apparent for AR = 3, as it is likely that the cylinders are too short to experience a large variance in flow regime along their height. In addition, the cylinders of AR = 3 experience a largely dissimilar near wake than higher-AR cylinders. Both the upstream and downstream cylinders have similar values of St across the entire P/D range, though the weaker vortex shedding does not allow for a sharp jump to the co-shedding regime. Instead, the cylinders both experience a steep increase in St from P/D = 1.75 to 2.75. If the two flow regimes (reattachment and co-shedding) are bi-stable over this P/D band with reattachment more likely near P/D = 1.75 and co-shedding more likely at P/D = 2.75, then the power spectra may show two spectral peaks. In fact, in Figure 4.3 the power spectrum for P/D = 2.75 shows two very small peaks, perhaps representing the intermittent switching between shear layer reattachment and co-shedding.

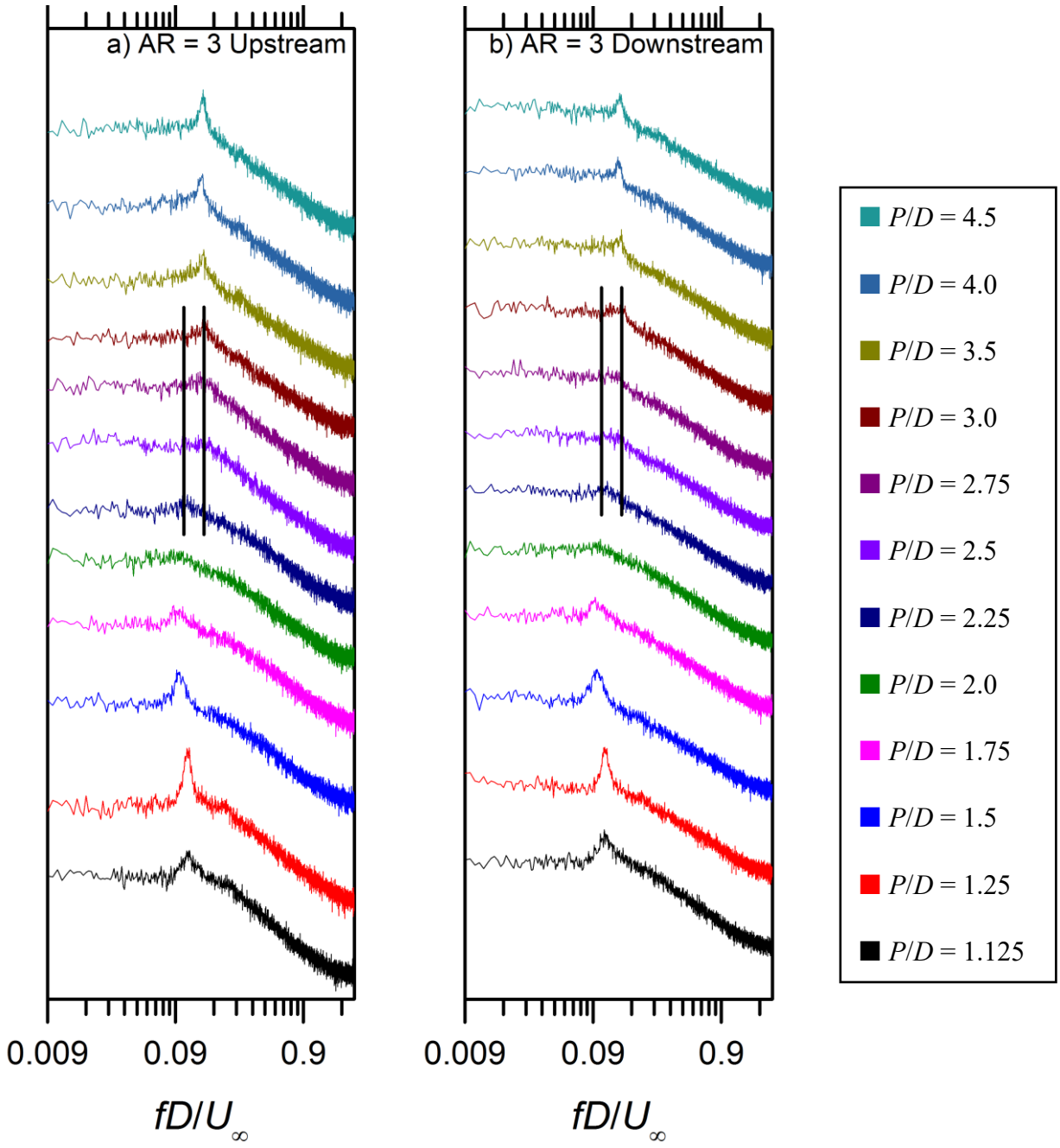

Figure 4.3: Velocity fluctuation power spectra for the AR = 3 cylinders in a tandem configuration for a) upstream and b) downstream cylinders. Vertical black lines are added to show the existence of two peaks in the power spectra.

Significantly more scatter was found in the St data (Figure 4.2c and Figure 4.2d) for the finite cylinders of AR = 5 and AR = 3. The vortex shedding for these lower-AR cylinders is weaker, and as a result the peaks in the power spectra are less defined. It can be seen in Figure 4.2e, however, that the AR = 5 and AR = 3 cylinders experience a largely different St trend than AR = 9 and AR = 7 for $P/D < 2.5$. In this region a lower aspect ratio correlates to a significantly lower St. Isolated finite-height cylinders also exhibit a decrease in St with decreasing AR. It is possible that the longer formation lengths found at lower AR coupled with the extended-body nature found with the shear layer reattachment regime could amplify this decrease in St. As a result, significantly lower values of St are possible with reduced AR and P/D.

From the data for C_D (Section 4.2.1) and St (Section 4.2.2), it is seen that the discontinuous jump in the data at the onset of the co-shedding regime is seen only for the St data (this jump itself is much weaker than what is observed for infinite cylinders), at P/D = 4.0, 3.5, 3.0, and 2.75 for AR = 9, 7, 5, and 3, respectively. The C_D data do not show any jump, and the initial suggestion in Section 4.2.1 was that the absence of the jump could be due to a delayed switchover to the co-shedding regime at higher P/D (beyond the range of the present study). The St data, however, suggest that the switch to a co-shedding regime indeed occurs, but is sensitive to AR, is more gradual rather than discontinuous (compared to two infinite cylinders in tandem), and that the difference in St across the boundary between the two flow regimes is much smaller (compared to two infinite cylinders in tandem). The reason the C_D data do not show any sudden jump may be attributed to the variation of the flow field along the cylinder heights, hence the changes in C_D with P/D are more gradual.

4.3 Side-by-Side Finite-Height Cylinders

Much like the tandem configuration discussed in Section 4.2, the flow around two infinite cylinders arranged in a side-by-side configuration has been extensively documented in the literature. Though geometrically symmetric, the flow field, wind loading, and vortex shedding associated with each cylinder may be significantly different. The degree of asymmetry between the two cylinders is proportional to the proximity interference, thus a smaller P/D results in a larger difference in flow characteristics.

Three main flow regimes are associated with infinite side-by-side cylinders: base bleed, biased, and co-shedding. The base bleed flow regime ($P/D < 1.25$) is characterized by single-body behaviour where both cylinders are associated with a single Kármán vortex street. The small portion of the flow that passes through the gap into the base region (the base bleed flow) may bias strongly to one cylinder, causing a strong attractive lift force (negative values of C_L). The biased flow regime ($P/D = 1.25 – 2.5$) is characterized by vortex shedding from both cylinders, with the gap flow becoming biased to one side. The result is a narrow near wake behind one cylinder and a wide near wake behind the other cylinder. The co-shedding regime ($P/D > 2.5$) is characterized by two parallel Kármán vortex streets produced by the cylinders, with proximity effects causing the vortex streets to synchronize either anti-phase or in-phase.

This section contains the results for two surface-mounted finite-height cylinders in a side-by-side configuration, including the mean drag coefficient, C_D (Section 4.3.1), mean lift coefficient, C_L (Section 4.3.2), and Strouhal number, St (Section 4.3.3) as functions of P/D. Additionally the quasi-stable gap flow bias found at very small P/D, which is associated with hysteretic behaviour for incidence angles close to 90° (when the cylinders are nearly side-by-side), is also discussed (Section 4.3.4).

4.3.1 Mean Drag Coefficient

Mean drag coefficient data for the two side-by-side finite cylinders, for AR = 9, 7, 5, and 3, are found in Figure 4.4 alongside infinite cylinder data from Alam et al. (2003a). For small P/D configurations where distinct C_D values associated with two different wake states were obtained, data were acquired along test trajectories using both clockwise (CW) and counter-clockwise (CCW) increments in α. Varying the direction that α was incremented up to $\alpha = 90°$ allowed the instrumented central cylinder to obtain both wake states each with its own unique wind loads.

In a similar fashion to infinite cylinders, finite-height cylinders in close proximity ($P/D < 1.5$) showed a large difference in C_D values between the two cylinders (found in Figure 4.4). The base bleed flow regime at $P/D = 1.125$ had the highest difference in the two C_D values, with the gap flow remaining attached to the base region of the higher C_D cylinder (based on results from Alam et al. 2003a). Reducing the AR causes a dramatic decrease in C_D. As the pitch ratio

increases from P/D = 1.125 to 1.25, there is a significant decrease in C_D for both cylinders (this is also found with infinite cylinders). This decrease in C_D represents the transition from the base bleed flow regime to the biased flow regime, as the additional gap flow significantly increases the base pressure behind the cylinders. The changes in C_D at these low pitch ratios may be due to the considerable amount of downwash produced by two closely spaced cylinders. As the two cylinders act similar to one larger body, the entire structure is represented by twice the frontal width, resulting in half the AR.

The critical value of P/D at which point the cylinders no longer exhibit dissimilar C_D, i.e., the upper P/D limit for the biased flow regime, is found to decrease as the cylinder AR is lowered. By defining the P/D boundary between the biased and co-shedding flow regimes as the point where there is no longer an abrupt change in C_D within $\alpha = 90° \pm 1°$ (to account for uncertainty in turntable position) it was found that AR had a large effect.[1] Using this criterion, the critical P/D was found to be at P/D = 2.0, 1.75, 1.5, and 1.25 for AR = 9, 7, 5, and 3, respectively (Table 4.1). This result suggests that the aspect ratio influences the gap stability, with a smaller AR unable to maintain a preferential bias side for the full 10 s sample time (particularly at smaller values of P/D). The critical P/D values for all AR were therefore found to be *lower* than the critical value of P/D = 2.5 identified for infinite cylinders (Alam et al., 2003a).

[1] Identifying the high and low values of C_D, and the end of the biased flow regime, required some analysis of the staggered cylinder data, reported later in this chapter, as the method of data acquisition may have affected the results for cylinders near the side-by-side configuration at intermediate P/D. Though only a single value of C_D was measured for both CW and CCW α at many of the moderate P/D, the staggered cylinder plots presented in Appendix B show a dissimilar value of C_D for upstream and downstream cylinders near $\alpha = 90°$ for moderately spaced cylinders (approximately P/D = 1.5 – 3.0 depending on AR). Increased gap stability found at very low P/D (= 1.125 and 1.25) can result in the gap bias remaining fixed to one cylinder for the entire length of the 10 s sample period, resulting in two distinct values of C_D at $\alpha = 90°$ when α is varied CW and CCW. On the contrary, at intermediate P/D (=1.5 – 3.0) the diminished gap stability allows for the bias to intermittently change side throughout the course of the 10 s sample period, with high and low C_D values corresponding to both wake states equally represented in the instantaneous force data. The result is an averaged value of C_D between the two wake states, with a preferential direction more likely as one cylinder is brought slightly in front of the other (small changes in α away from 90°). The aforementioned reduction in proximity effect as P/D increases also affects the ability to manually bias the flow to one side by changing α, as seen by the broader α range over which the intermittent switching is apparent as P/D is increased.

A more accurate way of determining the critical value of P/D, at the end of the biased flow regime, would be to instrument both cylinders with force balances and measure instantaneous forces simultaneously on the two cylinders. As long as the random intermittent switching is at a frequency lower than the vortex shedding frequency, discrete high and low bands of C_D representing both wake states could then be identified at alternating times for the two cylinders. In the present experiments, however, as the data collected were averaged over a 10 s period and only for one cylinder at a time, the exact behaviour of both cylinders at the same instant is unclear. In an attempt to approximate the critical P/D without the undue influence of the intermittent bias switching, data from staggered configurations of $\alpha = 85°$ and 95° were then used, where the flow remained stably biased preferentially to one cylinder for a longer portion of the 10 s sampling time. This method is described in detail in Appendix C, and allowed the critical value of P/D to be estimated as $P/D = 3.0$, 2.5, 2.0, and 1.75 for AR = 9, 7, 5, and 3, respectively (Table 4.1). Using this second method to identify the critical P/D, the biased flow regime for the finite cylinders may extend over a *wider* range of P/D compared to infinite cylinders for the case of AR = 9. The general effect of lowering the AR, however, remains unchanged, which is to lower the value of the critical P/D and thus reduce the extent of P/D where biased flow is observed. The main finding is that a sufficiently high aspect ratio is needed for the biased flow pattern to occur.

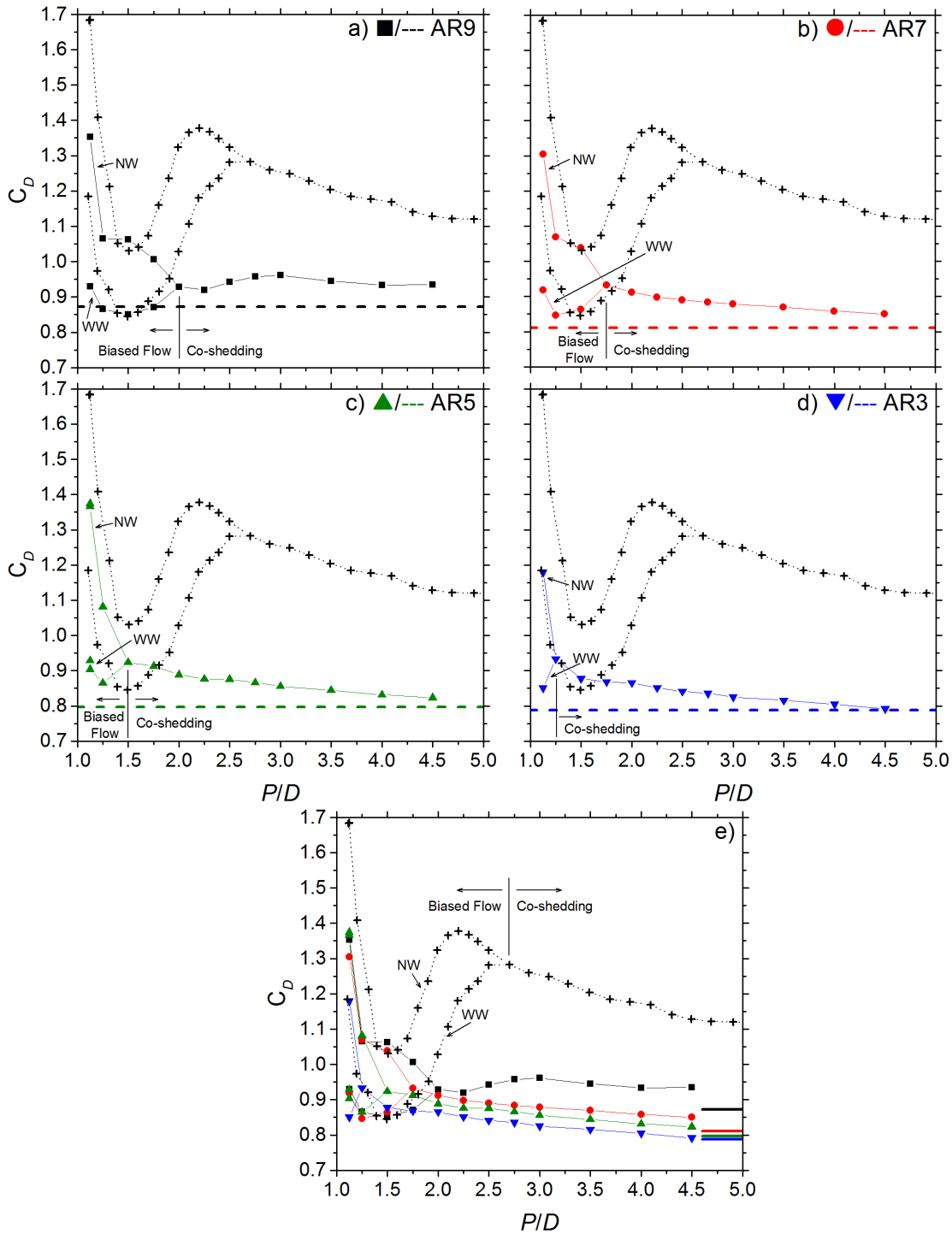

Figure 4.4: Mean drag coefficient, C_D, data for side-by-side finite-height (solid symbols), isolated finite-height (solid colour line), and infinite (+ data from Alam et al., 2003a) cylinders as function of P/D and a) AR: ■/– AR = 9, b) ●/– AR = 7, c) ▲/– AR = 5, d) ▼/– AR = 3, and e) all data combined. High C_D is narrow wake state (NW); low C_D is wide wake state (WW).

Compared to the infinite cylinder C_D data of Alam et al. (2003a) (Figure 4.4), which shows complex behaviour at intermediate P/D within the biased flow regime, the finite cylinder C_D data behave much simpler overall. The greater number of vortex systems found with finite-height cylinders may act to simplify the behaviour of the drag coefficient data compared to infinite cylinders. Though the flow field itself is vastly more complicated, a significant change in one vortex system does not have the profound effect on the entire finite cylinder flow field compared to what occurs for infinite cylinders with less complex vortex dynamics.

The C_D curves (Figure 4.4) for the finite-height cylinders trend toward that of isolated cylinders as P/D increases to the widely spaced range and the influence of proximity interference becomes less significant. As AR is decreased, the isolated cylinder's value of C_D is reached at a lower P/D in a similar fashion to that of the boundary between the biased and co-shedding flow regimes being found at a lower P/D.

4.3.2 Mean Lift Coefficient

Experimental data for C_L at AR = 9, 7, 5, and 3 may be found in Figure 4.5 along with the infinite cylinder data from Alam et al. (2003a). As described in the preceding section, both of the bi-stable wake states were attained for the instrumented central cylinder by rotating the outer cylinder in either the clockwise (CW) or counter-clockwise (CCW) direction when approaching $\alpha = 90°$. For intermediate P/D where intermittent bias switching prevented the two distinct wake states from being easily identified, data from staggered configurations of $\alpha = 85°$ and 95° (see Appendix C) were used to determine the preferential bias of the gap flow.

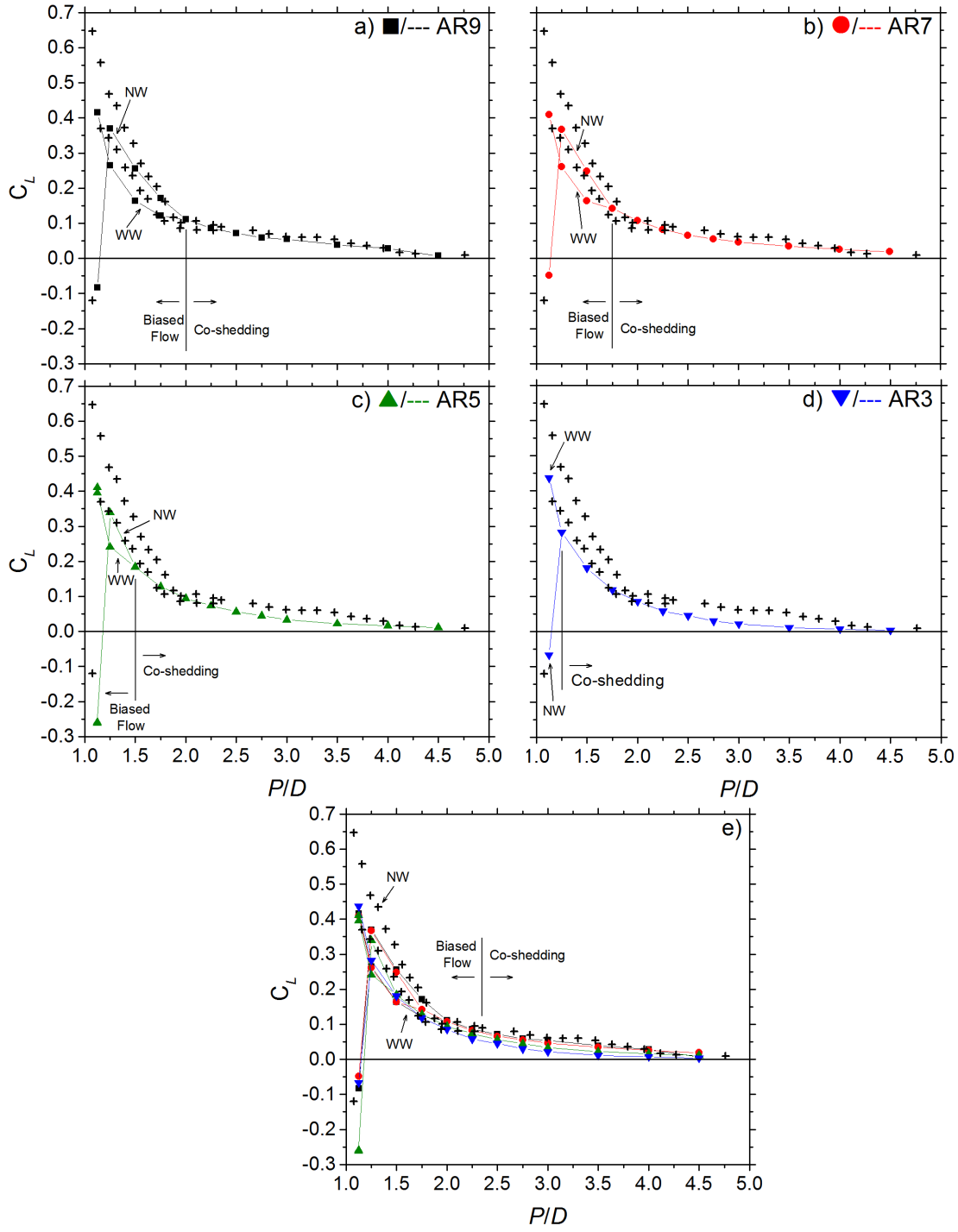

Figure 4.5: Mean lift coefficient, C_L, data for side-by-side finite-height (solid symbols), isolated finite-height (solid colour line), and infinite (+ data from Alam et al., 2003a) cylinders as function of P/D and AR: a) ■/– AR = 9, b) ●/– AR = 7, c) ▲/– AR = 5, d) ▼/– AR = 3, and e) all data combined. For $P/D \geq 1.25$, high C_L is narrow wake state (NW); low C_L is wide wake state (WW).

The base bleed regime at $P/D = 1.125$ is very apparent in the C_L data presented in Figure 4.5. Two very different C_L values are obtained, with the biased side cylinder experiencing an attractive (negative) C_L. The limited number of P/D points for very closely spaced cylinders only allowed for one data point to be measured within this unique flow regime characterized by severe gap (base bleed) flow deflection. With the exception of AR = 5, a lower AR tended to reduce the difference between the two C_L values.

For $P/D > 1.125$, a repulsive (positive) C_L was measured for both cylinders. As P/D increases and the gap flow becomes parallel to the freestream, the difference in C_L between the two cylinders becomes smaller. As the magnitude and range of C_L is much smaller than C_D, the intermittent gap bias direction switching found at intermediate P/D is more difficult to identify in the C_L data gathered at α near 90°. Thus, it is difficult to define the upper P/D boundary between the biased and co-shedding flow regimes using C_L data alone.

For $P/D > 2.5$, where the co-shedding flow regime would be encountered, the finite cylinders (for all AR) behave similarly to the infinite cylinders, with very small magnitudes of C_L (each cylinder experiences the same small repulsive lift force). For this flow regime, AR seems to only have a small effect, with a decrease in AR corresponding to a small decrease in C_L. The data for all AR trend toward zero mean lift coefficient as P/D approaches 4.5, as the reduced proximity effects cause both cylinders to behave as if they were isolated.

Within the biased flow regime, it was noticed that the cylinder experiencing the high C_L also experiences a high C_D and a high St, while the cylinder experiencing the low C_L also experiences a low C_D and a low St. This result is consistent with the infinite cylinder data for staggered cylinders reported by Sumner et al. (2005), however it is different than what was reported by Alam et al. (2003a); this discrepancy is explored in detail in Appendix D.

4.3.3 Strouhal Number

Strouhal number, St, measurements were conducted in a similar manner as described in the tandem cylinder section (Section 4.2.2). Two hot-wire probes were used, one in the wake of each cylinder, and each located at the cylinders' mid-height positions. The St data for the two cylinders are presented in Figure 4.6. Due to intermittent gap bias switching found at moderate P/D (the biased flow regime) and the extended sampling time compared to acquiring force balance data, the power spectra typically showed multiple peaks, although they tended to be less well defined. It was often found that both probes would capture the same two peaks, corresponding to both wake states that would switch back and forth several times throughout the measurement period. Consequently, data in Figure 4.6 represent data selected between α = 87° and 90° that show both values of St captured by both probes before an obvious gap bias change that would happen at a single α.

Single bluff body behaviour found within the base bleed flow regime is very apparent in Figure 4.6 at exclusively P/D = 1.125. Both hot-wire probes read the same value of St which was approximately half of that found with the isolated cylinder of the same AR. It follows that the two finite cylinders are functioning as one body of twice the width with a single vortex street. The AR does not have a large effect on St in the base bleed flow regime, as all of the measured St are approximately the same. However, if the greater width is taken into account the effective AR tested only covers a smaller range of AR = 4.5, 3.5, 2.5, and 1.5, which all are close to, if not below, the critical AR.

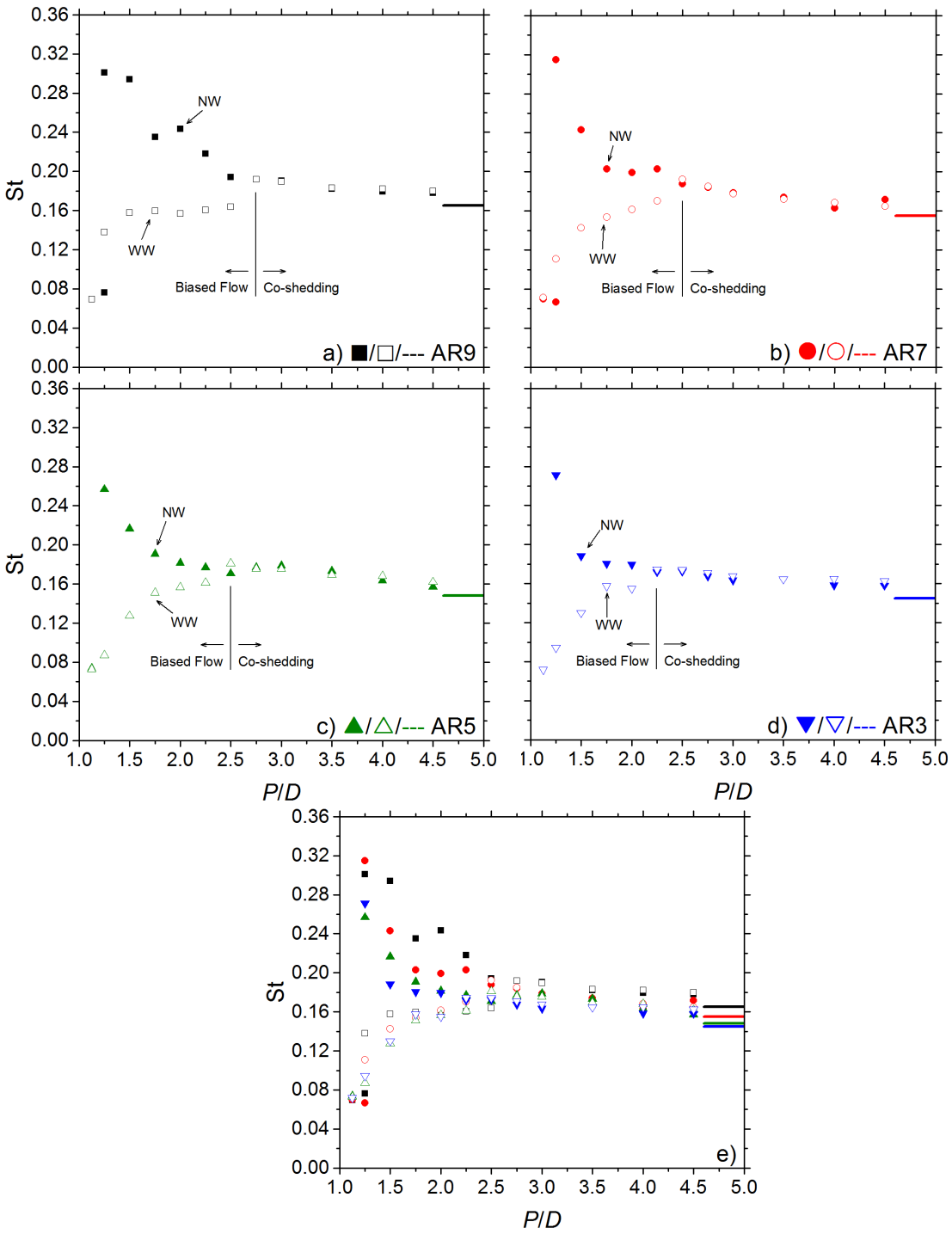

Figure 4.6: Side-by-side configuration mid-span Strouhal number, St, data as measured by the traversing hot-wire probe (solid symbols), stationary hot-wire probe (open symbols), and for an isolated cylinder (solid colour line) as function of *P*/*D* and AR: a) ■/□/– AR = 9, b) ●/○/– AR = 7, c) ▲/△/– AR = 5, d) ▼/▽/– AR = 3, and e) all data combined. High St is narrow wake state (NW); low St is wide wake state (WW).

Intermediate P/D show the biased flow regime quite clearly in Figure 4.6. For all AR, the transition from the base bleed regime to the biased flow regime occurs between P/D = 1.125 and 1.25. Within this range, smaller values of P/D produce a stronger gap deflection and a larger difference between the near wakes of the two cylinders. As described in Alam et al. (2003a), the side to which the gap flow is biased experiences a narrower near wake with a higher vortex shedding frequency, while the opposing side experiences wider near wake with a lower vortex shedding frequency. Within this flow regime a smaller value of P/D is associated with greater interference, resulting in a larger difference in wake width and ultimately the measured value of St between the two cylinders. As seen in Figure 4.6, the largest difference in St occurs at P/D = 1.25, with the two St values rapidly approaching each other as P/D is increased. The cylinder with the wide near wake (opposite to the direction of the biased gap flow) does not experience much change in St as either P/D or AR is varied, remaining at or just below the value of its respective isolated finite cylinder throughout the biased flow regime. The cylinder with the narrow near wake (to which the gap flow is biased) experiences a steep, non-linear decrease in St with increasing P/D that asymptotically approaches the value of the other cylinder. The AR has a large influence on St within the biased flow regime, where a lower AR causes the two distinct values of St to more quickly approach one another as P/D is increased.

The P/D boundary between the biased flow and co-shedding regimes was previously defined as the point where an appreciable change in C_D (approximately 5 %) was seen. Velocity spectra were measured for both cylinders simultaneously, thus the intermittent gap switching was easier to identify as the spectra would show a peak for each wake state. As P/D increases, St for both wake states asymptotically approach each other and the intermittent switching becomes less noticeable, the spectra show one wider peak as opposed to two. The spectra for AR = 9 and 3 may be found in Figure 4.7. Using the St based criterion described above, the onset of the co-shedding regime occurs at P/D = 2.75, 2.5, 2.5, and 2.25 for AR = 9, 7, 5, and 3, respectively. When compared to the boundaries defined by C_D in Table 4.1, the St criterion provides boundaries much larger than the C_D criterion, though their dependency on AR is similar.

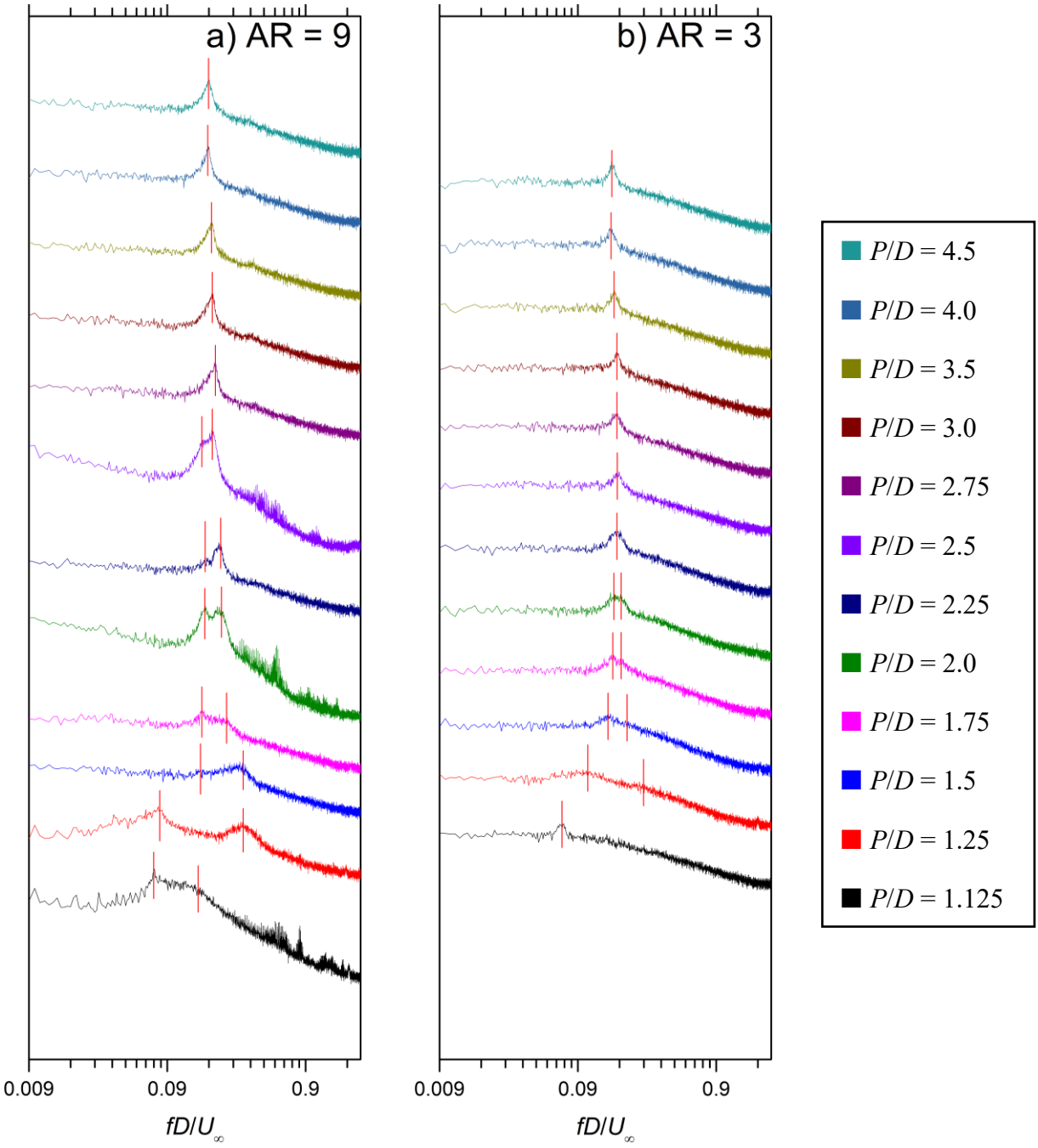

Figure 4.7: Power spectra of velocity fluctuations behind the outer cylinder in the side-by-side configuration for a) AR = 9 and b) AR = 3. The vortex shedding peaks (Strouhal numbers) are marked by red lines.

Similar to the discussion above on classifying co-shedding with C_D, a similar methodology was used with St by preferentially biasing the intermittent gap flow using staggered configurations of α = 85° and 95° (Figure C.3 in Appendix C). The flow regime boundary is then defined as the P/D value where there is no longer an appreciable difference between individual cylinder St values and both cylinders assume the same value; the boundary is still dependent on AR. Using the St based criterion described above, the onset of the co-shedding regime occurs at P/D = 3.0, 2.75, 2.5, and 2.25 for AR = 9, 7, 5, and 3, respectively. When compared to the boundaries in Table 4.1 the results are very similar to the St criterion at α = 90°, likely due to the presence of two distinct spectra peaks limiting the effect of averaging.

Table 4.1: Upper P/D limit of the biased flow regime for side-by-side finite-height cylinders using appreciable variance in individual cylinder data criterion. *Infinite cylinder data taken from Alam et al. (2003a).

AR	C_D Criterion	α = 90° ± 5° C_D Criterion	St Criterion	α = 90° ± 5° St Criterion
Infinite	2.50	---	---	---
9	2.00	3.00	2.75	3.00
7	1.75	2.50	2.50	2.75
5	1.50	2.00	2.50	2.50
3	1.25	1.75	2.25	2.25

At large P/D both cylinders have vortex streets, with the only proximity interference being synchronization of vortex shedding. The anti-phase or in-phase nature of the vortex shedding could not be experimentally determined from the time-averaged data collected, however, as seen in Figure 4.6, both cylinders would share identical values of St approaching the value of their respective AR isolated cylinder as P/D was increased. This is indicative of an absence of biased flow. The AR does has a small effect on the Strouhal number for widely spaced side-by-side cylinders, with a lower St corresponding to a lower AR. The rate at which St approaches the isolated cylinder value as P/D increases does not seem to be AR dependent, with all AR tested being similarly close to the isolated values at P/D = 4.5.

4.3.4 Hysteresis at α near 90°

Hysteresis was identified at low P/D for staggered configurations near $\alpha = 90°$ where C_L and C_D measured at the central cylinder were different depending whether α was incremented clockwise (CW, α increasing) or counter clockwise (CCW, α decreasing). Many characteristics of the hysteresis are dependent on both AR and P/D. Though not within the scope of this thesis, it is likely that Re and δ/D would also have an influence on the hysteresis.

At the point of geometric symmetry (the side-by-side configuration, $\alpha = 90°$), the cylinders may experience asymmetric near wakes and subsequently different wind loads, as discussed in Section 4.3. For all four aspect ratios tested, $P/D = 1.125$ corresponds to the base bleed flow regime with severe gap flow deflection: the cylinder to which the flow is deflected experiences a very high C_D and an attractive C_L, while the non-biased cylinder experiences a lower C_D and a strongly repulsive C_L. Increasing the spacing to $P/D \geq 1.25$ results in the biased flow regime with a gap deflection angle inversely proportional to P/D. The biased flow regime is characterized by one cylinder (towards which the gap flow is deflected) having a narrow near wake with a higher C_D, C_L, and St, while the other cylinder (away from the deflected gap flow) has a wider near wake with a lower C_D, C_L, and St. In a similar manner, closely spaced cylinders in a *staggered* configuration near $\alpha = 90°$ exhibit a gap bias with the upstream cylinder assuming the narrow wake state and the downstream cylinder assuming the wide wake state.

Measurements of C_D and C_L were made from $\alpha = 0°$ to 180° in increments of 1°, which represents a CW rotation, where the central cylinder switches from a downstream cylinder (wide wake state) to an upstream cylinder (narrow wake state) at the point of symmetry, $\alpha = 90°$. Conversely, C_D and C_L data were also acquired in reverse order from $\alpha = 180°$ to 0° in increments of 1°, representing a CCW rotation, where the central cylinder starts as an upstream cylinder (narrow wake state) and ends as a downstream cylinder (wide wake state) as it passes $\alpha = 90°$.

The hysteresis occurs as the outer cylinder moves past $\alpha = 90°$ but maintains its initial wake state, causing the $C_D(\alpha)$ and $C_L(\alpha)$ curves to depart from their CW or CCW counterpart. Only once the outer cylinder has rotated to a sufficiently high (or low) critical value of α past 90° (which is a complex function of AR and P/D) does the gap flow bias change orientation and the central cylinder assumes the opposite wake state. The critical α, where the wake state changes, is

marked by an abrupt change in both C_D and C_L that jump back to the value measured at the same α for the opposite direction of rotation, at which point the CW and CCW collected C_D and C_L data are identical for all α away from 90°. For a summary of the hysteretic behaviour as a function of both P/D and AR, see Table 4.2, and for a simplified sketch of the shear layer behaviour, see Figure 4.8.

Table 4.2: Summary of hysteretic behaviour as a function of P/D and AR for staggered cylinders near the side-by-side configuration.

P/D	**AR = 3**	**AR = 5**	**AR = 7**	**AR = 9**
1.125	Strong Hysteresis: "less stable", inconsistent upper and lower limits on critical values of α	Strong Hysteresis: inconsistent upper and lower limits on critical values of α	Strong Hysteresis: very consistent upper and lower limits on critical values of α	Strong Hysteresis: very consistent upper and lower limits on critical values of α
1.25	No Hysteresis	No Hysteresis: discontinuous change at $\alpha = 90°$	Weak Hysteresis: very consistent upper and lower limits on critical values of α	Moderate Hysteresis: very consistent upper and lower limits on critical values of α
1.5	No Hysteresis	No Hysteresis	No Hysteresis: discontinuous change at $\alpha = 90°$	Weak Hysteresis: very consistent upper and lower limits on critical values of α
1.75	No Hysteresis	No Hysteresis	No Hysteresis	No Hysteresis: discontinuous change at $\alpha = 90°$
2.0	No Hysteresis	No Hysteresis	No Hysteresis	No Hysteresis

Table 4.3: Range of incidence angle (α) over which hysteresis is experienced in the wind loading on the cylinders. Values in parentheses show upper and lower critical α. The * denotes configurations that did not experience a hysteretic α range centered (symmetric) about $\alpha = 90°$.

	AR = 3	**AR = 5**	**AR = 7**	**AR = 9**
***P/D* = 1.125**	23° * (70° - 93°)	47°-56° * (53° - 109°)	24° (77° - 101°)	23° (77° - 100°)
***P/D* = 1.25**	No Hysteresis	0° (90°)	5° (92° - 88°)	10° (85° - 95°)
***P/D* = 1.5**	No Hysteresis	No Hysteresis	0° (90°)	2° (89° - 91°)
***P/D* = 1.75**	No Hysteresis	No Hysteresis	No Hysteresis	0° (90°)
***P/D* = 2.0**	No Hysteresis	No Hysteresis	No Hysteresis	No Hysteresis

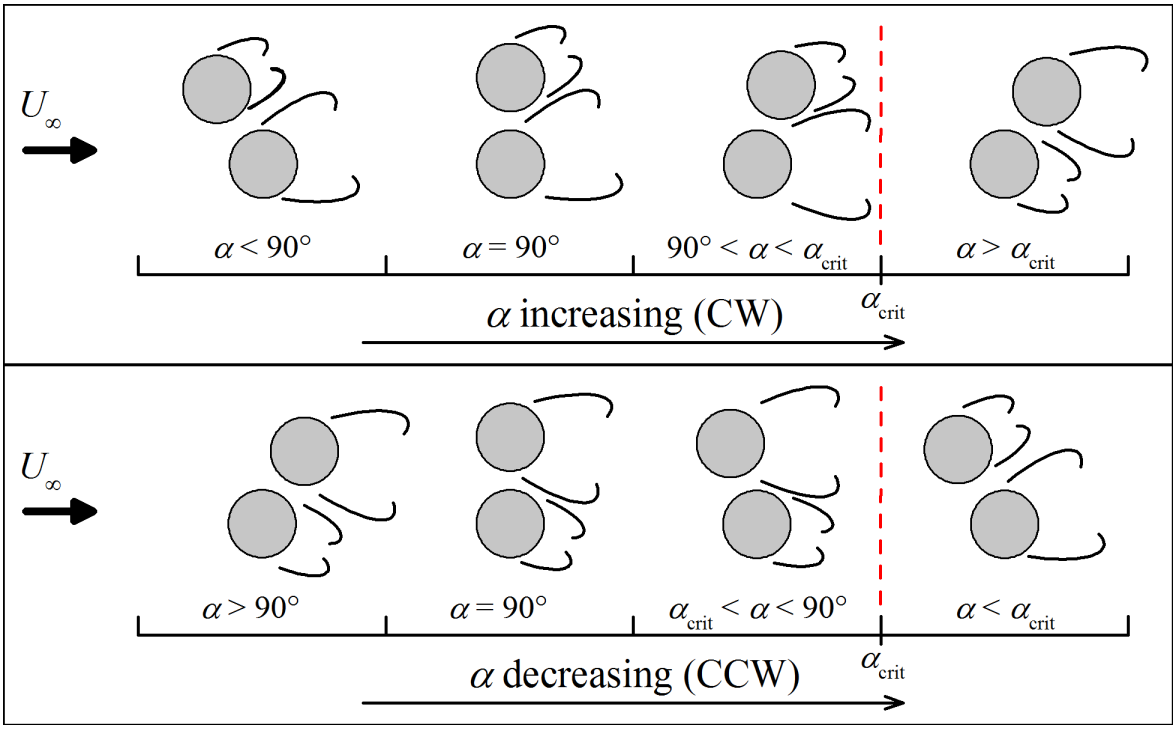

Figure 4.8: Simplified sketch of shear layer behaviour during hysteresis near $\alpha = 90°$ in a two-dimensional plane

Figure 4.9 shows the behaviour of C_L and C_D with α for AR = 9 (Figure 4.9a) and AR = 3 (Figure 4.9b) at several P/D. For similar plots depicting AR = 7 and 5, see Appendix E. It can be seen that lowering P/D increases both the angular range where hysteresis is found as well as the difference in the magnitude of C_L and C_D between wide and narrow wake states. For a full list of the angular ranges with hysteresis present as a function of both P/D and AR see Table 4.3. For configurations that experience hysteresis ($P/D \leq 1.5$ for AR = 9, $P/D \leq 1.25$ for AR = 7, and only $P/D = 1.125$ for AR = 5 and 3) there is a distinct difference in wind loading between $P/D = 1.125$ (the base bleed flow regime) and $P/D \geq 1.25$ (the biased flow regime).

For $P/D \geq 1.25$ the cylinders fall within the biased flow regime, however as AR is reduced the P/D range where the gap bias behaviour is found also reduces. When the central cylinder is initially in the downstream position (wide wake state, CW rotation with α increasing from $\alpha < 90°$), C_D for the central (downstream cylinder) is relatively low and C_L is less repulsive relative to the narrow wake state. Conversely, when the central cylinder is initially in the upstream position (narrow wake state, CCW rotation with α decreasing from $\alpha > 90°$) both C_D and C_L for the central (upstream) cylinder are higher than found in the opposing wake state. This pairing of higher coefficients with the narrow wake state and lower coefficients with the wide wake state is also found in the infinite cylinder data of Sumner et al. (2005). The initial wake state developed at the central cylinder before α reaches 90° is maintained past 90°. A smaller P/D results in an extended region of α before the central cylinder abruptly switches to the other wake state.

At $P/D = 1.75$ for AR = 9, $P/D = 1.5$ for AR = 7, and $P/D = 1.25$ for AR = 5 (as seen in Table 4.2) no hysteresis occurs, however the biased flow regime persists with the central cylinder intermittently switching between wake states at $\alpha = 90°$. At higher P/D than these values, there is no longer an abrupt jump in C_D or C_L at or near $\alpha = 90°$, and any intermittent gap bias switching is no longer discernable without instantaneous measurements, as described in Appendix C.

For $P/D = 1.125$ the measured wind loads resemble those of base bleed flow regimes, and the initially upstream cylinder behaves significantly different to cylinders in the biased flow regime. When the central cylinder is initially downstream (non-biased side, CW rotation with α increasing from $\alpha < 90°$) it behaves similar to larger P/D, with a lower C_D relative to the other wake state and a largely repulsive C_L. Conversely, the cylinder that was initially upstream

(biased side, CCW rotation with α decreasing from $\alpha > 90°$) experiences significantly higher C_D and an attractive C_L, unlike any larger P/D. These alternating high and low coefficients with narrow and wide wake states match well with the infinite cylinder results of Alam and Zhou (2007) and Alam et al. (2003a). Only $P/D = 1.125$ results in either of the cylinders experiencing an attractive C_L, which becomes more significant in magnitude the farther the outer cylinder moves past $\alpha = 90°$ in the hysteretic range, as the base bleed flow is further deflected. As the proximity interference is strongest with $P/D = 1.125$, the abrupt jump in C_D and C_L is largest in magnitude, with the directions of the lift force also changing direction. It is also noted that $P/D = 1.125$ was the only cylinder spacing that produced hysteresis for all aspect ratios, indicating that the base bleed dynamics may have a stronger influence than aspect ratio effects for this pitch ratio.

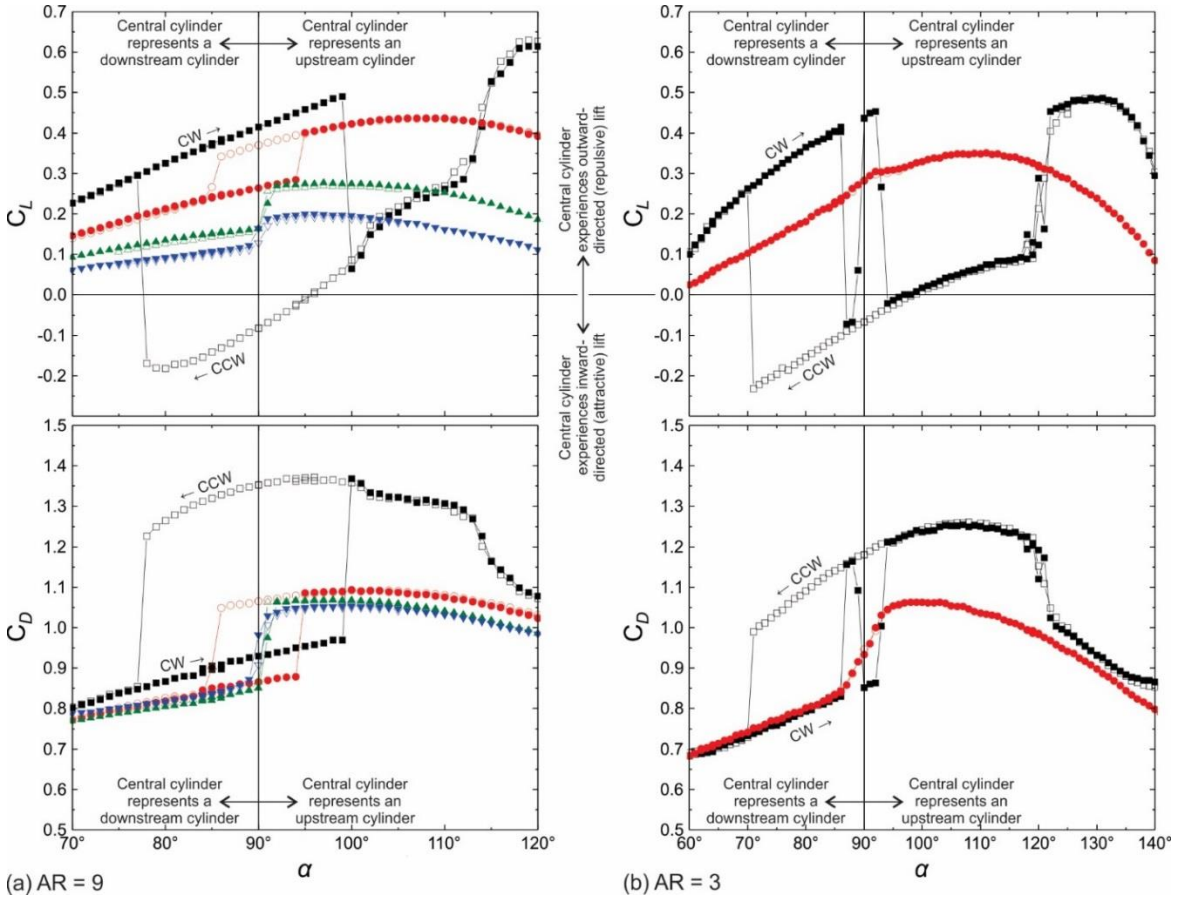

Figure 4.9: C_D and C_L data for the central cylinder for a) AR = 9 and b) AR = 3. Solid symbols: CW movement of the outer cylinder. Open symbols: CCW movement of the outer cylinder. ■, □: $P/D = 1.125$; ●,○: $P/D = 1.25$; ▲,△: $P/D = 1.5$; ▼,▽: $P/D = 1.75$.

Figure 4.10 shows the behaviour of C_D and C_L as a function of α and AR for P/D = 1.125 (Figure 4.10a) and P/D = 1.25 (Figure 4.10b) for all four aspect ratios. All four aspect ratios experience hysteresis at P/D = 1.125, however AR effects have a strong influence over whether or not a given P/D in the biased flow regime ($P/D \geq 1.25$) will experience hysteresis, as detailed in Table 4.2.

Hysteresis is present for all aspect ratios at P/D = 1.125, however the behaviour of each AR at P/D = 1.125 is markedly different. Consistency (or repeatability) in the upper and lower limits of α (the critical values of α) for the range of hysteresis, between different tests, lessens as AR decreases (Table 4.3), such that for smaller aspect ratios there is a greater potential for a broader range of α associated with hysteresis. The upper and lower bounds of incidence angle for the occurrence of hysteresis were highly repeatable for AR = 9 and AR = 7 for both CW and CCW rotations, however the cylinders of AR = 5 and AR = 3 did not have consistent (repeatable) α limits between tests nor in the CW and CCW directions. For AR = 5, the CW range of α for hysteretic behaviour in the wind loading varied up to 10° between tests and differed from the CCW limit by ~30°. For AR = 3, the CW data showed some intermittent switching between the two states between α = 86° and 89°, and therefore the hysteresis was considered “less stable”. Additionally, AR = 5 experienced an additional wake state, with a discontinuity at α = 95° when the tests were conducted CCW. At this point the base bleed flow perhaps biases toward the central cylinder, and after the discontinuity the already higher C_D and more attractive C_L increase in magnitude. This increase in magnitude gives AR = 5 the most extreme values of C_D and C_L out of all of the AR tested. Moreover, AR = 5 showed the largest hysteretic range with the unique wake state persisting until α = 53° (37° past the point of symmetry). Flow visualization would be beneficial for all tests conducted at P/D = 1.125 to more conclusively determine the base bleed dynamics for both cylinders simultaneously.

Cylinders in the biased flow regime ($P/D \geq 1.25$) are less complex than the base bleed flow regime (P/D = 1.25). At a given P/D, lowering the aspect ratio reduces the range of α where hysteresis occurs: at P/D = 1.25, only the cylinders of AR = 9 and 7 experience hysteresis; at P/D = 1.5, only the cylinders of AR = 9 experience hysteresis (Table 4.2). For P/D = 1.25, the cylinders of AR = 9 have a hysteretic range of 10° (between α = 85° and 95°), the cylinders of AR = 7 have a range of 5° (between α = 88° and 93°), and the cylinders of AR = 5 only

experience a discontinuous change at α = 90°. The cylinders of AR = 3 do not experience any discontinuity, rather only a gradual change between the two wake states across a wide band near α = 90°; this distinct behaviour for AR = 3 can be attributed to these cylinders being below the critical AR.

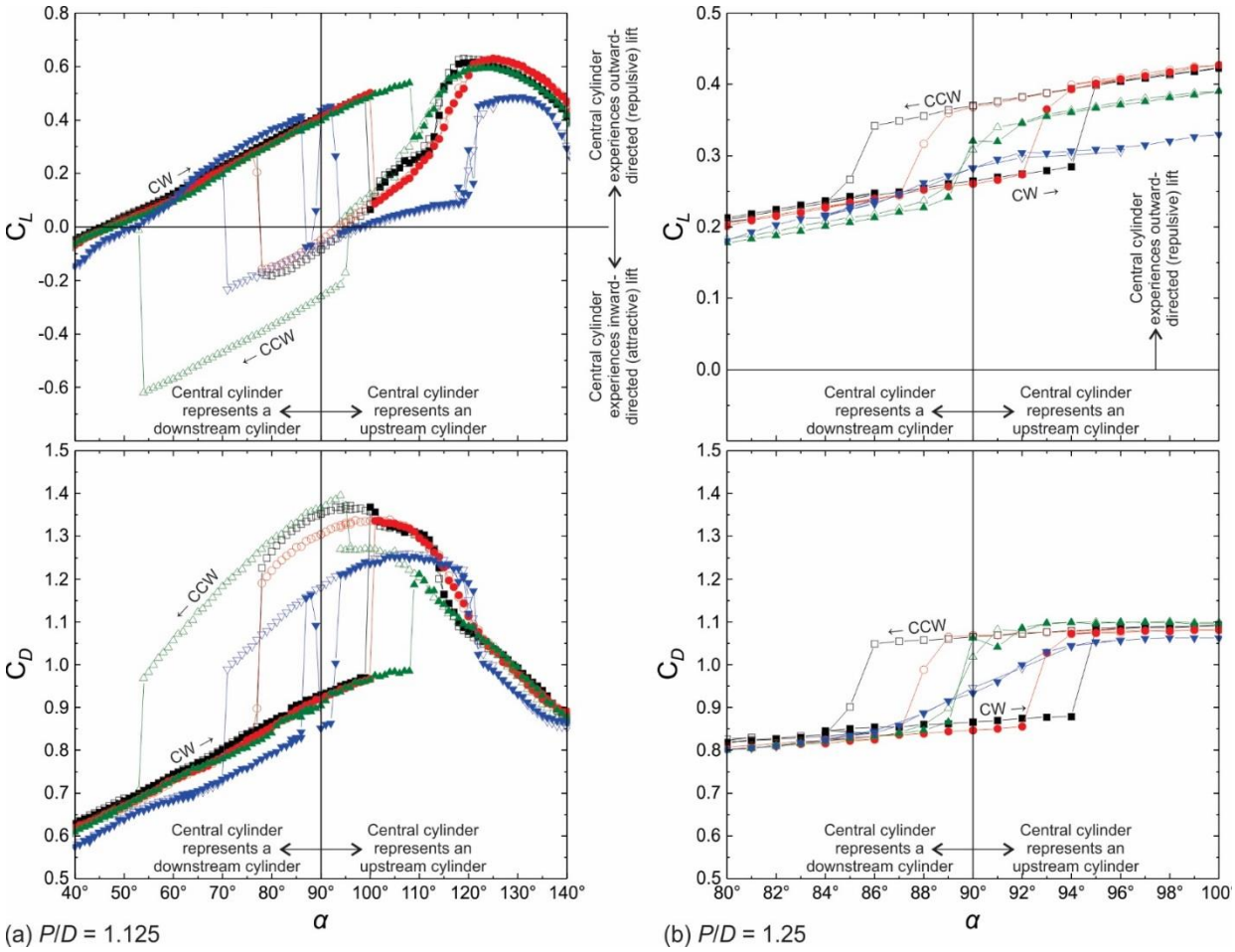

Figure 4.10: C_D and C_L data for the central cylinder, for (a) P/D = 1.125 and (b) P/D = 1.25. Solid symbols: CW movement of the outer cylinder. Open symbols: CCW movement of the outer cylinder. ■, □: AR = 9; ●,○: AR = 7; ▲,△: AR = 5; ▼,▽: AR = 3.

It is noted that data were acquired by rotating the outer cylinder to the desired α, measuring the forces for 10 s, then incrementing α again. The turntable and the outer cylinder rotate at an angular speed of 6°/s. The starting and stopping of the motion is sudden, but the resulting steady speed of rotation is still small. The tangential velocity (in m/s) of the outer cylinder depends on the pitch ratio, but in all cases (Table 4.4) it is very small compared to the freestream velocity, and sufficiently small that the flow can be assumed to remain quasi-steady. At the highest pitch ratio where hysteresis is experienced (P/D = 1.5 for AR = 9), the tangential speed of the outer (rotating) cylinder is only 0.01 % of the freestream velocity.

Table 4.4: Experimental apparatus outer cylinder and turntable motion characteristics.

P/D	1.125	1.25	1.5	1.75	2	4.5
Angular Velocity [°/s]	6.0	6.0	6.0	6.0	6.0	6.0
Tangential Velocity [m/s]	0.0037	0.0041	0.0049	0.0058	0.0066	0.0148
Tangential Velocity / U_∞[-]	0.00011	0.00012	0.00014	0.00016	0.00019	0.00042

4.4 Staggered Finite-Height Cylinders

Surface-mounted finite-height cylinders in a staggered configuration can represent a vast amount of geometries for engineering applications. Angles between tandem (α = 0°, Section 4.2) and side-by-side (α = 90°, Section 4.3) fall within the staggered range, with the combination of α and P/D mapping out complex regions of wake and/or proximity interference. Within the context of α, P/D, and AR, the behaviour of the mean drag coefficient, C_D (Section 4.4.1), mean lift coefficient, C_L (Section 4.4.2), and Strouhal Number, St (Section 4.4.3), will be discussed. Each of these sections contains several complex figures (illustrated in Figure 4.11), with contours of C_D found in Figures 4.12, 4.13, 4.14, and 4.15, characterization of the "inner lift peak" in Figure 4.16, contours of C_L found in Figures 4.17, 4.18, 4.19, and 4.20, and contours of St found in Figures 4.21 and 4.22.

Each of the contour plots (showing lines of constant C_D for example) displays data in a similar fashion, with a simplified C_D contour plot shown in Figure 4.11 as an example. The white circle in the centre of each contour plot represents a stationary cylinder for reference, with flow from left to right. The radial lines extending from the centre show values of α, and the concentric rings show values of P/D. Values plotted on each contour around the stationary reference cylinder represent the value of C_D, C_L, or St experienced by the second (outer) cylinder if it were to be positioned at that P/D and α. For example, the red "A" found on Figure 4.11 would represent the value of C_D experienced by an upstream cylinder at P/D = 2.0 and α = 75° (255° on plot). This cylinder would be in the biased flow-like regime, with a relatively higher value of C_D. Conversely, a downstream cylinder with the same P/D = 2.0 and α = 75° configuration would experience a lower value of C_D as shown by the red "B", as it is now downstream of the stationary reference cylinder. The grey cross-hatched region adjacent to the stationary reference cylinder marks the region where no measurements were conducted, as P/D < 1.0 would result in the cylinders overlapping. In the context of hysteresis (as discussed in Section 4.3.4) each contour represents the outer cylinder rotating clockwise around the stationary reference cylinder (α increasing from 0° to 360°). The result is the outer cylinder moving from upstream to downstream (left to right) on the upper portion of the contour plot, and the outer cylinder moving from downstream to upstream (right to left) on the lower portion of the contour plot.

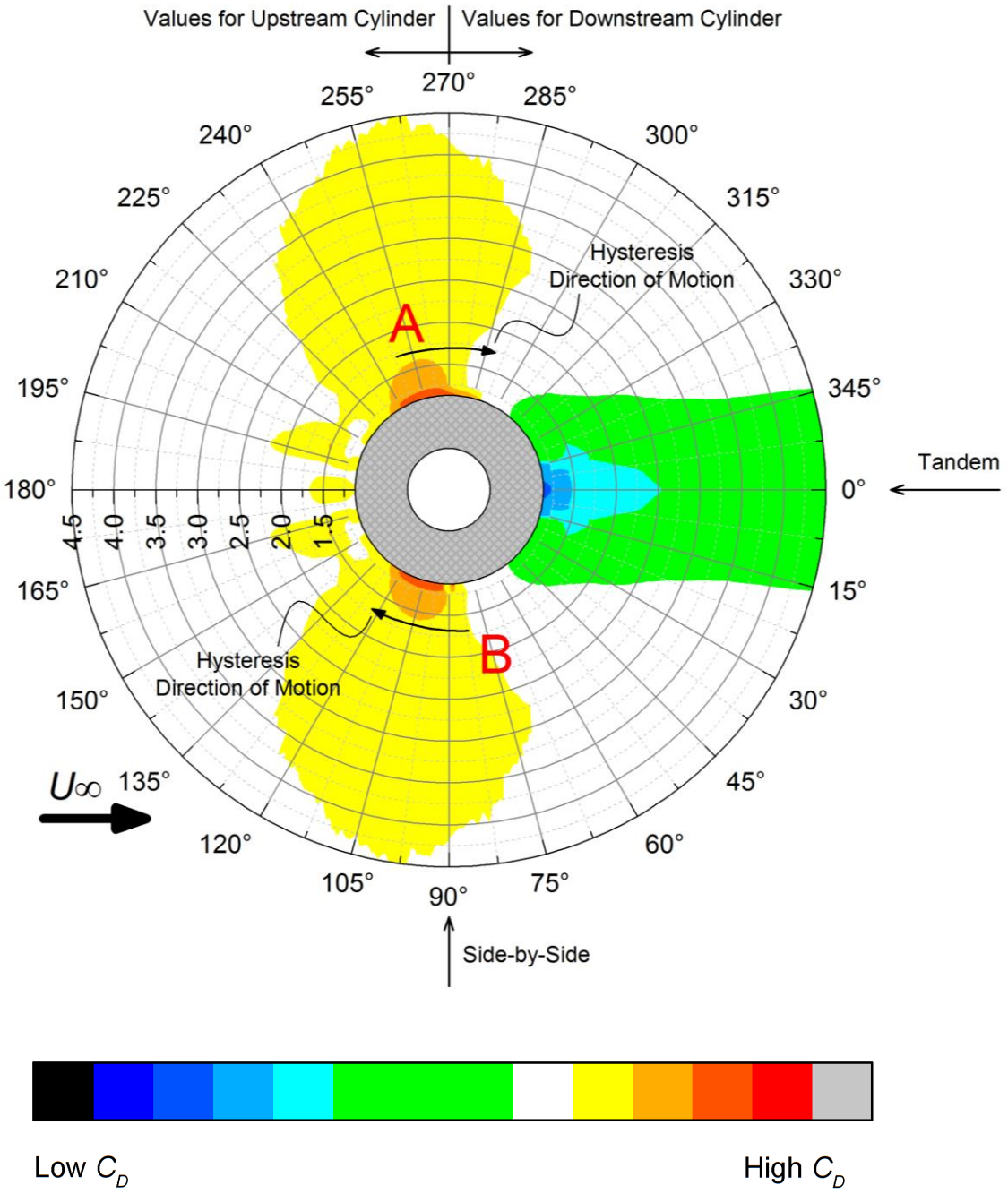

Figure 4.11: Simplified example of a C_D contour plot for illustrative purposes. A and B refer to specific staggered configurations described in the text.

4.4.1 Mean Drag Coefficient

Mean drag coefficient, C_D, contours (lines of constant C_D) for AR = 9, 7, 5, and 3 are shown in Figures 4.12, 4.13, 4.14, and 4.15, respectively. These contours represent the value of C_D that would be experienced by the outer cylinder positioned at each P/D and α relative to the central cylinder. The contours for each AR were built using the 12 discrete pitch ratios (P/D = 1.125, 1.25, 1.5, 1.75, 2.0, 2.25, 2.5, 2.75, 3.0, 3.5, 4.0, and 4.5) and incidence angles from $\alpha = -5°$ to 185° in increments of 1°. For closely spaced P/D resulting in hysteresis (described in Section 4.3.4) data were also collected by incrementing α in the opposite direction. A polar map of the data collection points for C_D and C_L may be found in Appendix A. The C_D data collected may be found separated by P/D in Appendix B.

From the contour plots, three main regions may be identified for all AR that loosely align with the regions of wake interference, proximity interference, and no interference. These regions are similar for C_L, and they are characterized by a low C_D region found at very low incidence angles (α = 0° to ~20°), a biased flow-like region found near side-by-side (α = ~45° to 90°), and a region with little interference found predominantly for the upstream cylinder at moderate to wide P/D (α = 20° to ~45°).

The low incidence angle region is mainly influenced by wake interference effects and is at the angles near tandem (α = 0° to ~20°) in Figures 4.12 though 4.15. In this region both cylinders experience complex C_D behaviour as P/D and α are varied. In the tandem configuration, a downstream cylinder experiences a thrust force for all AR at low P/D. A decrease in AR allows more high momentum fluid to enter the gap between the cylinders. This increases drag on the downstream cylinder, reduces drag on the upstream cylinder and allows a higher AR downstream cylinder to experience a thrust force at larger P/D than lower AR cylinders. For all aspect ratios, interference effects are found even up to P/D = 4.5. The upstream cylinder is significantly less affected than the downstream cylinder at large P/D, with C_D remaining fairly close to that of an isolated cylinder; however, an increase in AR results in a larger variation in C_D.

At small P/D, a local minimum value of C_D is found for the downstream cylinder at $\alpha \approx$ 11°in Figures 4.12 through 4.15. At the same α, the upstream cylinder experiences a local maximum value of C_D. These characteristics align with the descriptions given by Sumner et al. (2005) for the "inner lift peak" found with staggered infinite cylinders at similar P/D and α. Sumner et al. (2005) found that the inner lift peak transitioned to the "outer lift peak" between P/D = 2.5 and 3.0; the outer lift peak is not associated with a local minimum or maximum drag, however. The contours in Figures 4.12 through 4.15 show that the local maximum drag for the upstream cylinder extends to larger P/D than the downstream cylinder for all AR. The behaviour of the local maximum and minimum values of C_D for the cylinders varies significantly with AR, with a decrease in AR decreasing the prominence of the local max/min values at larger P/D. This result suggests that the transition from the inner lift peak to outer lift peak happens at a smaller P/D for a smaller AR; this is discussed in more detail in Section 4.4.2. Additionally, the upstream cylinder experiences significantly different behaviour in the local maximum drag for AR = 3, which may be due to it being below the critical AR, causing a substantially different shear layer and wake structure. AR = 9 and 7 show similar behaviour in this region, with AR = 5 resembling a transition between the aspect ratios above and below it (this transitional behaviour is also reported by Rostamy et al. (2012)). This dependence on aspect ratio is discussed further in Section 4.4.2.

Large incidence angles (α = ~45° - 90°) produce proximity interference effects that strengthen as P/D is reduced or AR is increased. For all AR, proximity interference effects were apparent up to P/D = 4.5. For $P/D \geq 1.75$ the biased flow regime associated with side-by-side cylinders (discussed in Section 4.3) can be seen in the C_D contours, with the upstream cylinder assuming the narrow wake state characterized by a higher C_D and the downstream cylinder assuming the wide wake state characterized by a lower C_D. At α = 90° the wake states and their corresponding C_D values switch cylinders. A higher AR increases the P/D range and the difference in C_D values between the two cylinders, while low AR tends to smooth out the behaviour across a smaller P/D and broader α range.

Very closely spaced cylinders ($P/D \leq 1.5$, though very dependent on AR) can experience hysteresis in the wind loading near $\alpha = 90°$, and this phenomenon was discussed thoroughly in Section 4.3.4. In this P/D range the difference in C_D is large between the upstream cylinder (narrow wake state, higher C_D) and downstream cylinder (wide wake state, lower C_D). Figures 4.12 through 4.15 show the value of C_D for the outer cylinder as it rotates clockwise (α increasing from 0° to 360°), representing a cylinder that is initially downstream (lower C_D) on the bottom portion of the figure ($\alpha = 0° - 90°$) and initially upstream (higher C_D) on the top portion of the figure ($\alpha = 180° - 270°$). For the case represented by the bottom portion of the contour plot, the initial lower value of C_D associated with the downstream cylinder is maintained as α increases past 90° until a critical α is reached, at which point the value of C_D reverts back the higher value expected by an upstream cylinder. The reverse is true for the upper portion of the contour plot, where the higher C_D value of the upstream cylinder is carried past $\alpha = 90°$ until a critical α, where is abruptly switches to the lower value expected by a downstream cylinder. This behaviour is a complex function of both AR and P/D and was discussed in detail in Section 4.3.4.

The regions where C_D is largely unaffected by wake or proximity interference are quite small, only spanning a range of approximately $\alpha = 20°$ to 45° for the upstream cylinder alone at large P/D. At AR = 9, 7, and 5 a small local maximum in C_D occurs at $\alpha = 30°$ and the largest P/D, which may be the appearance of an "outer lift peak" type regime. This pattern seems to develop at $P/D > 4.5$, beyond the scope of the measured data. Reducing AR has an effect of pushing this local maximum C_D to a larger P/D which may be a result of increased vortex formation length found with lower aspect ratio cylinders. Although at AR = 3 the downstream cylinder shows little indication of this local maximum C_D at $\alpha = 30°$, the peak itself may have just been pushed well beyond the largest data point at $P/D = 4.5$.

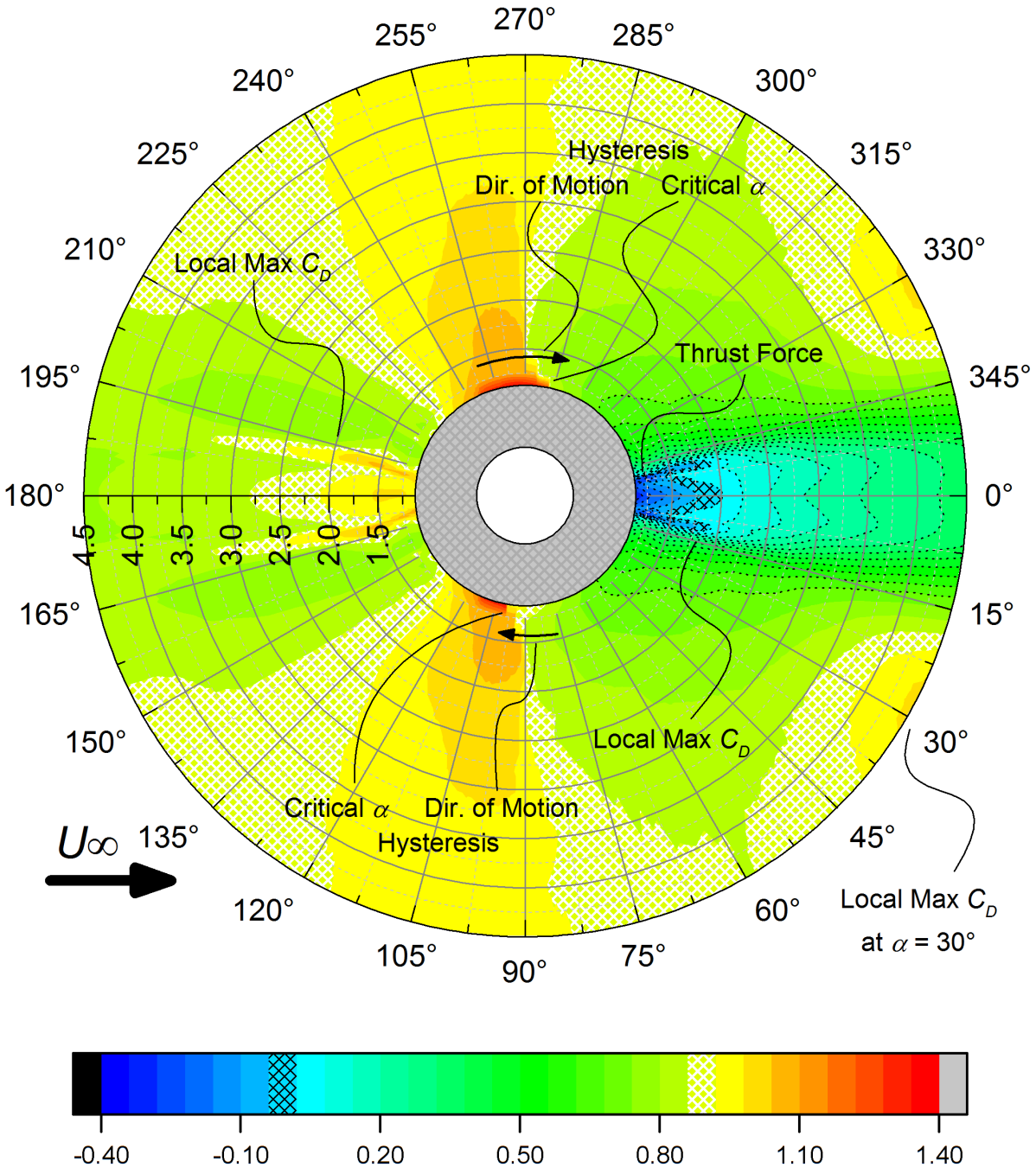

Figure 4.12: C_D contour plot for AR = 9. Contours displayed represent C_D for the outer cylinder placed at that point on the plot. In the context of hysteresis, the outer cylinder rotates clockwise around the central cylinder (α increasing from 0° to 360°). The white circle is the stationary reference cylinder, and the grey cross-hatching is the area where no data was collected. White cross-hatching is isolated cylinder value, black cross-hatching is $C_D = 0$. $P/D = 1.0$ represents the cylinders touching. Flow is from left to right.

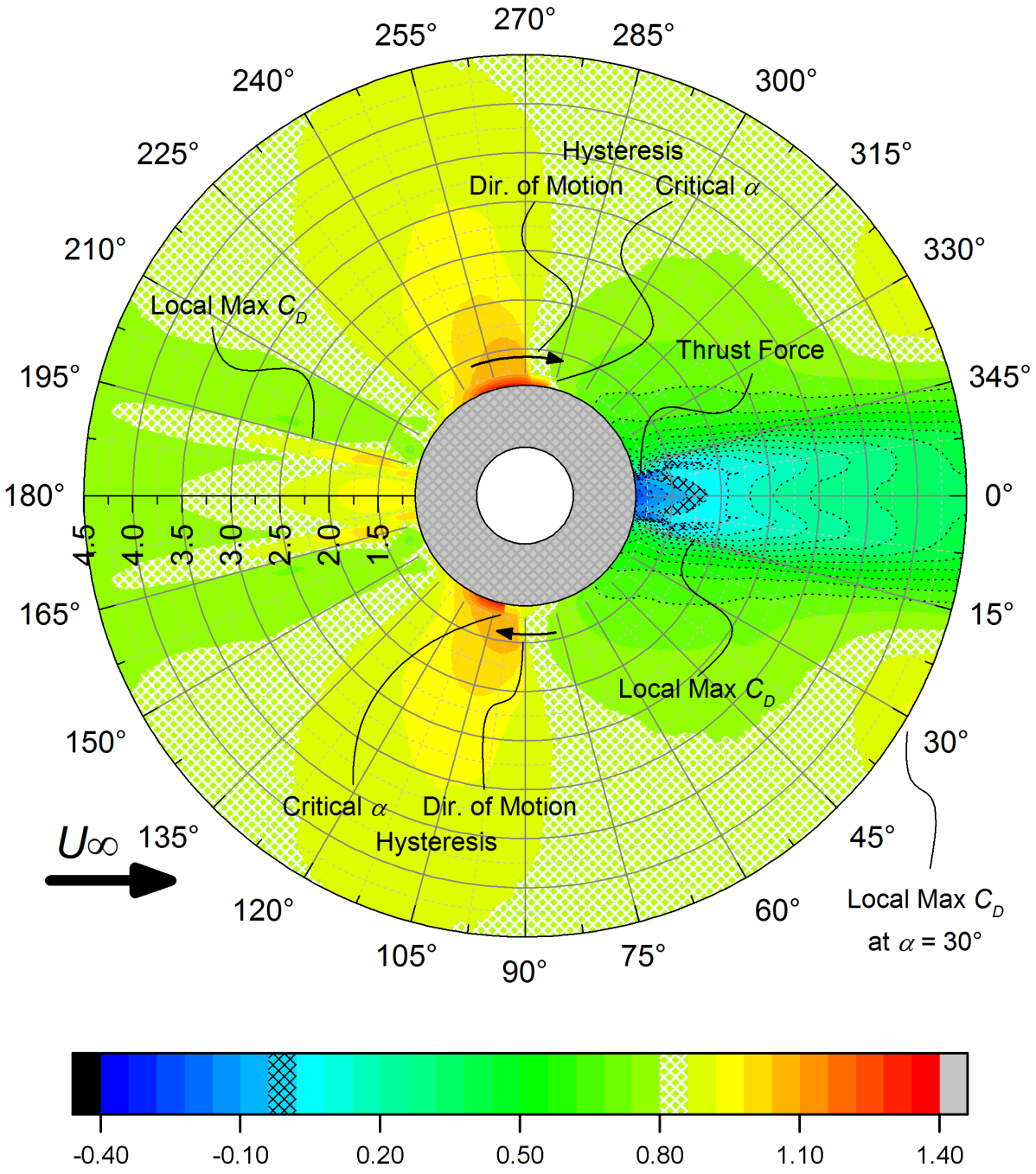

Figure 4.13: C_D contour plot for AR = 7. Contours displayed represent C_D for the outer cylinder placed at that point on the plot. In the context of hysteresis, the outer cylinder rotates clockwise around the central cylinder (α increasing from 0° to 360°). The white circle is the stationary reference cylinder, and the grey cross-hatching is the area where no data was collected. White cross-hatching is isolated cylinder value, black cross-hatching is $C_D = 0$. $P/D = 1.0$ represents the cylinders touching. Flow is from left to right.

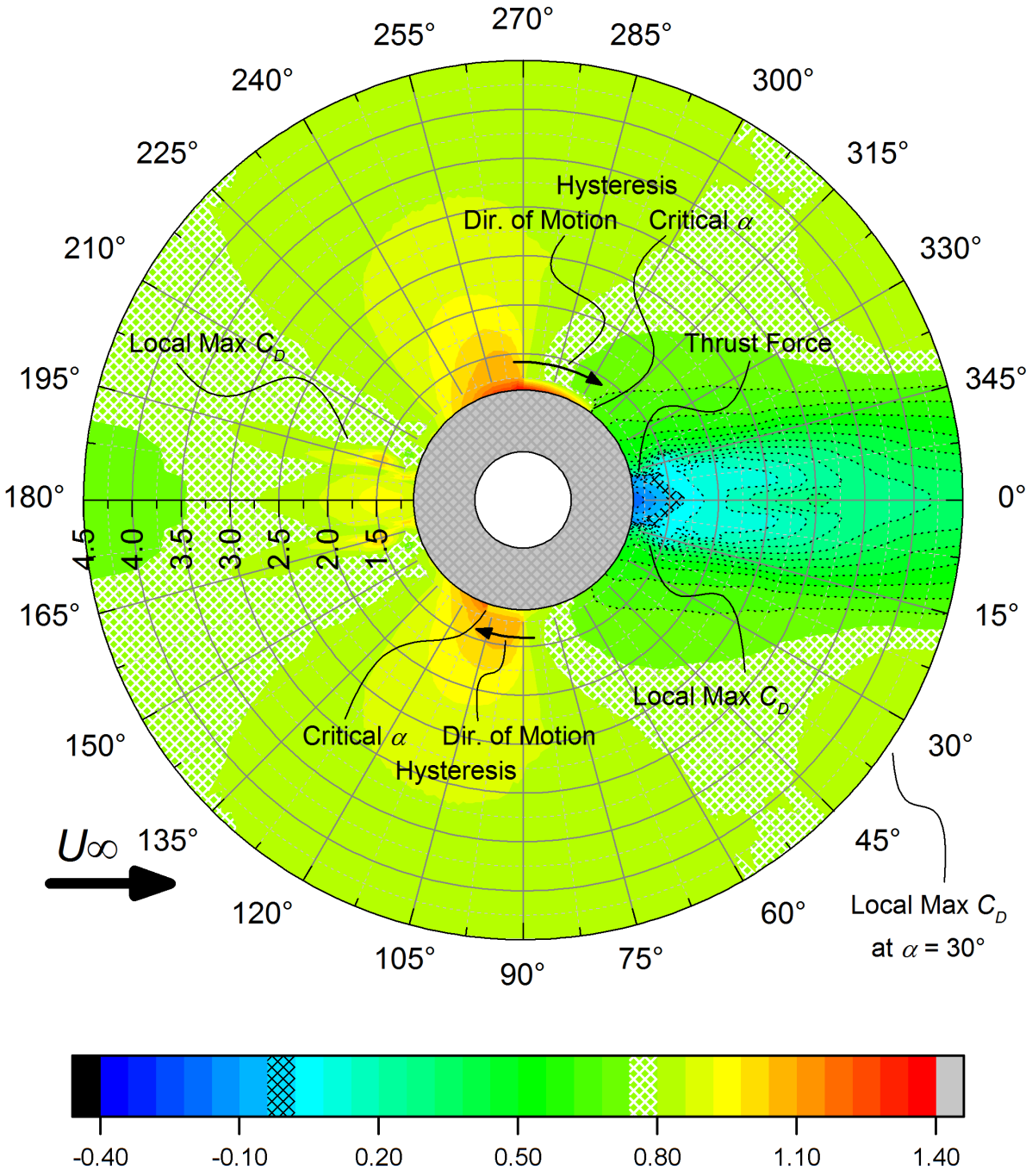

Figure 4.14: C_D contour plot for AR = 5. Contours displayed represent C_D for the outer cylinder placed at that point on the plot. In the context of hysteresis, the outer cylinder rotates clockwise around the central cylinder (α increasing from 0° to 360°). The white circle is the stationary reference cylinder, and the grey cross-hatching is the area where no data was collected. White cross-hatching is isolated cylinder value, black cross-hatching is $C_D = 0$. $P/D = 1.0$ represents the cylinders touching. Flow is from left to right.

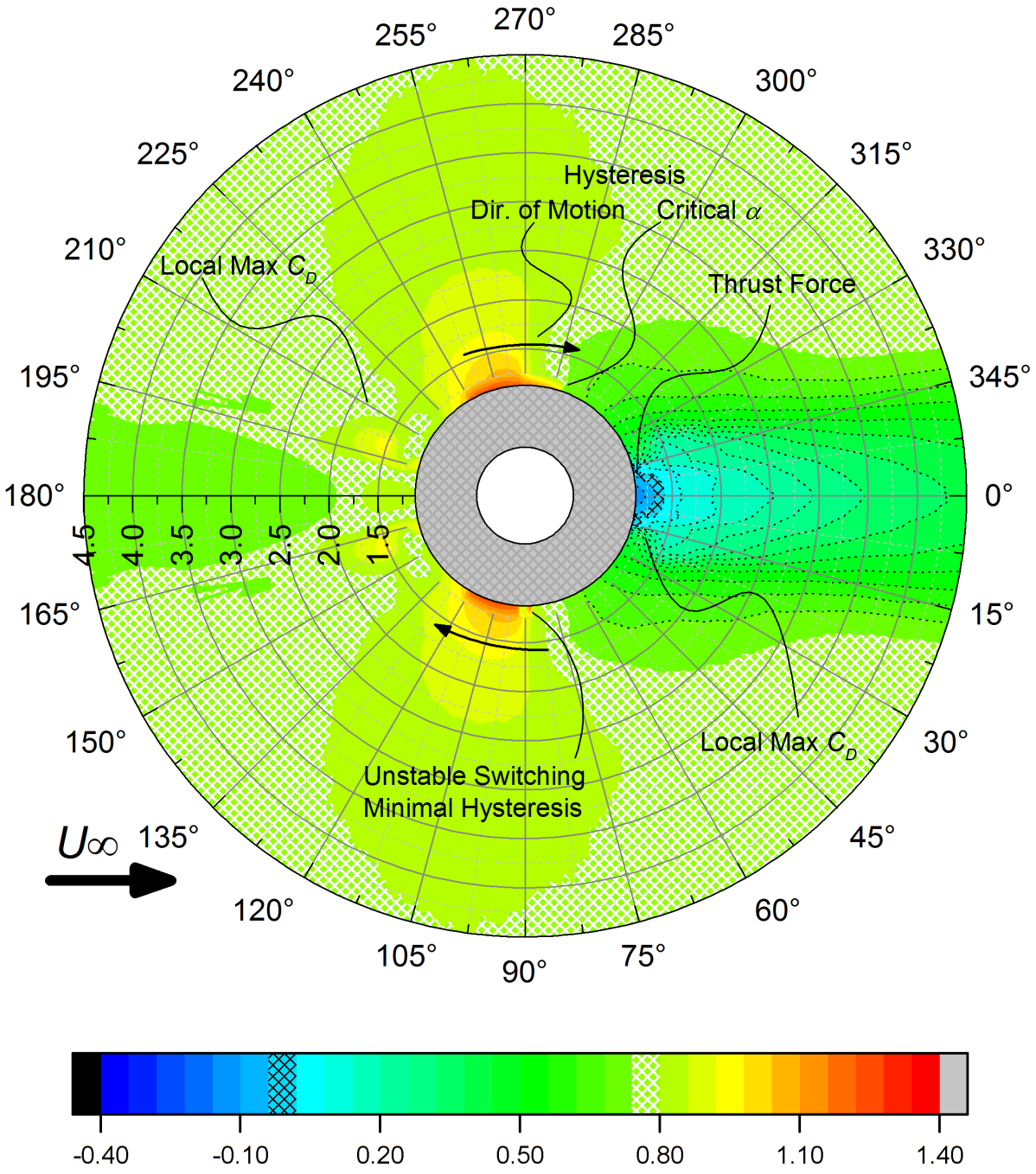

Figure 4.15: C_D contour plot for AR = 3. Contours displayed represent C_D for the outer cylinder placed at that point on the plot. In the context of hysteresis, the outer cylinder rotates clockwise around the central cylinder (α increasing from 0° to 360°). The white circle is the stationary reference cylinder, and the grey cross-hatching is the area where no data was collected. White cross-hatching is isolated cylinder value, black cross-hatching is $C_D = 0$. $P/D = 1.0$ represents the cylinders touching. Flow is from left to right.

4.4.2 Mean Lift Coefficient

Mean lift coefficient data, C_L, were obtained simultaneously with C_D for the entire range of staggered configurations. In a similar manner as C_D, contour plots showing lines of constant C_L were created for AR = 9, 7, 5, and 3 that may be found in Figures 4.17, 4.18, 4.19, and 4.20, respectively. A polar map of the data collection points for C_D and C_L may be found in Appendix A as well, with the C_L data separated by P/D found in Appendix B. As with C_D, three main regions may be identified for all AR that loosely align with the regions of wake interference, proximity interference, and no interference. These three regions are a region of negative C_L at low incidence angles (α = 0° to ~45°), a region of positive C_L near side-by-side (α = ~45° to 90°), and a zero-lift region found predominantly for the upstream cylinder at moderate to large P/D (α = 0° to ~45°). Generally, in all of these regions the magnitude of C_L decreases as P/D is increased with the peak values near $P/D \approx 1.25$; however, P/D = 1.125 often shows significantly different behaviour than that of larger P/D. The shapes of these regions and the magnitudes within them are a more complex function of AR. A decrease in AR generally broadens the regions with respect to α and shortens them with respect to P/D, with the magnitudes generally decreasing as well.

Small incidence angle flow regimes described by Sumner et al. (2000) are apparent in the lift contours (α = 0° to ~45° in Figures 4.17 through 4.20), most notably the occurrence of the "inner lift peak". For closely spaced infinite cylinders the inner lift peak is found at α = 9° (Sumner et al., 2005) and is characterized by a well-defined peak of negative C_L, reduced C_D, and increased St as a result of shear layer reattachment on the downstream cylinder. In contrast, the "outer lift peak" described by Sumner et al. (2005) occurs at larger P/D where the vortex impingement on the downstream cylinder causes a broader lower-magnitude peak of negative C_L, with no corresponding decrease in C_D, at α = 18°. The boundary between the inner and outer lift peaks as found by Sumner et al. (2005) for infinite cylinders was found to be between P/D = 2.5 and 3.0.

The C_L contours found in Figures 4.17 through 4.20 show significant gradients in C_L for the downstream cylinder at small α, and it can be seen that AR has a significant influence on the behaviour of C_L as the downstream cylinder sits within the separated shear layer of the upstream cylinder. Sumner et al. (2005) defines the transition from inner lift peak to outer lift peak as the P/D where the peak in C_L experiences a discontinuous jump to a larger α, as seen in Figure 4.16. The finite cylinders of AR = 9 and 7 do not show any jump, however, but only show the presence of the inner lift peak, while AR = 5 and 3 would seem to transition to the outer lift peak at only P/D = 1.5 (however the peaks are still initially sharp in nature, unlike the broader peaks expected for the outer lift peak). The finite cylinders of AR = 3 are unique, with the lift peak measured for the downstream cylinder significantly broader and offset farther from α = 0° than the higher aspect ratio cylinders.

The effects on the upstream cylinder are also influenced by aspect ratio. AR = 9, 7, and 5 show similar features, with a smaller area of influence concentrated near α = 15°. Small P/D in this range also produce a sharp negative C_L for the upstream cylinder. The cylinders of AR = 3, however, have a much wider area of influence (up to α = 45°) with a much weaker peak, much like the downstream cylinder. Aspect ratio has a large effect on the development of the lift peak, with the longer vortex formation length likely allowing AR = 9 and 7 cylinders to not transition to a vortex impingement flow pattern (characterized by the outer lift peak). AR = 3 is below the critical aspect ratio and has a different near wake and shear layer behaviour entirely, which may be why the lift peaks are fundamentally different when compared to larger AR. The cylinders of AR = 5 are likely in a transitional region, with the sharp peak in C_L at small P/D similar to higher AR cylinders while also having broad, weaker peaks at large P/D similar to AR = 3. Flow visualization of the shear layer interactions on the downstream cylinder may bring clarity to the classification of these lift peaks.

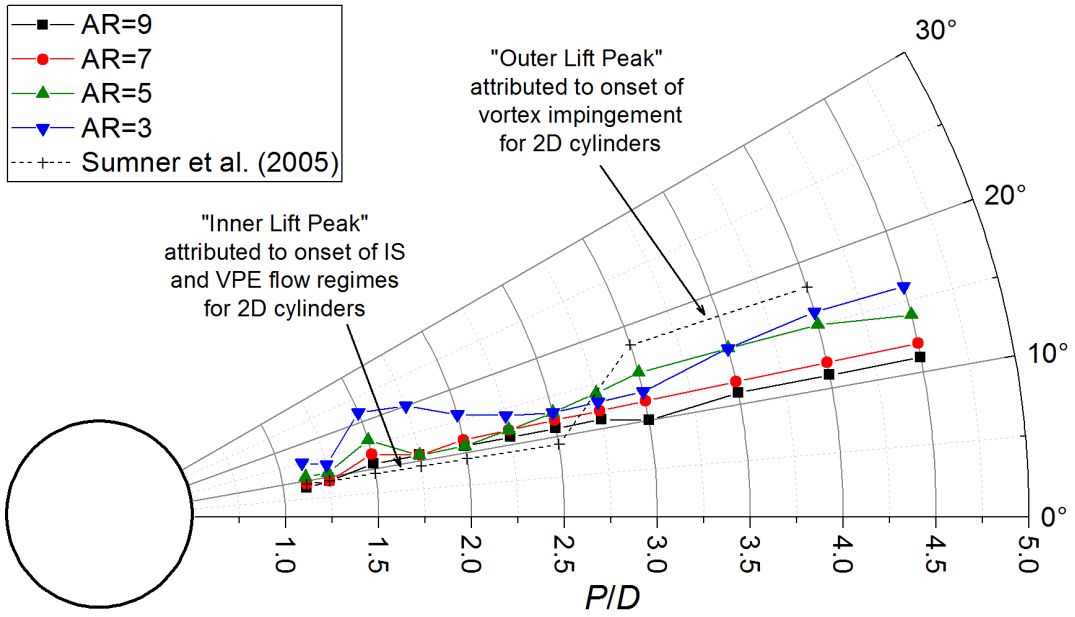

Figure 4.16: Peak negative C_L locations with respect to α for: ■, AR = 9; ●, AR = 7; ▲, AR = 5; ▼, AR = 3; and +, infinite cylinder data from Sumner et al. (2005).

The narrow band of low lift between the lift peaks for the downstream cylinder near tandem (Figures 4.17 through 4.20) is also a complex function of AR and P/D. Deviations from $\alpha = 0°$ at small P/D cause asymmetric shear layer reattachment to the outer side and a negative lift on both cylinders that attempts to realign them. For the downstream cylinder the small region of low C_L near tandem is quite narrow for $P/D \leq 1.25$ at around $\alpha = 5°$. Between $P/D = 1.25$ and 1.75 this region becomes wider, with AR = 9 up to $\alpha = 8°$ and AR = 3 up to 11°. For AR = 5 and 3 this marks a significant decrease in inner lift peak magnitude and sharpness as well as an increase α where the peak is found. For AR = 9 and 7 the shape and severity of the peaks remains unchanged, however a very slight increase in α is found. The upstream cylinder, however, has a far smaller P/D range where it experiences any $C_L \leq 0$ (between $P/D \leq 2.5$ -2.75, increasing slightly with decreasing AR). This could be related to the vortex formation length of the cylinder, and it is possible that $P/D \geq 2.75$ results in vortex formation and impingement rather that shear layer reattachment onto the downstream cylinder which provides far less feedback upstream.

Proximity interference found at large incidence angles (α = ~45° to 90°) produces exclusively a positive, repulsive C_L for $P/D \geq 1.25$ as found in Figures 4.17 through 4.20. This region is similar to the biased flow regime found with side-by-side cylinders as discussed in Section 4.3. In this case, the upstream cylinder has the narrow near wake with higher C_L and the downstream cylinder has the wide near wake with lower C_L. The proximity interference is highest when P/D is at its lowest, causing the magnitude of C_L to increase as P/D decreases. Conversely, at larger P/D both upstream and downstream cylinders experience lower values of C_L that are much closer to one another. An indication of the gap deflection angle is found in the magnitude of C_L, with zero lift indicating insignificant gap deflection as found at wide P/D. The aspect ratio has a large effect on what is considered a large P/D in this region, such that as AR is reduced a smaller P/D is required to produce zero lift (P/D = 4.0 for AR = 9 and only P/D = 2.75 for AR = 3). When comparing AR = 3 and AR = 9, the smaller region of positive C_L at large incidence angles contrasted against the larger region of negative C_L at low incidence angles would indicate that below the critical AR, wake interference becomes the larger influence.

Very small P/D behave drastically different than small and intermediate P/D. As described in Section 4.3, the base bleed flow regime found at P/D = 1.125 causes the bias side cylinder (in the staggered case, the upstream cylinder) to obtain an attractive C_L unlike any other P/D in the large incidence angle flow regimes. The non-bias side cylinder (in the staggered case, the downstream cylinder) obtains a repulsive C_L that is large in magnitude. Coupled with this largely different C_L is the presence of strong hysteresis at P/D = 1.125 for all AR. In Figures 4.17 through 4.20 the data are displayed such that the contours represent C_L on the outer cylinder as it rotates clockwise around the central cylinder (α increasing from 0° to 360°). Therefore the upper half of the contours (α = 180° to 360°) clearly shows the narrow region of attractive C_L that begins at $\alpha \approx 255°$ (15° before the side-by-side configuration) where the cylinder is upstream. This narrow region continues across α = 90° up to a critical α before abruptly changing back to the repulsive C_L that is expected of a downstream cylinder at P/D = 1.125. Similarly on the bottom half of the contours in Figure 4.17 through Figure 4.20 (α = 0° to 180°) where the cylinder is initially downstream the repulsive C_L experienced for $\alpha < 90°$ is maintained across to $\alpha > 90°$ before reaching the critical α, reverting C_L back to the attractive value expected for an upstream cylinder. The critical α and the P/D where this hysteresis occurs is a strong function of AR, and is discussed in Section 4.3.4 with additional graphs explicitly showing the phenomenon.

The third main region outlined in Figures 4.17 through 4.20 is the area of zero lift, specifically areas of minimal proximity interference and no wake interference. Though areas of zero lift occur at small P/D and for many of the tandem configurations, they are transitional regions between attractive and repulsive zones characterized by complex flow fields. The areas of minimal proximity interference occur predominantly with the upstream cylinder for large P/D > 2.75 and between α = 0° and ~45°. The vortex street formed behind the upstream cylinder may impinge on or be deflected by the presence of the downstream cylinder, though as the vortex is already shed it has less influence on the flow upstream than a free shear layer. Proximity interference only becomes significant for the upstream cylinder once large incidence angles are achieved. As AR is decreased larger α is possible while still maintaining negligible C_L.

Overall, the mean lift coefficient experienced by staggered finite cylinders is a complicated function of AR, P/D, and α. Three main regions were identified for each AR. Low incidence angles (α = 0° to ~45°) produce wake interference and regions of attractive C_L. High incidence angles (α = ~45° to 90°) produce proximity interference and generally result in repulsive C_L. Low incidence angles (α = 0° to ~45°) and large P/D (> 2.75) produce negligible wake or proximity interference for only the upstream cylinder resulting in negligible C_L. The shape of each region is also a strong function of AR, with AR = 3 experiencing smaller regions of positive lift and larger regions of negative lift. Conversely, AR = 9 and 7 experience larger regions of positive lift and smaller regions of negative lift. AR = 5 seems to be a transitional aspect ratio, with positive and negative lift regions intermediately sized between that of higher and lower AR.

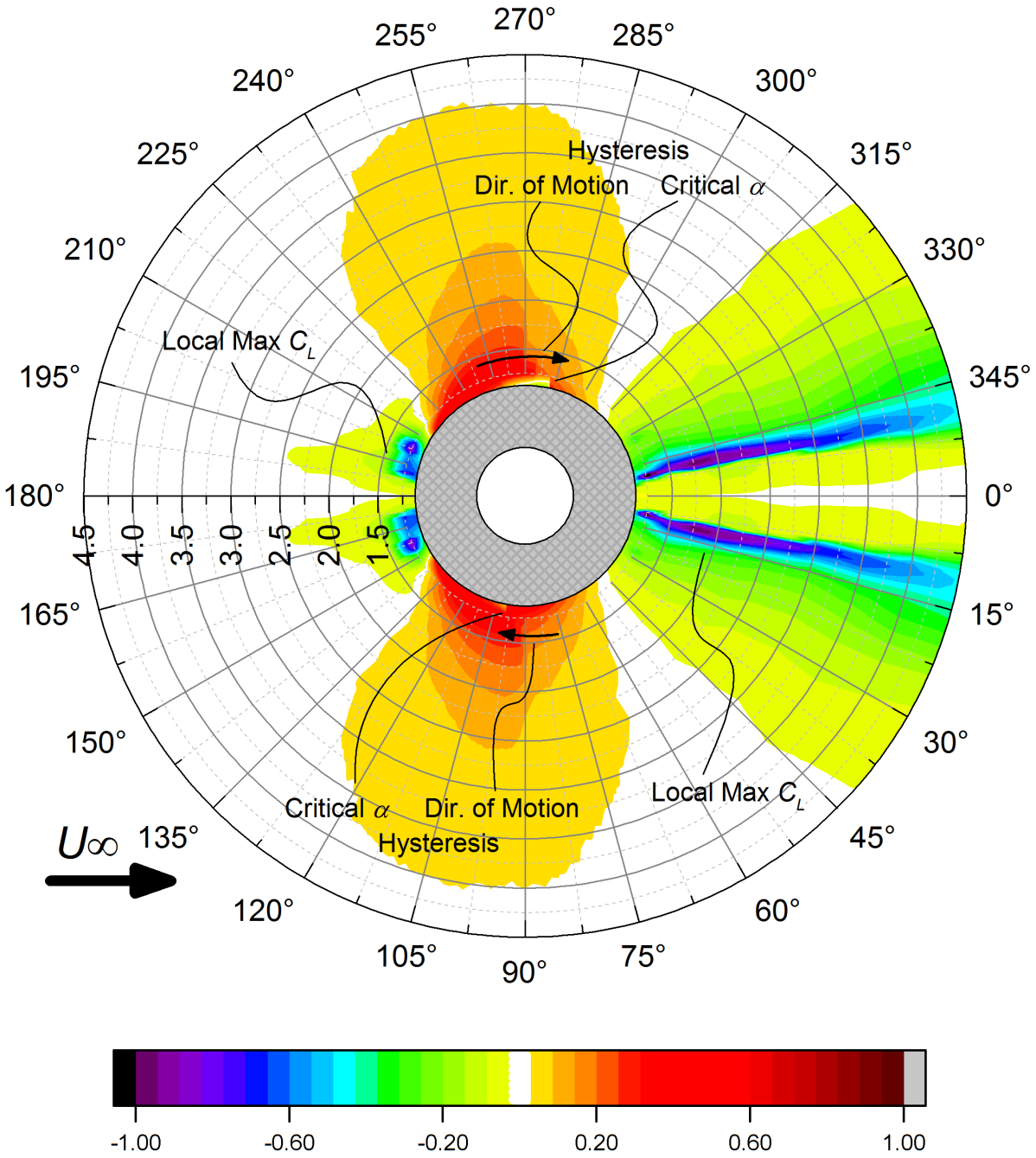

Figure 4.17: C_L contour plot for AR = 9. Contours displayed represent C_L for the outer cylinder placed at that point on the plot. In the context of hysteresis, the outer cylinder rotates clockwise around the central cylinder (α increasing from 0° to 360°). The white circle represents the stationary reference cylinder, and the grey cross-hatching represents the area where no data is collected. P/D = 1.0 represents the cylinders touching. Flow is from left to right.

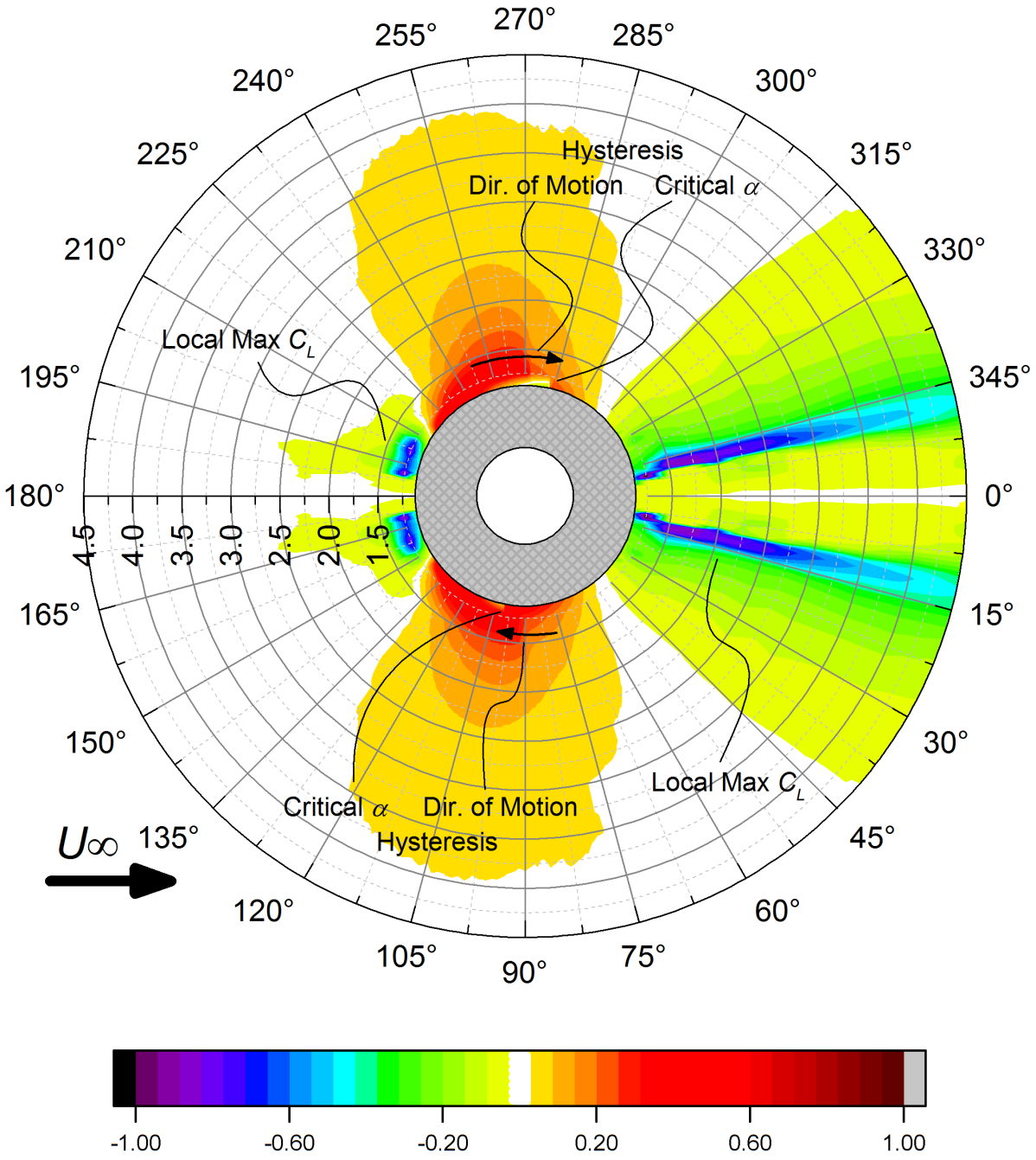

Figure 4.18: C_L contour plot for AR = 7. Contours displayed represent C_L for the outer cylinder placed at that point on the plot. In the context of hysteresis, the outer cylinder rotates clockwise around the central cylinder (α increasing from 0° to 360°). The white circle represents the stationary reference cylinder, and the grey cross-hatching represents the area where no data is collected. P/D = 1.0 represents the cylinders touching. Flow is from left to right.

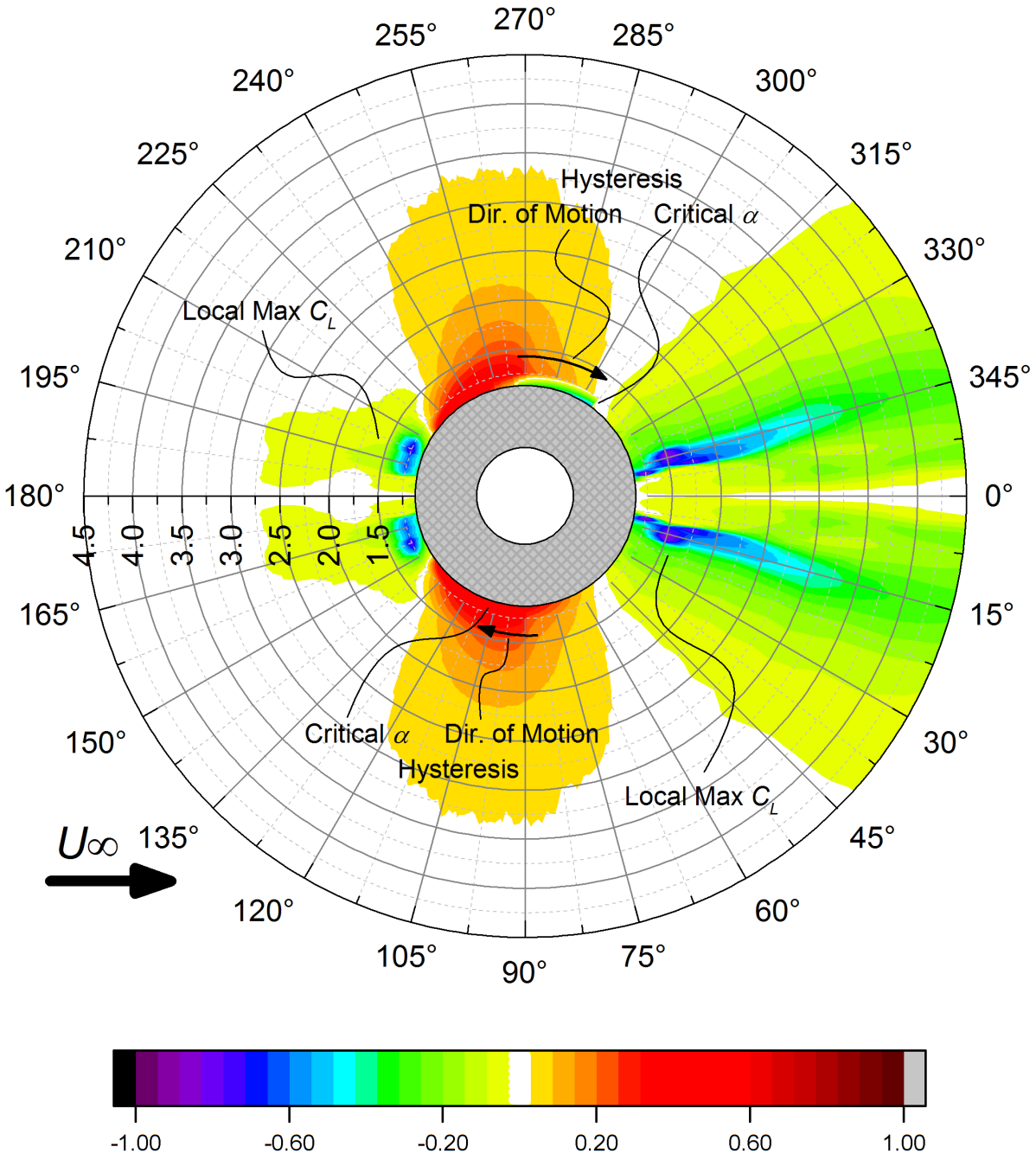

Figure 4.19: C_L contour plot for AR = 5. Contours displayed represent C_L for the outer cylinder placed at that point on the plot. In the context of hysteresis, the outer cylinder rotates clockwise around the central cylinder (α increasing from 0° to 360°). The white circle represents the stationary reference cylinder, and the grey cross-hatching represents the area where no data is collected. P/D = 1.0 represents the cylinders touching. Flow is from left to right.

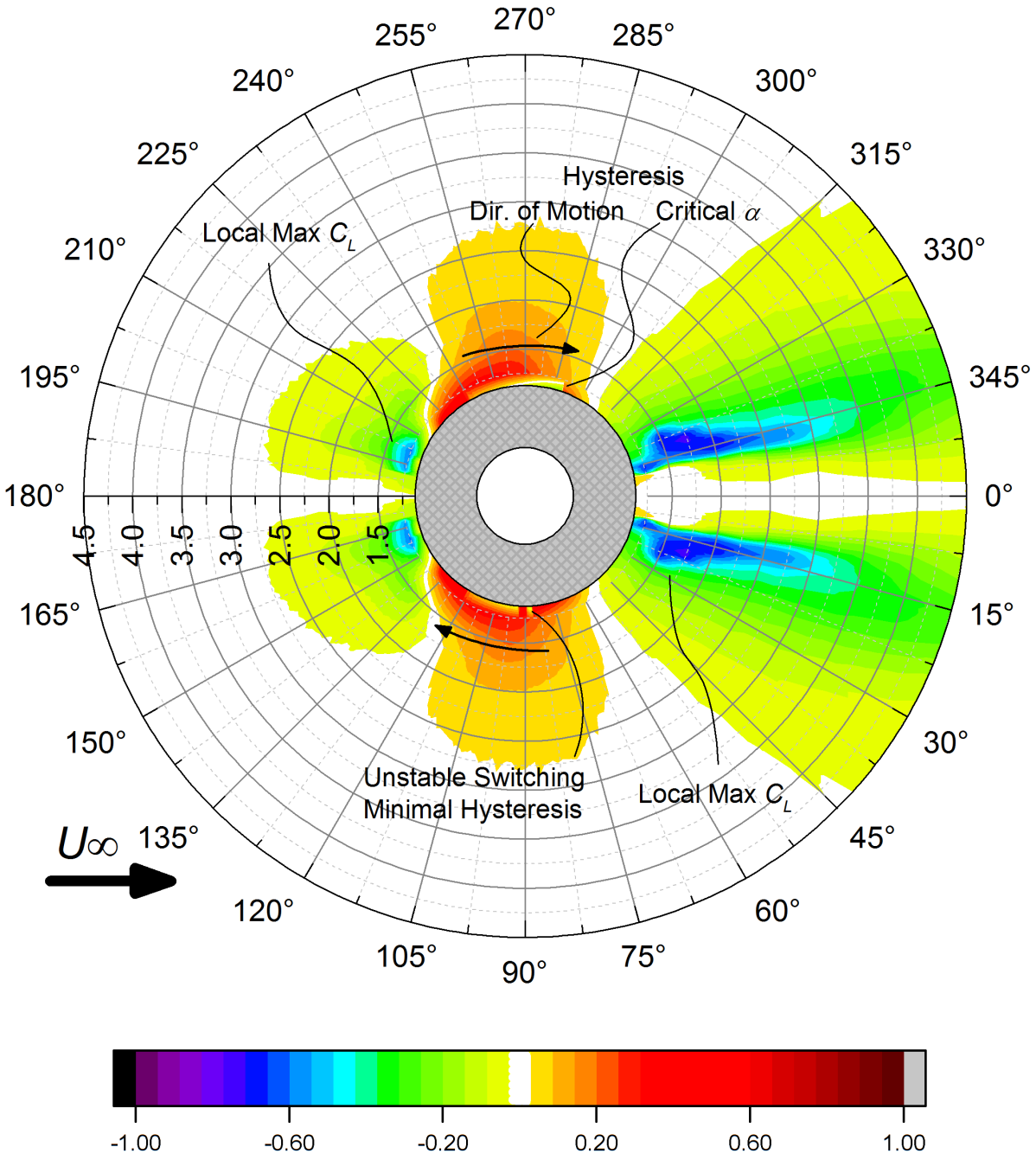

Figure 4.20: C_L contour plot for AR = 3. Contours displayed represent C_L for the outer cylinder placed at that point on the plot. In the context of hysteresis, the outer cylinder rotates clockwise around the central cylinder (α increasing from 0° to 360°). The white circle represents the stationary reference cylinder, and the grey cross-hatching represents the area where no data is collected. P/D = 1.0 represents the cylinders touching. Flow is from left to right.

4.4.3 Strouhal Number

Strouhal number data were acquired for both the upstream and downstream cylinder simultaneously across the entire staggered range from α = 0° to 90° for the same 12 discrete P/D used for C_D and C_L. As detailed in Section 4.2.2, velocity fluctuation power spectra were measured via one stationary hot-wire probe behind the fixed central cylinder while another moveable hot-wire probe tracked the rotating outer cylinder over the range of P/D and α. In a similar manner as the C_D and C_L data, the St data were compiled into contours for AR = 9, 7, 5, and 3, and can be found in Figure 4.21 and Figure 4.22. Polar maps of the data collection points for St may be found in Appendix A, with gaps along certain α (predominantly near the inner lift peak) where no discernable peaks were found in the velocity fluctuation power spectra. The St data separated by P/D are found in Appendix B as well. The St contours can be divided into three main regions, however the α and P/D boundaries as defined by C_D in Section 4.4.1 and C_L in Section 4.4.2 do not align well with the St contours. There is a wake interference region at low incidence angles (α = 0° to ~20°), a biased flow-like region found at moderate and high incidence angles (α = ~20° to 90°), and a region of negligible interference found for both cylinders at large P/D (boundaries are dependent on AR).

At low incidence angles (α < ~20°) wake interference is dominant. The St data have some limitations however, as the hot-wire probes were positioned at x/D = 3.0, y/D = 1.0, and z/H = 0.5 relative to the cylinders. Consequently, for P/D < 3.0 the upstream probe is actually situated behind the downstream cylinder, meaning there will be some ambiguity in the interpretation of St for these staggered configurations. Without the use of flow visualization or whole field techniques, or different hot-wire techniques, the upstream cylinder St behaviour is more difficult to interpret for low incidence angles.

The St contours found in Figure 4.21 and Figure 4.22 show a local maximum in St for the downstream cylinder at an α that coincides with the inner lift peak described in Section 4.4.2 (approximately α = 12° to 15°). Measuring St in this region was challenging, however, with the positioning of the probes influencing the measured velocity fluctuation power spectra. The Strouhal number was only measured at the mid-height of the cylinders, and AR has a large effect on the vortex formation along the height of the cylinder. In some instances the upstream cylinder showed a peak in the power spectra in this region, however, more often the power spectra

showed no coherent peak for small and intermediate P/D between α = ~8° to 16°, even when moving the probe around in the x-y plane. The absence of clear St values may also be in part due to the upstream probe being positioned either behind or very close to the downstream cylinder.

The behaviour of St for α > 20° remains fairly constant, with P/D being the larger influence for both the upstream and downstream cylinders. As described in Section 4.4.1, the gap flow between the cylinders becomes biased toward the upstream cylinder. The result is the upstream cylinder has a narrow near wake and a higher St, while the downstream cylinder has a wide near wake and a lower St. A similar result is found for all AR, with the difference between the two St values a strong function of P/D. Increasing P/D reduces the proximity interference, and results in St values that asymptotically approach that of an isolated finite cylinder. For this entire region the downstream cylinder (low St mode) remains just below the St of an isolated cylinder, where the upstream cylinder (high St mode) can experience a severe gradient at small P/D. For an increase in AR, the region in which the upstream and downstream cylinders have not yet attained the isolated cylinder St increases in P/D.

The St contours in Figure 4.21 and Figure 4.22 show a fairly consistent divide between high and low St ranges at α = 90°. Intermittent switching of the gap bias direction is likely at this incidence angle at low P/D, and this topic is discussed at length in Section 4.3.3 and Appendix C. The power spectra over a range of α near 90° (the range increases as P/D decreases) show the same two distinct peaks for both probes, corresponding to the low and high St values, indicating at least one gap bias switch during the 30 s sample time.

When at α = 90°, both wake states are equally likely, though flow stability found at lower P/D can cause the gap flow bias to remain in one direction for longer periods of time before switching sides. When α is brought away from 90° however, the high St (narrow) wake state becomes more likely for the upstream cylinder, while the low St (wide) wake state becomes more likely for the downstream cylinder. This is found in the power spectra data at staggered angles near α = 90°, however increasing P/D causes the upstream and downstream St to converge. The lack of difference between the two states results in one wider power spectra peak likely comprised of two indiscernible peaks of similar value. The shared St at wider P/D very close to α = 90° described in Section 4.3.3 earlier is a fairly good indication of the departure from the biased flow regime as summarized in Table 4.1, however the repulsive C_L in this region

still shows the proximity interference of the co-shedding regime. Moving to an incidence angle farther from $\alpha = 90°$ extends the P/D "range" of the bias flow-like regime on the St contours as the effective P/D is reduced slightly however.

The strong hysteresis found in the C_D and C_L contours near the side-by-side configuration is not nearly as apparent in the St contours, which is why the St data are not divided by CW and CCW α increments. This may be for a number of reasons. The most severe (and therefore easiest to identify) hysteresis is at $P/D = 1.125$ where the extended-body flow regime occurs, at which point only one Kármán vortex street is produced. The result is only one St measured by both probes at approximately half the value of an isolated cylinder as discussed in Section 4.3.3. Looking at the data for $P/D \geq 1.25$, neither AR = 3 nor 5 experience hysteresis, AR = 7 experiences only a few degrees of hysteresis at only $P/D = 1.25$, and AR = 9 has notable hysteresis at $P/D = 1.25$ (although the 30 s sampling time for a power spectrum increases the chance that a small disturbance will flip the wake states during the measurement). Thus only a few degrees of hysteresis were produced for AR = 9 at $P/D = 1.25$, however this is almost negligible when compared to the highly repeatable hysteresis found with C_D and C_L.

With the exception of small incidence angles, large P/D configurations found in Figure 4.21 and Figure 4.22 show similar St values for both upstream and downstream cylinders that match the isolated finite cylinder St data. This region of reduced proximity interference with respect to St does not align very well with those defined by C_D and C_L in Sections 4.4.1 and 4.4.2. Near side-by-side and at very large incidence angles, the St contours approach isolated finite cylinder values of St at lower P/D than in surrounding regions, where the C_D and C_L contours near the side-by-side configurations showed significant proximity effects. Conversely, where the C_D and C_L contours had shallow gradients near $\alpha = 45°$ for the upstream cylinder, the St contours experience their largest magnitude change. The highest values of St were found near $\alpha = 45°$, making it a useful reference for defining the critical P/D that produces no significant proximity interference. As AR is reduced, the critical P/D reduces significantly at $P/D = 4.0$, 3.5, 2.75, and 2.25 for AR = 9, 7, 5, and 3, respectively. This trending of critical P/D with respect to AR is similar to that found with C_D and C_L. Overall, a reduction in AR reduces the proximity interference effects, especially for the upstream cylinder.

In summary, the vortex shedding frequencies measured for both upstream and downstream cylinders in a staggered configuration were divided into three main regions, however the P/D and α boundaries did not align well with those identified for C_D and C_L in Sections 4.4.1 and 4.4.2. The wake interference region at low incidence angles (α = 0° to ~20°) was characterized by a low St with a local maximum at the inner lift peak. The proximity interference region at moderate and high incidence angles (α = ~20° to 90°) showed biased flow-like characteristics with the upstream cylinder having a higher St compared to the downstream cylinder. Finally the region of negligible interference was found at wide P/D, though the boundaries were dependent on AR.

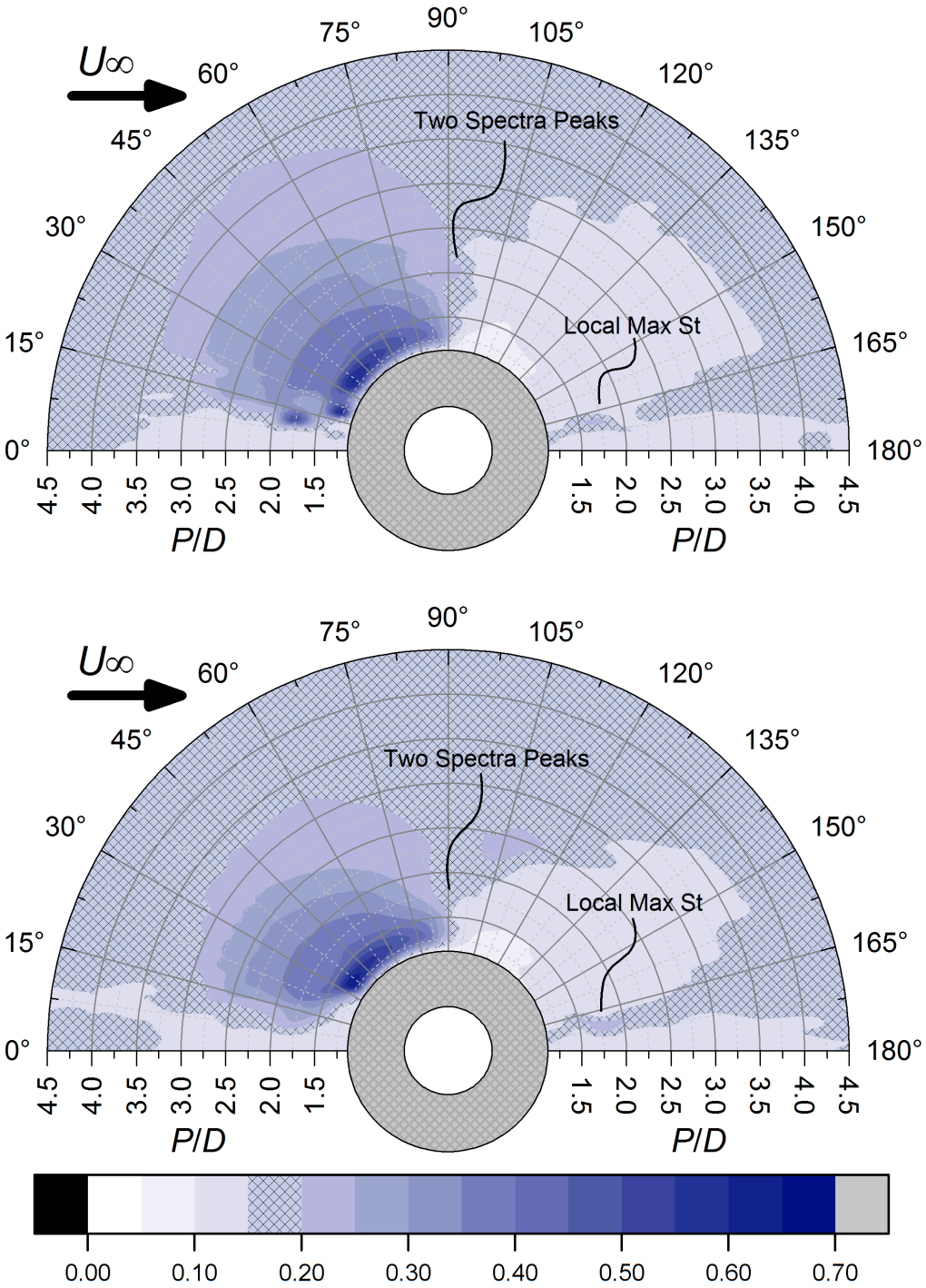

Figure 4.21: St contour plots for AR = 9 (top) and AR = 7 (bottom). Contours displayed are St for the outer cylinder placed at that point on the plot. The white circle is the stationary reference cylinder, and the grey cross-hatching is the area where no data was collected. Black cross-hatching is isolated cylinder value. *P*/*D* = 1.0 represents the cylinders touching. Flow is from left to right.

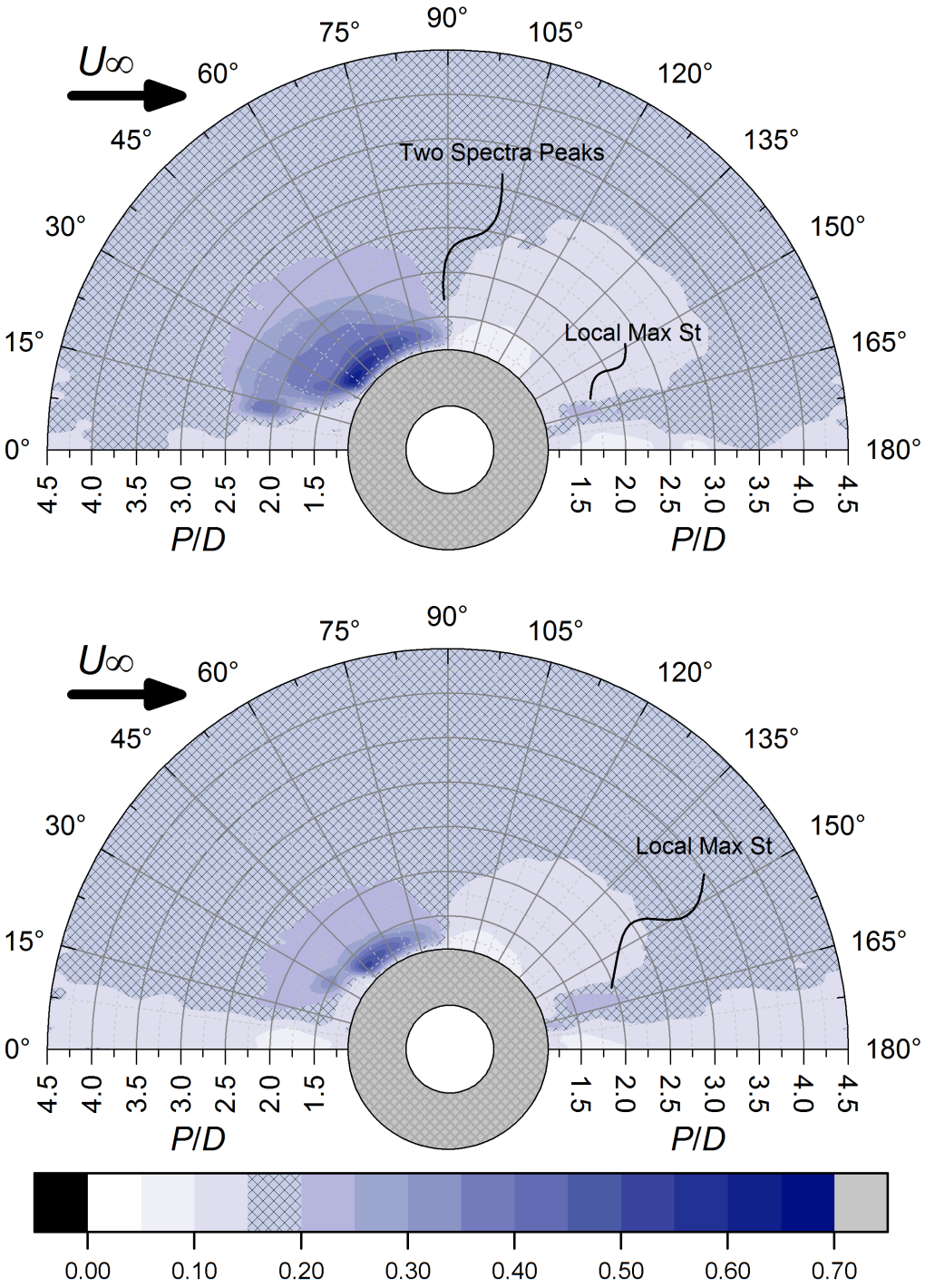

Figure 4.22: St contour plots for AR = 5 (top) and AR = 3 (bottom). Contours displayed are St for the outer cylinder placed at that point on the plot. The white circle is the stationary reference cylinder, and the grey cross-hatching is the area where no data was collected. Black cross-hatching is isolated cylinder value. *P*/*D* = 1.0 represents the cylinders touching. Flow is from left to right.

Chapter 5 Conclusions, Contributions, and Recommendations

5.1 Conclusions

In the present research, the effects of aspect ratio on the wind loading and vortex shedding frequency of two surface-mounted finite-height cylinders in a staggered configuration were studied using a low-speed, closed return wind tunnel. Mean drag and lift force coefficients (C_D and C_L) were measured on the central cylinder (of the two-cylinder staggered arrangement) using a force balance while the non-instrumented outer cylinder was located at discrete pitch ratios (P/D) and rotated to different incidence angles (α) relative to the central cylinder. Measurements of the Strouhal number (St) were made simultaneously for both cylinders. The cylinder aspect ratio (AR), P/D and α were varied systematically to obtain a large set of data for C_D, C_L, and St for every combination of P/D and α at AR = 9, 7, 5, and 3. The data were divided into three main configurations for analysis purposes: tandem, side-by-side, and staggered. All of the experiments were conducted at a single Reynolds number and a single boundary layer thickness.

Aspect ratio and pitch ratio effects on C_D and St were first studied for cylinders in a tandem configuration ($\alpha = 0°$). The drag coefficients of the upstream cylinders became lower as AR was decreased, consistent with isolated finite-height cylinders. The downstream cylinders however, showed more complex behaviour. For small P/D (≤ 2.0) a decrease in AR produced an increase in C_D (for small P/D this equated to a reduction in net thrust). At lower AR, it was suggested that increased downwash behind the upstream cylinder resulted in an increase in freestream impingement over a larger portion of the downstream cylinder, increasing the pressure in the gap between the two cylinders and C_D of the downstream cylinder while reducing C_D for the upstream cylinder. Within the C_D data there was no abrupt increase to mark the onset of co-shedding as seen for two infinite cylinders in tandem. This may be a result of the longer vortex formation length found with finite-height cylinders allowing shear layer reattachment to persist up to the largest P/D (= 4.5) measured. Additionally, it may be caused by two flow patterns coexisting in different regions along the cylinder heights. The result would be a smaller abrupt increase in C_D, or perhaps just a smooth transition as a larger portion of the height experiences co-shedding as P/D increases. In contrast, the mid-height St data showed a small jump for all AR, to the value expected for isolated finite cylinders, however this only represents the vortex shedding at the mid-height, and does not reflect any heightwise variation in St.

Measurements of C_D, C_L, and St were then presented for cylinders in a side-by-side configuration ($\alpha = 90°$). At $P/D = 1.125$ the base bleed flow regime was identified for the two finite cylinders, characterized by one cylinder experiencing a significantly higher C_D and an attractive C_L; this was apparent for all AR, and much like the tandem configuration, a lower AR resulted in a smaller C_D. Similar to the infinite cylinder results of Sumner et al. (2005) for $P/D \geq 1.25$, an abrupt jump to the biased flow regime occurs for all AR, where the finite cylinder with the narrow wake state experiences a higher C_D, C_L, and St, and where the finite cylinder with the wide wake state experiences a lower C_D, C_L, and St. The behaviour of the biased flow regime is sensitive to AR, where an increase in AR increases the critical value of P/D signifying the upper limit of the biased flow regime (and the differences in the magnitudes of C_D, C_L, and St between the two wake states). Defining the exact transition between the biased and co-shedding flow regimes was difficult as at intermediate P/D the gap bias direction intermittently switches sides. As C_D, C_L, and St were time-averaged values the measurements tended to show one value representing the average of both wake states (as opposed to two distinct values found at smaller P/D, where increased gap stability would allow the gap bias to stay preferentially to one side throughout the entire measurement averaging period).

An interesting hysteresis phenomenon was found at small P/D (≤ 1.75) near $\alpha = 90°$ where C_D and C_L experienced by the central cylinder were different depending on whether α was incremented CW or CCW. The initial values of C_D and C_L obtained by the central cylinder *before* $\alpha = 90°$ would be maintained *after* $\alpha = 90°$ up to a critical α, at which point both C_D and C_L would experience a sudden jump to the values expected by the opposing wake state. The size of the hysteretic range of α and the P/D that could produce hysteresis were both functions of AR. An increase in AR showed hysteresis at larger P/D with more repeatable critical α limits. A decrease in AR caused the potential for a larger hysteretic range of α, however the results were less repeatable and hysteresis was only found at smaller P/D.

For the staggered finite cylinders, contour plots of C_D, C_L, and St were produced for all AR to visually display the regions of wake and or proximity interference. Characteristics of the inner lift peak described by Sumner et al. (2005) are apparent in the data for C_D, C_L, and St, however the distinction between inner and outer lift peaks become less clear with surface-mounted finite-height cylinders. The sizes and shapes of the regions in the contour plots

experiencing wake and or proximity interference were sensitive to AR as well. As AR increases, strong wake interference effects were found at higher P/D, however as AR decreases wake interference effects are found at α farther from tandem. In the context of large incidence angle flow regimes, proximity interference at large P/D was found to increase at AR was increased. Overall, higher AR cylinders experienced a larger magnitude range of C_D, C_L, and St with steeper gradients throughout the entire staggered range. Additionally, higher AR cylinders experienced the effect of the other cylinder up to larger P/D than smaller AR cylinders.

For all staggered configurations, the data for AR = 3 behaved in a distinct fashion with changes in pitch ratio and incidence angle. This behaviour demonstrated that these cylinders were below the critical aspect ratio.

Overall, the differences between two infinite cylinders and two finite cylinders in a staggered configuration were found to be significant, due to the effects of aspect ratio and the greater complexity of the flow field for finite cylinders. This finding means that wind loading and vortex shedding data acquired for infinite cylinders should be used with caution when applied to engineering structures that are more appropriately represented by finite cylinders.

5.2 Contributions of this Work

The work presented in this thesis provides a systematic look at how the aspect ratio affects the wind loading and vortex shedding for both the upstream and downstream cylinders in a staggered configuration. No similar systematic study of aspect ratio effects for the flow around two surface-mounted finite-height finite cylinders exists in the literature to date. The data are presented in easy to read contours in addition to graphs displaying precise data sets. Evidence of strong hysteresis in the wind loading near $\alpha = 90°$ has not been extensively reported in other studies of two cylinders in cross-flow, and warrants further investigation as the sudden jump in C_D and C_L at the end of the hysteretic range produce strong impulsive loading on the cylinders. This thesis also provided a review of the C_D, C_L, and St classifications for the narrow and wide wake states found for the side-by-side configuration by Alam et al. (2003a), Sumner et al. (2005), and the present data, ultimately providing a reconciliation between the current designations.

5.3 Recommendations for Future Work

Limitations on both time and experimental complexity meant that this thesis is also limited in both its breadth and depth. The recommendations for future work involve considerations for new experiments and improvement on existing ones. The first recommendation would be to utilize flow visualization or whole field measurements techniques (such as particle image velocimetry) that would capture the complex flow field near the free ends and cylinder-wall junctions. These techniques would be valuable in understanding the root cause of the wind load and vortex shedding variations found for different AR that could only be speculated in the present thesis.

Improvement on apparatus limitations are also strongly recommended. A finer increment of P/D at very close cylinder spacing with less positioning uncertainty would be beneficial in describing the large variation in flow regimes currently presented. Finding exact boundaries between the flow patterns as a function of AR was challenging when each discrete P/D experienced a significantly different C_D, C_L, and St. Conversely, a method of measuring C_D, C_L, and St at cylinder spacing larger than the upper limit of $P/D = 4.5$ presented in this thesis would be useful. The true range of proximity and wake interference cannot be fully defined if the P/D range tested does not produce fully isolated-cylinder-like results. A larger P/D is needed, especially in the case of finite-height cylinders that were shown to produce proximity effects at larger P/D than infinite cylinders. Improvements to the method of obtaining C_D and C_L would also be of benefit, with the ability to measure the wind load on both cylinders simultaneously for small P/D recommended. Simultaneous force measurement (with each cylinder attached to its own, dedicated force balance) in conjunction with recording and analyzing the force time series data for both cylinders would provide greater insight into flow regimes that may switch back and forth intermittently (for example the biased flow regime for the side-by-side configuration discussed in Appendix C). Finally, a form of temperature compensation for either the freestream temperature or the temperature sensitive load cells used to measure C_D and C_L is recommended. A significant portion of the measurement time for the C_D and C_L data presented in this thesis was spent checking the force balance offsets, to minimize the impact of temperature drift on the measurement error; this was time that could have been better spent gathering additional data. A method of reducing the temperature effects would save a significant amount of experiment time, equipment wear, and thermal swelling of the ground plane and turntable assembly.

References

Adaramola, M. S., Akinlade, O. J., Sumner, D., Bergstrom, D. J., & Schenstead, A. J. (2006). Turbulent wake of a finite circular cylinder of small aspect ratio. *Journal of Fluids and Structures, 22*, 919-928.

Adaramola, M., Sumner, D., & Bergstrom, D. (2010). Effect of velocity ratio on the streamwise vortex structures in the wake of a stack. *Journal of Fluids and Structures, 26*, 1-18.

Alam, M. M., & Zhou, Y. (2007). Flow around two side-by-side closely spaced circular cylinders. *Journal of Fluids and Structures, 23*, 799-805.

Alam, M., Moriya, M., & Sakamoto, H. (2003a). Aerodynamic characteristics of two side-by-side circular cylinders and application of wavelet analysis on the switching phenomenon. *Journal of Fluids and Structures, 18*, 325-346.

Alam, M. M., Moriya, M., Takai, K., & Sakamoto, H. (2003b). Fluctuating fluid forces acting on two circular cylinders in a tandem arrangement at a subcritical Reynolds number. *Journal of Wind Engineering and Industrial Aerodynamics, 91*, 139-154.

ASME. (2012, August). *Pressure Vessels Ensure Safety*. Retrieved July 25, 2018, from American Society of Mechanical Engineers: https://www.asme.org/engineering-topics/articles/pressure-vessels/pressure-vessels-ensure-safety

Beitel, A. (2017). *The effect of aspect ratio on the aerodynamic forces and free end pressure distribution for a surface-mounted finite-height cylinder.* M.Sc. Thesis, Mechanical Engineering, University of Saskatchewan.

Beitel, A., & Sumner, D. (2017). The effect of aspect ratio on the normal force and bending moment coefficients for a surface-mounted finite cylinder. *4th Symposium on Flui-Structure-Sound interactions and Control (FSSIC 2017).* 21-24 August, 2017, Tokyo, Japan.

Coutanceau, M., & Defaye, J. (1991). Circular Cylinder Wake Configurations: A Flow Visualization Survey. *Applied Mechanics Reviews, 44*, 255-305.

Gerhardt, H. J., & Kramer, C. (1981). Interference effects for groups of stacks. *Journal of Wind Engineering and Industrial Aerodynamics, 8*, 195-202.

Heseltine, J. (2003). *Flow Around a Circular Cylinder with a Free End.* M.Sc. Thesis, Mechanical Engineering, University of Saskatchewan.

Hu, J., & Zhou, Y. (2008). Flow structure behind two staggered circular cylinders. Part 1. Downstream evolution and classification. *Journal of Fluid Mechanics, 607*, 51-80.

Igarashi, T. (1981). Characteristics of the flow around two circular cylinders arranged in tandem (1st report). *Bulletin of the JSME, 24*, 323-331.

Igarashi, T., Nakamura, H., & Fukuoka, T. (2004). Pressure drop and heat transfer of arrays of in-line circular blocks on the wall of parallel channel. *International Journal of Heat and Mass Transfer, 47*, 4547-4557.

Igbalajobi, A., McClean, J., Sumner, D., & Bergstrom, D. (2013). The effect of a wake-mounted splitter plate on the flow around a surface-mounted finite-height circular cylinder. *Journal of Fluids and Structures, 37*, 185-200.

Kim, T., & Christensen, K. (2018). Flow interactions between streamwise-aligned tandem cylinders in turbulent channel flow. *AIAA Journal, 56*, 1421-1433.

Lee, L. (1997). Wake structure behind a circular cylinder with a free end. *Proceedings of the Heat Transfer and Fluids Mechanics Institute, 35*, pp. 241-251.

Li, H., & Sumner, D. (2009). Vortex shedding from two finite circular cylinders in a staggered configuration. *Journal of Fluids and Structures, 25*, 479-505.

Liu, Y., & Cui, Z. X. (2006). Two side-by-side cantilevered cylinders in cross flow. *2006 ASME Pressure Vessels and Piping Division Conference*, (pp. PVP2006-ICPVT-11-93894). 23-27 July 2006. Vancouver, Canada.

Ljungkrona, L., & Sundén, B. (1993). Flow visualization and surface pressure measurement on two tubes in an inline arrangement. *Experimental Thermal and Fluid Science, 6*, 15-27.

Luo, S. C., Gan, T. L., & Chew, Y. T. (1996). Uniform flow past one (or two in tandem) finite length cylinder(s). *Journal of Wind Engineering and Industrial Aerodynamics, 59*, 69-93.

Noca, F., Park, H. G., & Gharib, M. (1998). Vortex formation length of a circular cylinder (300 < Re < 4,000) Using DPIV. *1998 ASME Fluids Engineering Division Annual Summer Meeting.* 21-25 June 1998. Washington, DC, USA: ASME.

Petersen, R., Cochran, B., & LeCompte, J. (2002). Specifying exhaust systems that avoid fume reentry and adverse health effects. *ASHRAE Transactions, 108*, Article ID# HI-02-15-3.

Portela, G., & Godoy, L. (2005). Shielding effects and buckling of steel tanks in tandem arrays under wind pressures. *Wind and Structures, 8*, 325-342.

Portela, G., & Godoy, L. (2007). Wind pressure and buckling of steel tanks. *Wind and Structures, 10*, 23-44.

Porteous, R., Moreau, D. J., & Doolan, C. J. (2014). A review of flow-induced noise from finite wall-mounted cylinders. *Journal of Fluids and Structures, 51*, 240-254.

Reddy, K. S., & Poddar, K. (2008). Uniform flow over two side-by-side finite length circular cylinders at high Reynolds numbers. *46th AIAA Aerospace Sciences Meeting and Exhibit*, (pp. AIAA 2008-372). 7-10 January 2008. Reno, Nevada, USA.

Rooney, D. M., Rodichok, J., & Dolan, K. (1995). Finite aspect ratio effects on vortex shedding behind two cylinders at angles of incidence. *Transactions of the ASME: Journal of Fluids Engineering, 117*, 219-225.

Rostamy, N. (2012). *Fundamental studies of the wake structure for surface-mounted finite-height cylinders and prisms.* PhD Thesis, Mechanical Engineering, University of Saskatchewan.

Rostamy, N., Sumner, D., Bergstrom, D., & Bugg, J. (2012). Local flow field of a surface-mounted finite circular cylinder. *Journal of Fluids and Structures, 34*, 105-122.

Said, N. M., Mhiri, H., Bournot, H., & Le Palec, G. (2008). Experimental and numerical modelling of the three-dimensional incompressible flow behaviour in the near wake of circular cylinders. *Journal of Wind Engineering and Industrial Aerodynamics, 96*, 472-502.

Sumner, D. (2010). Two circular cylinders in cross-flow: A review. *Journal of Fluids and Structures, 26*, 849-899.

Sumner, D. (2013). Flow above the free end of a surface-mounted finite-height circular cylinder: A review. *Journal of Fluids and Structures, 43*, 41-63.

Sumner, D., & Li, H. (2014). Wake interference effects for two surface-mounted finite cylinders in a tandem configuration. *ASME 2014 Pressure Vessels & Piping Conference*, (pp. PVP2014-28056). 20-24 July 2014. Anaheim, California, USA.

Sumner, D., Heseltine, J., & Dansereau, O. (2004). Wake structure of a finite circular cylinder of small aspect ratio. *Experiments in Fluids, 37*, 720-730.

Sumner, D., Heseltine, J., & Dansereau, O. (2004). Wake structure of a finite circular cylinder of small aspect ratio. *Experiments in Fluids, 37*, 720-730.

Sumner, D., Price, S., & Paidoussis, M. (2000). Flow-pattern identification for two staggered circular cylinders in cross-flow. *Journal of Fluid Mechanics, 411*, 263-303.

Sumner, D., Richards, M., & Akosile, O. (2005). Two staggered circular cylinders of equal diameter in cross-flow. *Journal of Fluids and Structures, 20*, 255-276.

Sumner, D., Rostamy, N., Bergstrom, D., & Bugg, J. (2015). Influence of aspect ratio on the flow above the free end of a surface-mounted finite cylinder. *International Journal of Heat and Fluid Flow, 56*, 290-304.

Sumner, D., Rostamy, N., Bergstrom, D., & Bugg, J. (2017). Influence of aspect ratio on the mean flow field of a surface-mounted finite-height square prism. *International Journal of Heat and Fluid Flow, 65*, 1-20.

Taniguchi, S., Sakamoto, H., & Arie, M. (1982). Interference between two circular cylinders of finite height vertically immersed in a turbulent boundary layer. *Transactions of the ASME: Journal of Fluids Engineering, 104*, 529-536.

Wang, H., Zhou, Y., & Mi, J. (2012). Effects of aspect ratio on the drag of a wall-mounted finite-length cylinder in subcritical and critical regimes. *Experiments in Fluids, 53*, 423-436.

Wang, H., Zhou, Y., Chan, C., & Lam, K. (2006). Effect of initial conditions on interaction between a boundary layer and a wall-mounted finite-length-cylinder wake. *Physics of Fluids, 18*, Article ID# 065106.

Williamson, C. (1996). Vortex Dynamics in the Cylinder Wake. *Annual Review of Fluid Mechanics, 28*, 477-539.

Wu, X., Ge, F., & Hong, Y. (2012). A review of recent studies on vortex-induced vibrations of long slender cylinders. *Journal of Fluids and Structures, 28*, 292-308.

Zdravkovich, M. (1977). Review of Flow Interference Between Two Circular Cylinders in Various Arrangements. *Transactions of the ASME: Journal of Fluids Engineering, 99*, 618-633.

Zhang, H., Yang, J., Xiao, L., & Lü, H. (2015). Large-eddy simulation of the flow past both finite and infinite circular cylinders at Re = 3900. *Journal of Hydrodynamics, 27*, 195-203.

Zhou, Y., & Alam, M. (2016). Wake of two interacting circular cylinders: A review. *International Journal of Heat and Fluid Flow, 62*, 510-537.

Zhou, Y., Feng, X., Alam, M., & Bai, H. (2009). Reynolds number effect on the wake of two staggered cylinders. *Physics of Fluids, 21,* Article ID# 125105.

Appendix A Map of Data Collection Points

A map of the data collection points for the force balance measurements are found in Figure A.1. Maps for the St data collection points for AR = 9, 7, 5, and 3 are found in Figure A.2a, Figure A.2b, Figure A.2c, and Figure A.2d, respectively.

Force balance measurements of C_D and C_L were made simultaneously from the central cylinder at each of the points in Figure A.1. The test trajectory for each AR was the same, using the 12 discrete P/D (= 1.125, 1.25, 1.5, 1.75, 2.0, 2.25, 2.5, 2.75, 3.0, 3.5, 4.0, and 4.5) mounting holes for the outer cylinder in the turntable. The turntable itself was incremented from $\alpha = -5°$ to 185° in increments of 1°. For small P/D and AR combinations resulting in hysteresis (described in Section 4.3.4), data were also collected by incrementing α in the opposite direction.

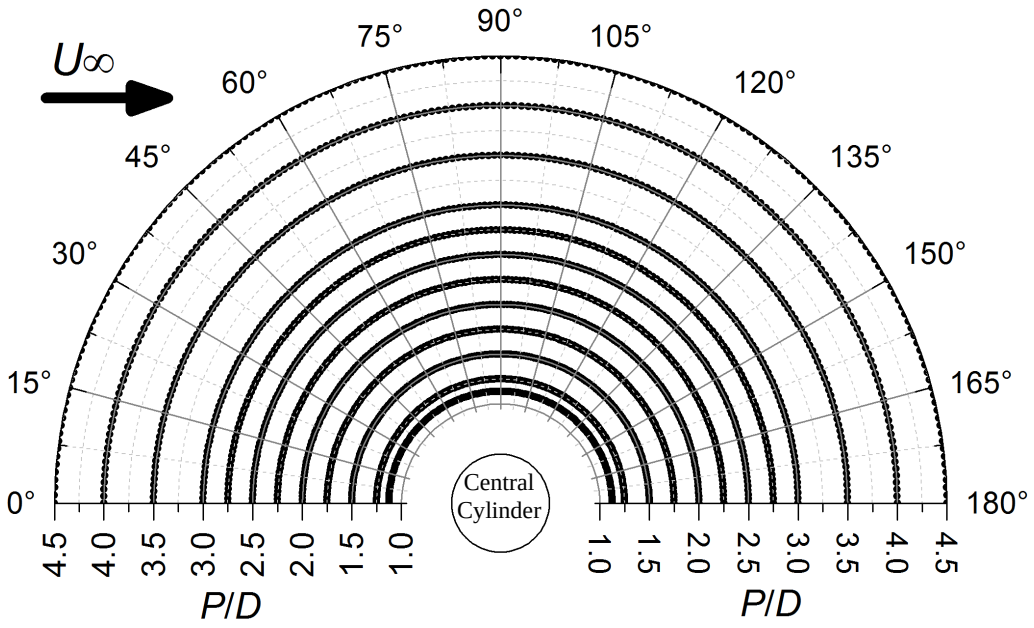

Figure A.1: Locations of the outer cylinder, for measurements of C_D and C_L for the central cylinder, with 12 discrete P/D and 1° increments in α. For $\alpha = 0°$ to 90°, the central cylinder represents a downstream cylinder. For $\alpha = 90°$ to 180°, the central cylinder represents an upstream cylinder. $P/D = 1.0$ represents the two cylinders touching.

The velocity fluctuation power spectra used to measure St were made at each of the points in Figure A.2. The P/D increments were the same as used for C_D and C_L, however each AR used a different increment of α in order to concentrate points where St was found to be more rapidly changing with P/D and α. With a stationary probe behind the central cylinder and a traversing probe behind the outer cylinder, simultaneous power spectra measurements from α = 0° to 90° covered the entire range. As described above, P/D and AR combinations resulting in hysteresis were also conducted in the CCW direction (with a decreasing value of α).

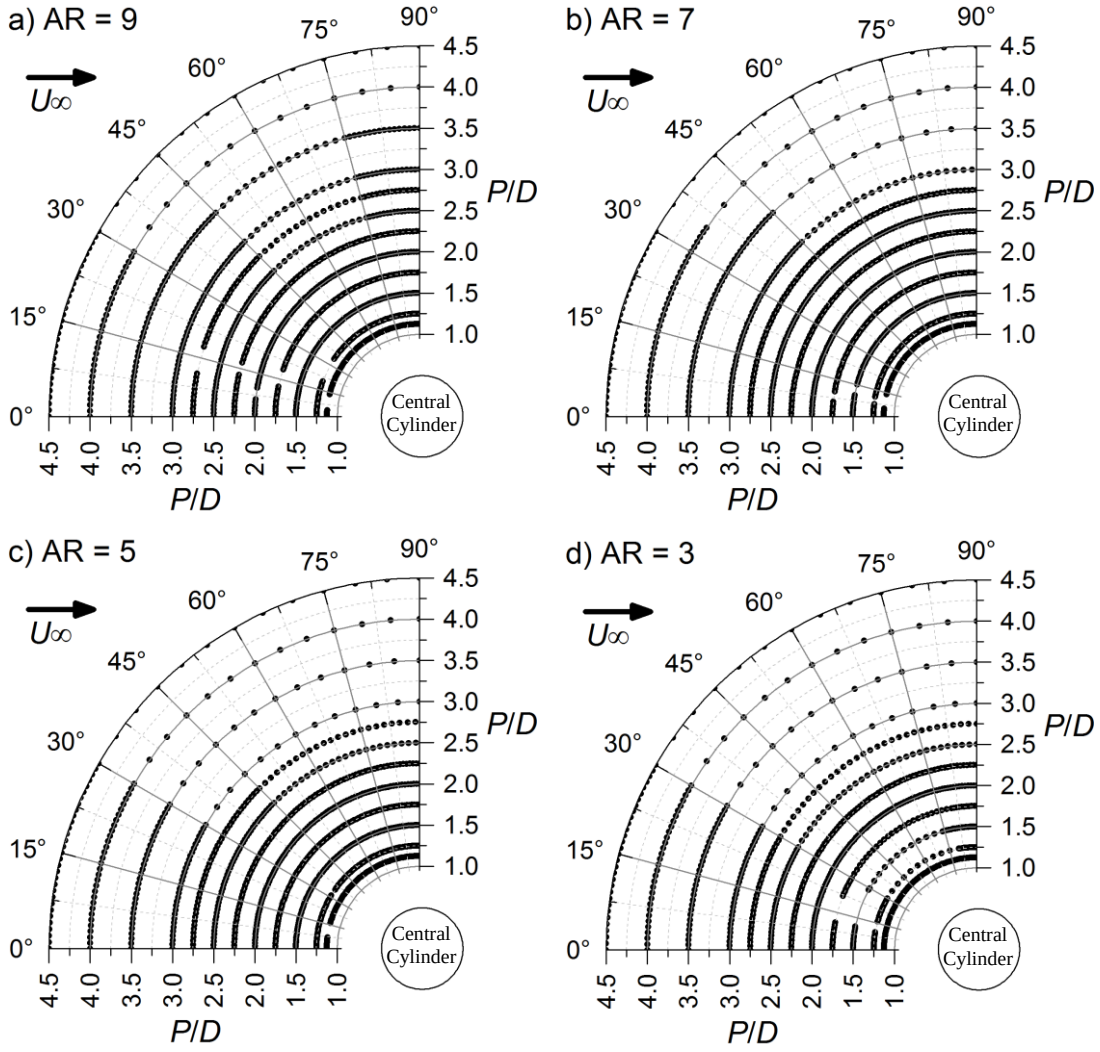

Figure A.2: Data collection points for St with 12 discrete P/D, α increments of 1°, 2° or 5°, for a) AR = 9, b) AR = 7, c) AR = 5, and d) AR = 3. Data were collected at x/D = 3.0, y/D = 1.0, and z/H = 0.5 for both the central (downstream) and the outer (upstream) cylinders simultaneously. P/D = 1.0 represents the two cylinders touching. Flow from left to right.

Appendix B Mean Coefficient of Drag, Mean Coefficient of Lift, and Strouhal Number Data as Functions of Pitch Ratio and Aspect Ratio

This Appendix shows the mean coefficient of drag, C_D, mean coefficient of lift, C_L, and Strouhal number, St, data as functions of pitch ratio, P/D, aspect ratio, AR, and incidence angle, α. All of the data were obtained at Re = 6.5×10^4 with δ/D = 1.4. For a map of the P/D and α configurations used for each AR to measure C_D, C_L, and St, see Appendix A. The Strouhal number data were obtained at the mid-height position.

All figures in this Appendix (Figure B.1 to Figure B.12) follow the same general layout. The left side of each figure shows the upstream cylinder data while the right side of each figure shows the downstream cylinder data. The top pair of graphs show C_D data, the middle pair of graphs show C_L data, and the bottom pair of graphs show St data. Each graph contains the data for AR = 9 (■/□), AR = 7 (●/○), AR = 5 (▲/△), and AR = 3 (▼/▽). For closely spaced staggered cylinders at high AR, hysteresis was found in the C_D and C_L measurements with respect to whether α was increasing or decreasing as described in detail in Section 4.3.4. For configurations resulting in hysteresis, tests conducted with both increasing (solid symbols) and decreasing (open symbols) α are shown.

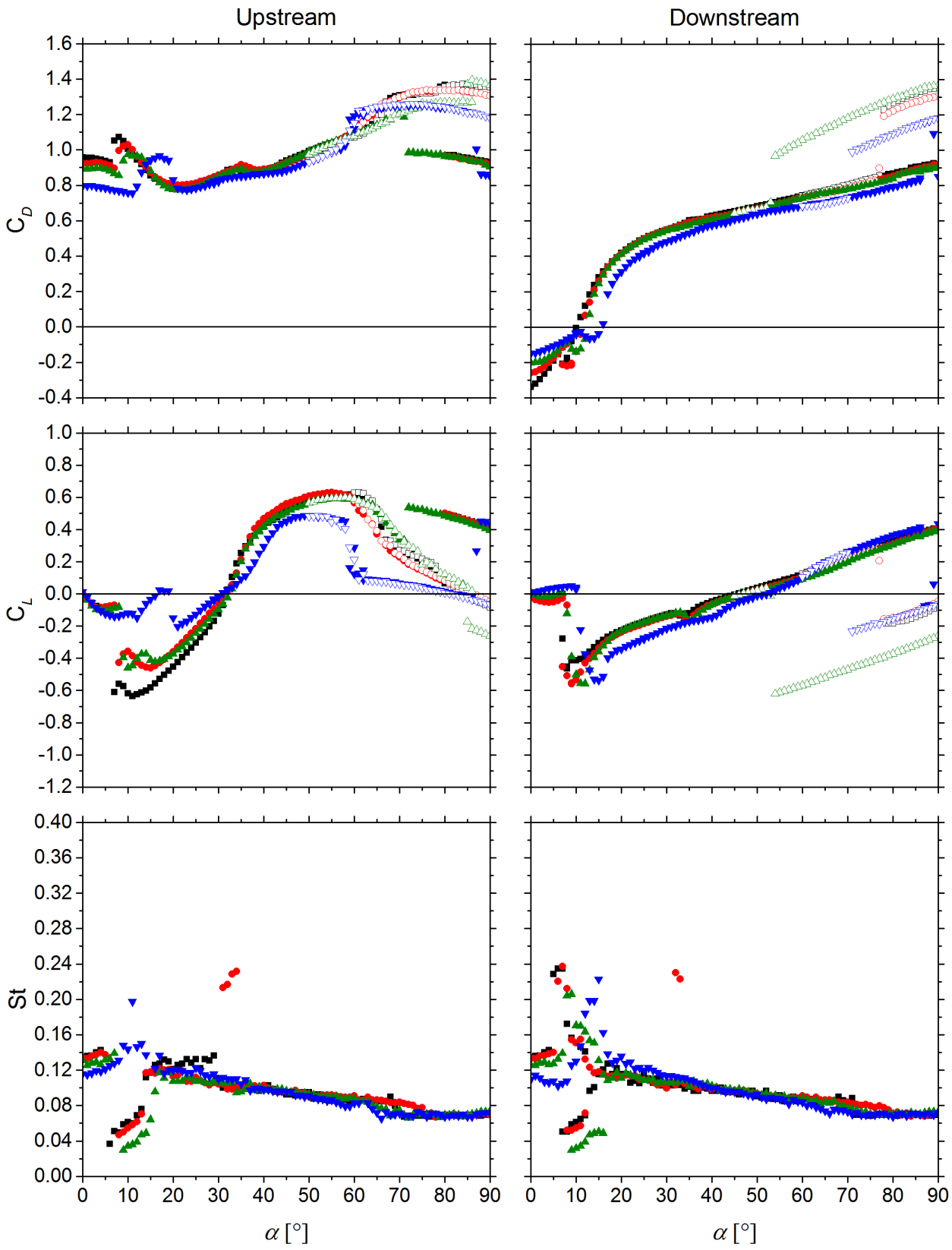

Figure B.1: P/D = 1.125 data for C_L, C_D, and St.

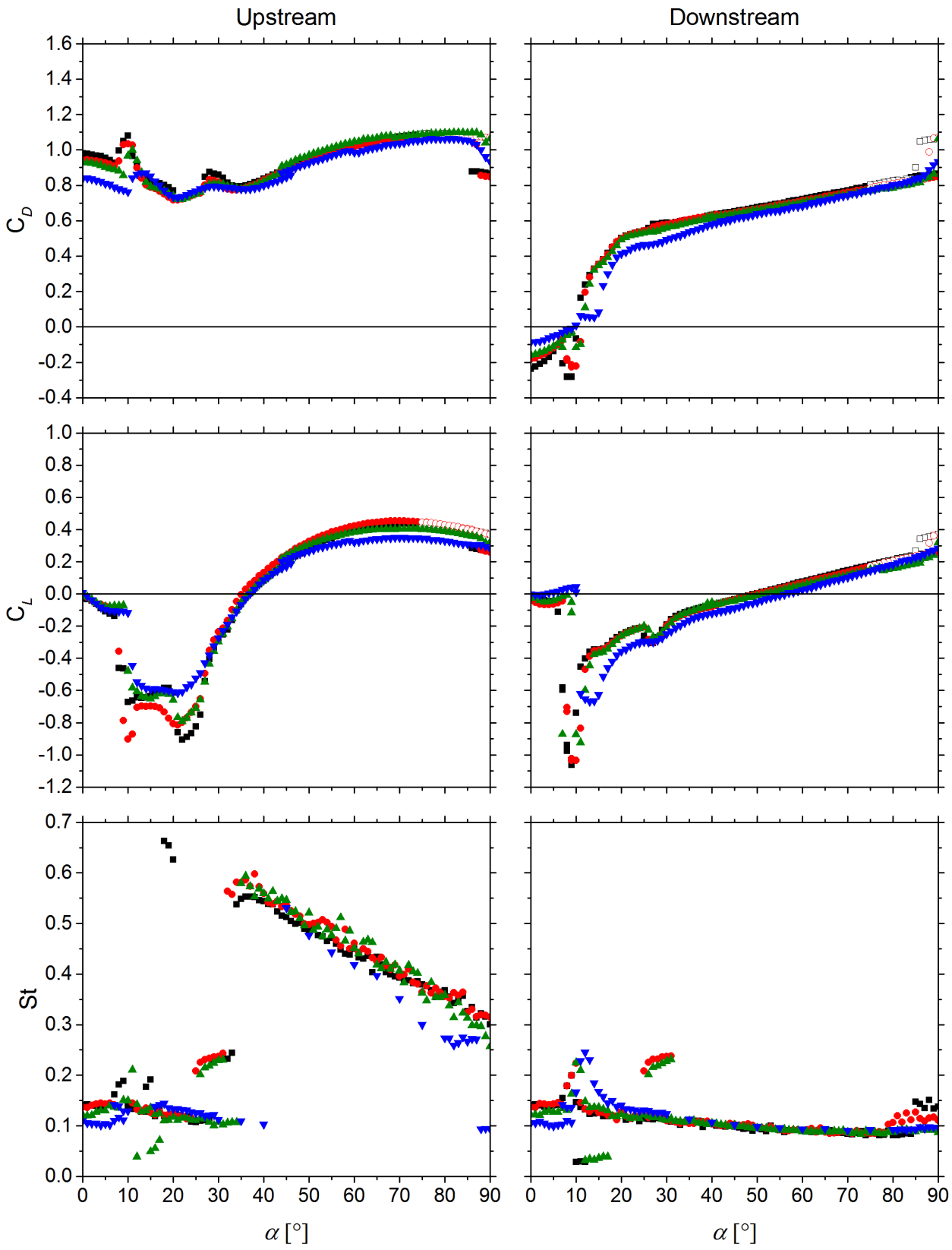

Figure B.2: P/D = 1.25 data for C_L, C_D, and St.

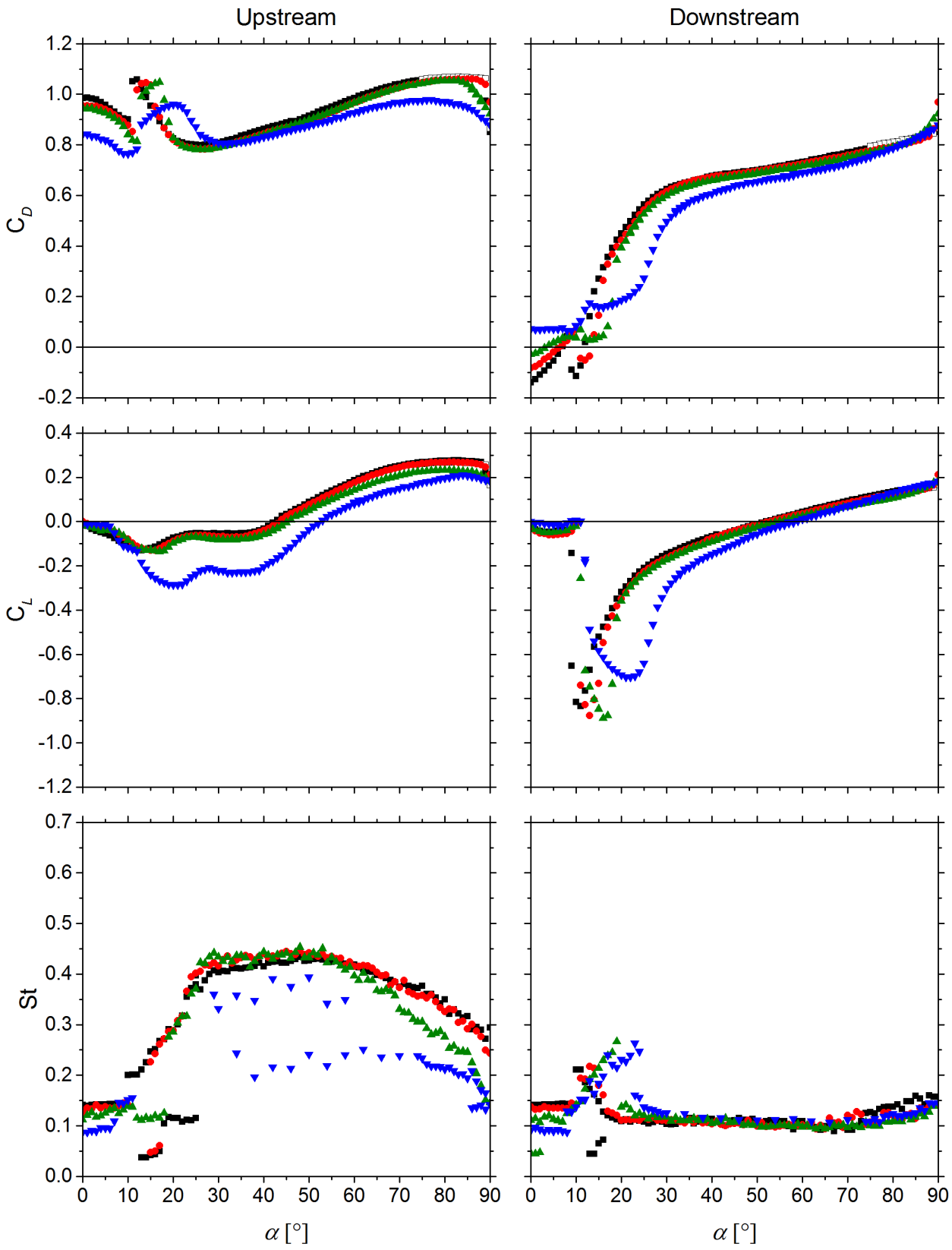

Figure B.3: P/D = 1.5 data for C_L, C_D, and St.

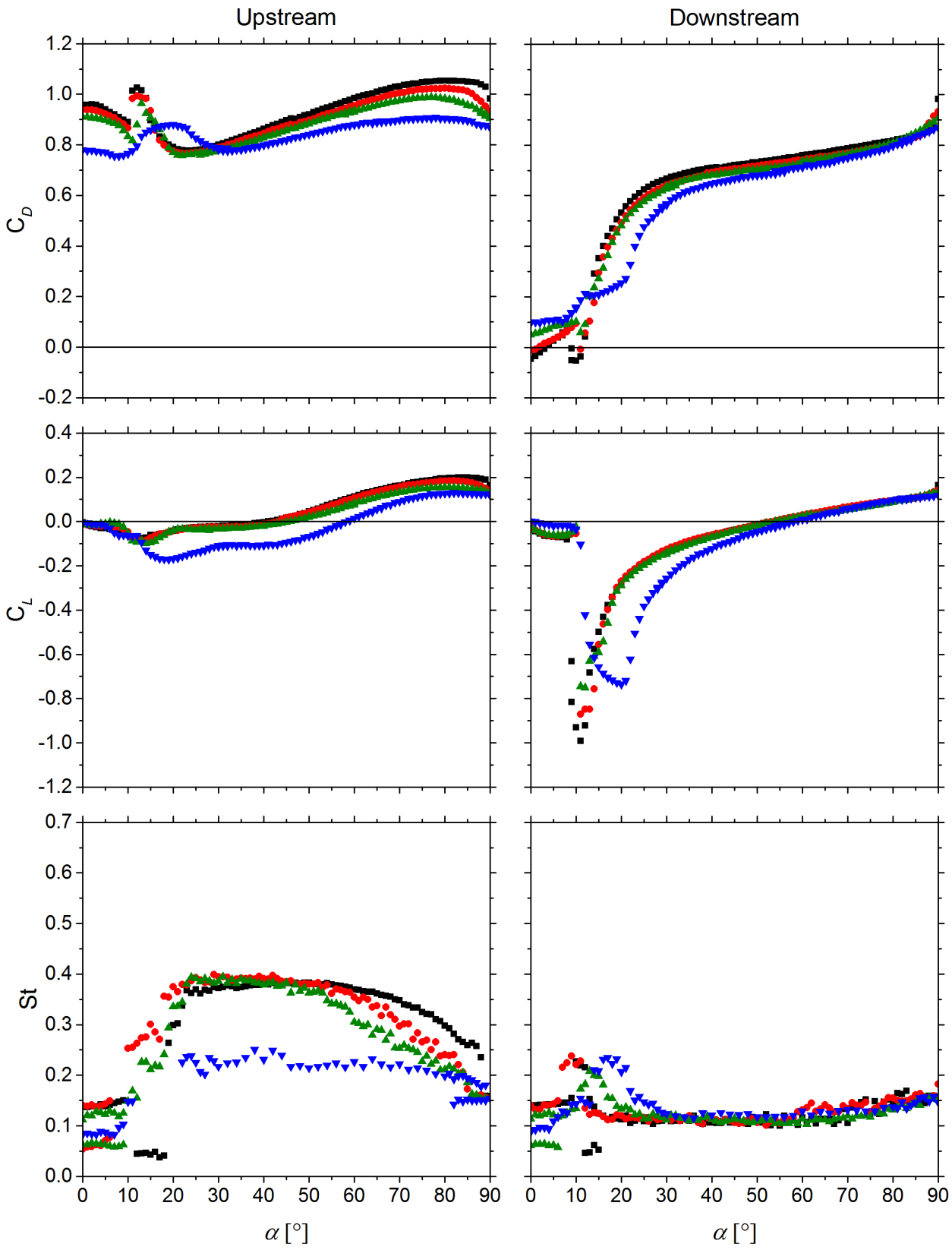

Figure B.4: P/D = 1.75 data for C_L, C_D, and St.

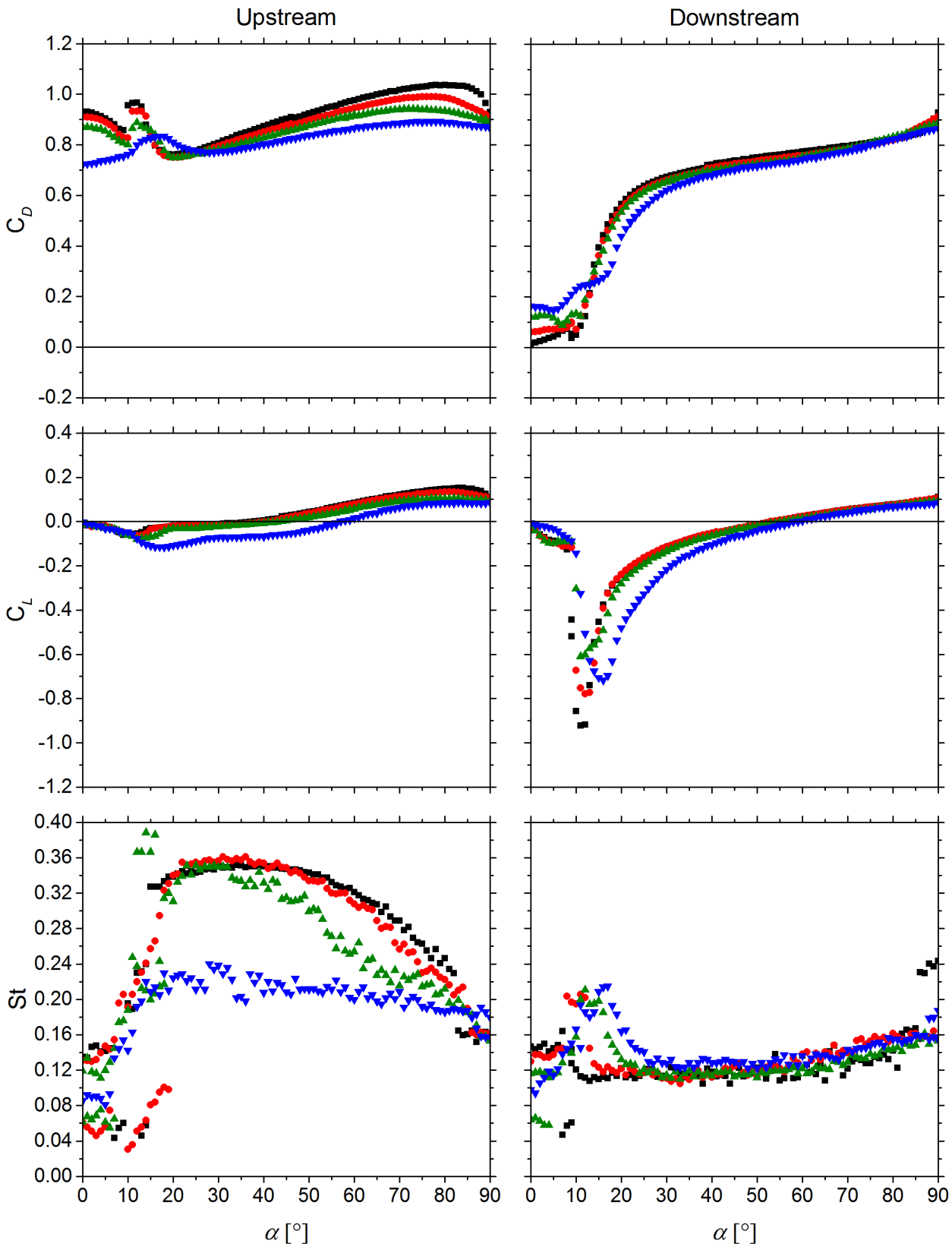

Figure B.5: P/D = 2.0 data for C_L, C_D, and St.

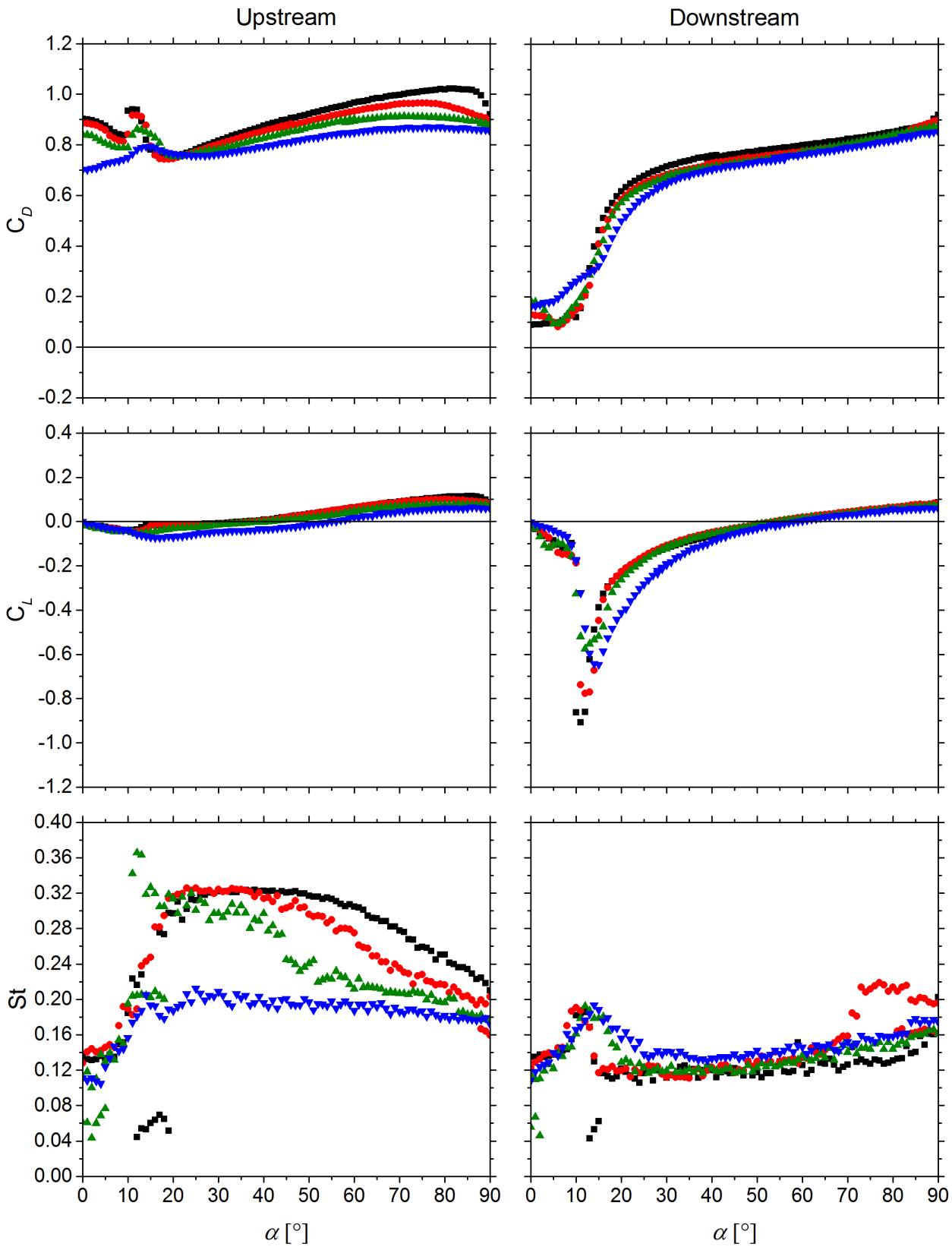

Figure B.6: P/D = 2.25 data for C_L, C_D, and St.

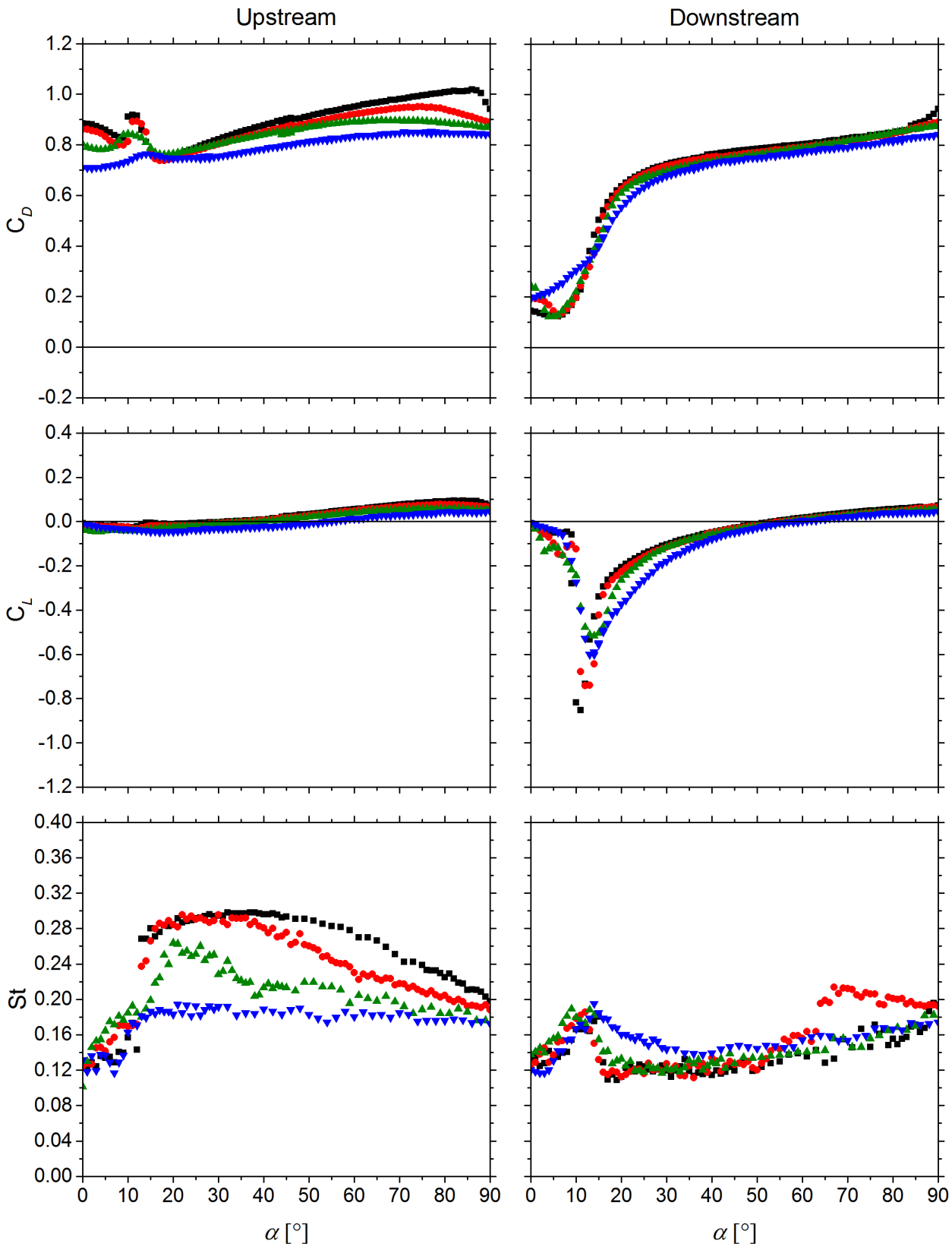

Figure B.7: P/D = 2.5 data for C_L, C_D, and St.

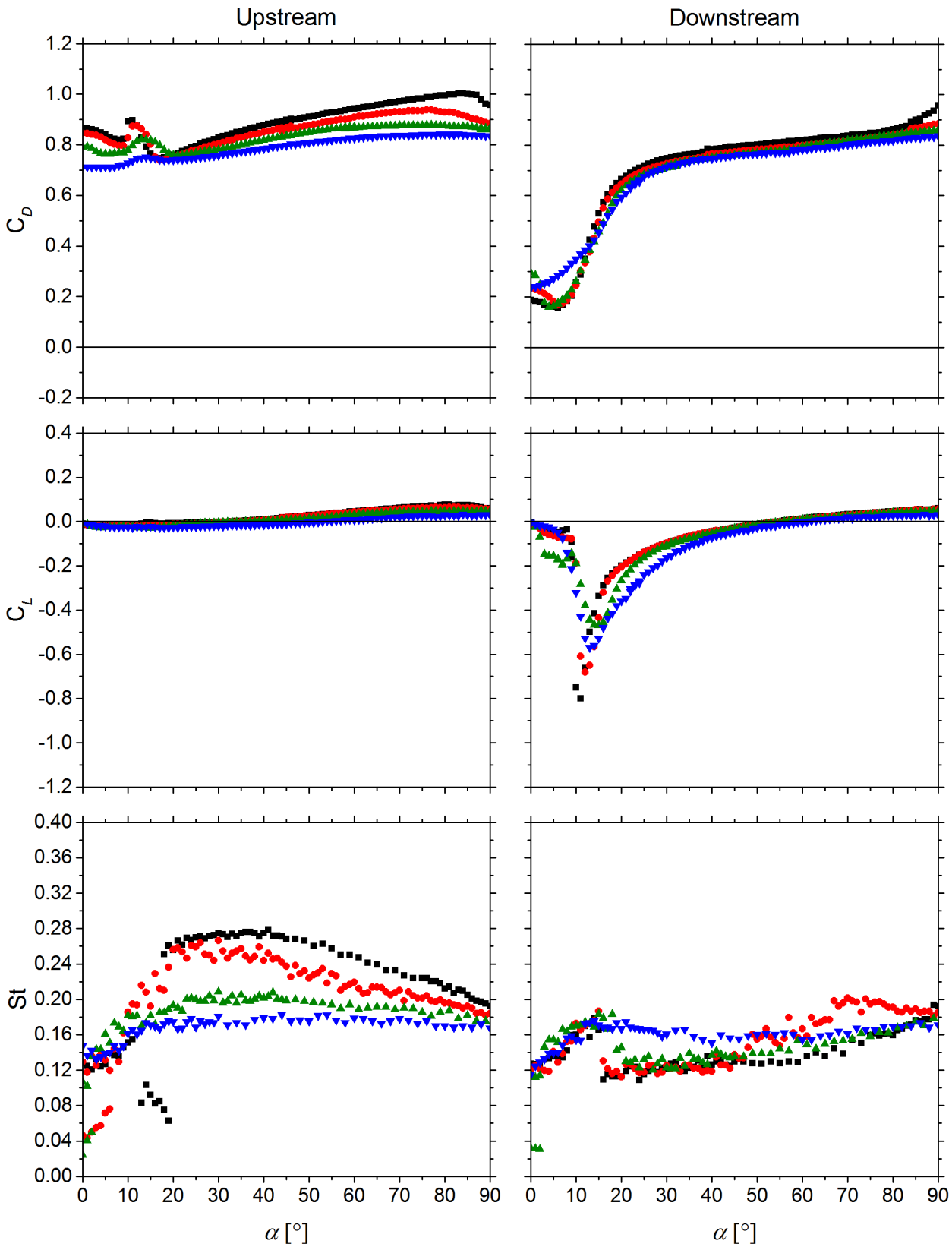

Figure B.8: P/D = 2.75 data for C_L, C_D, and St.

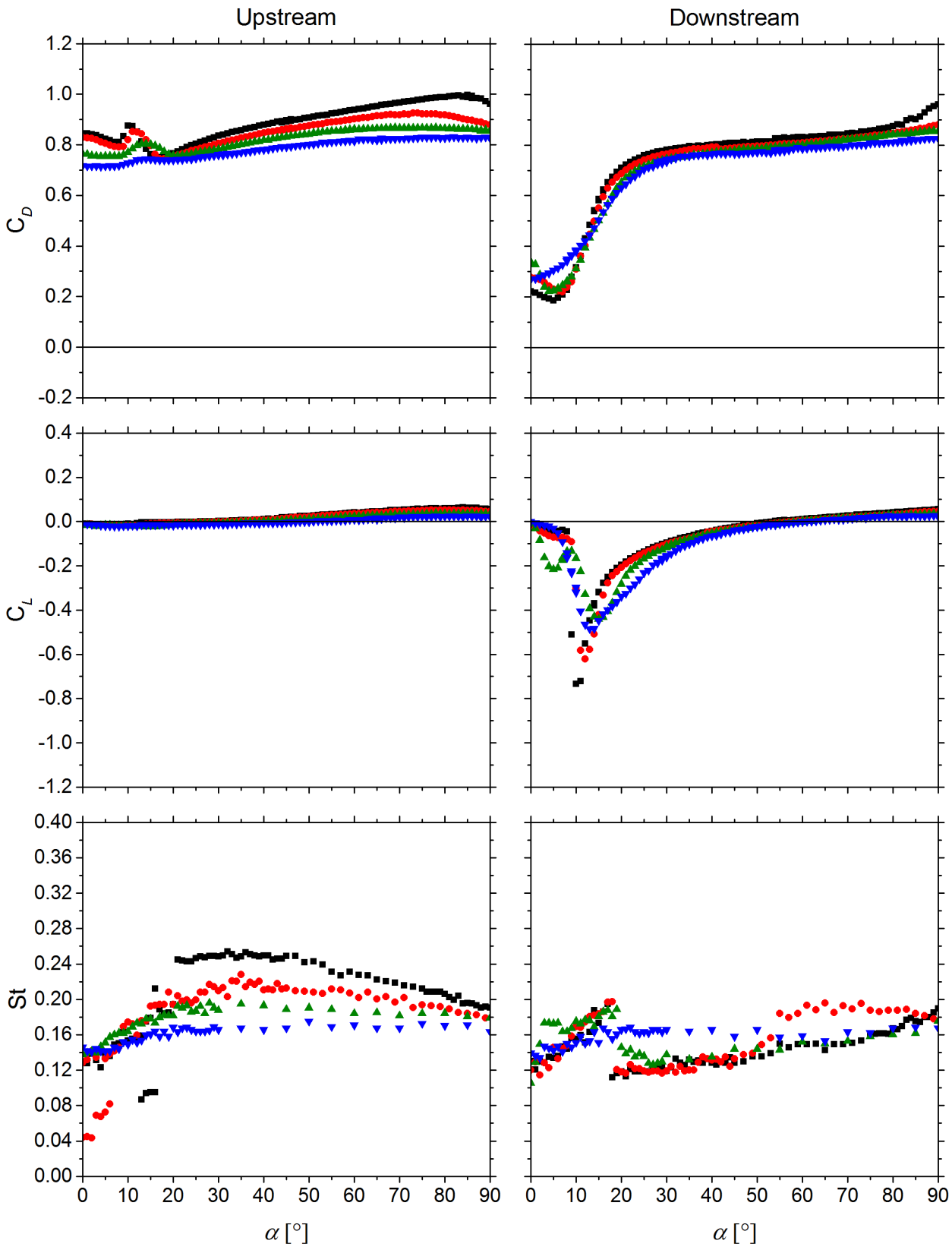

Figure B.9: P/D = 3.0 data for C_L, C_D, and St.

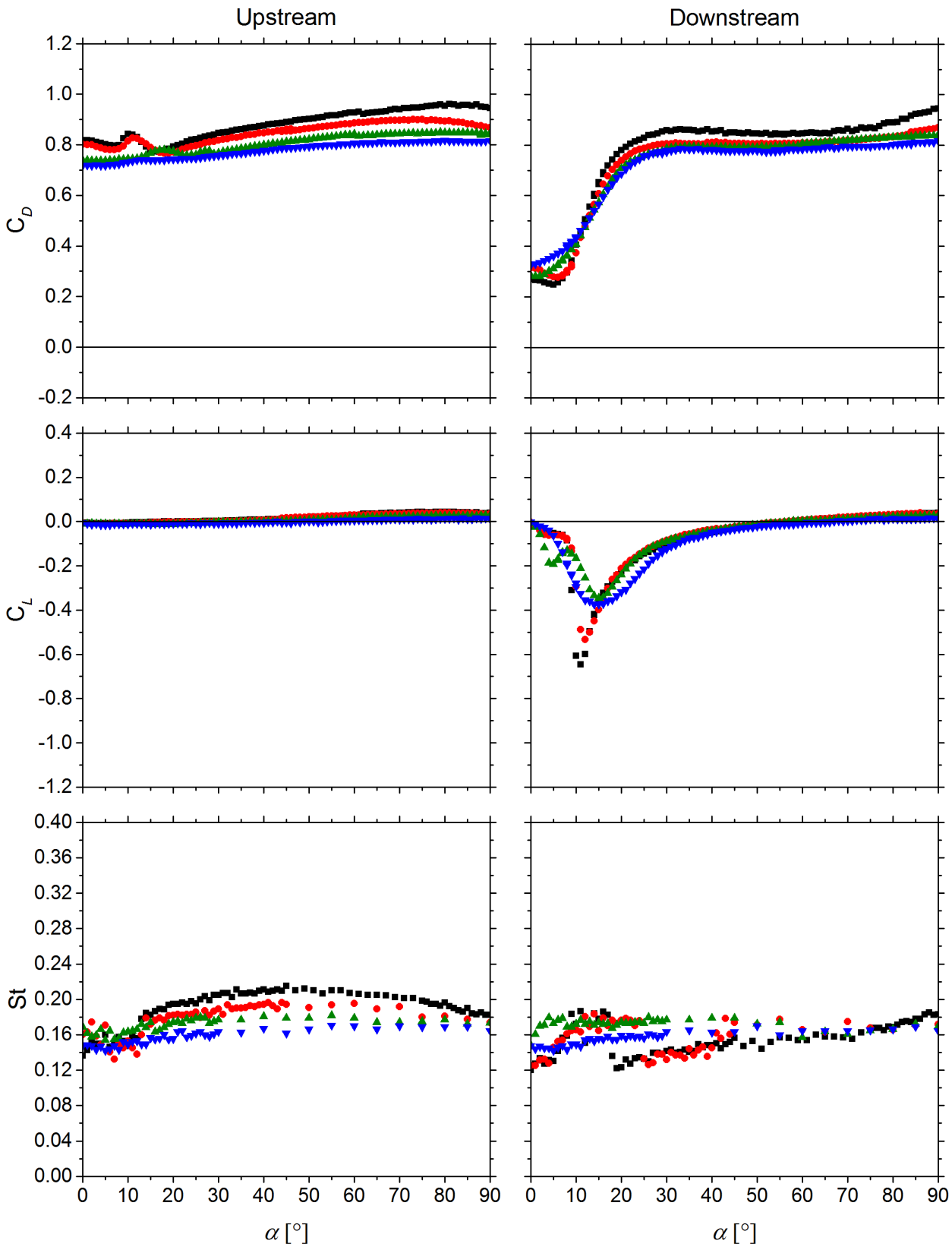

Figure B.10: P/D = 3.5 data for C_L, C_D, and St.

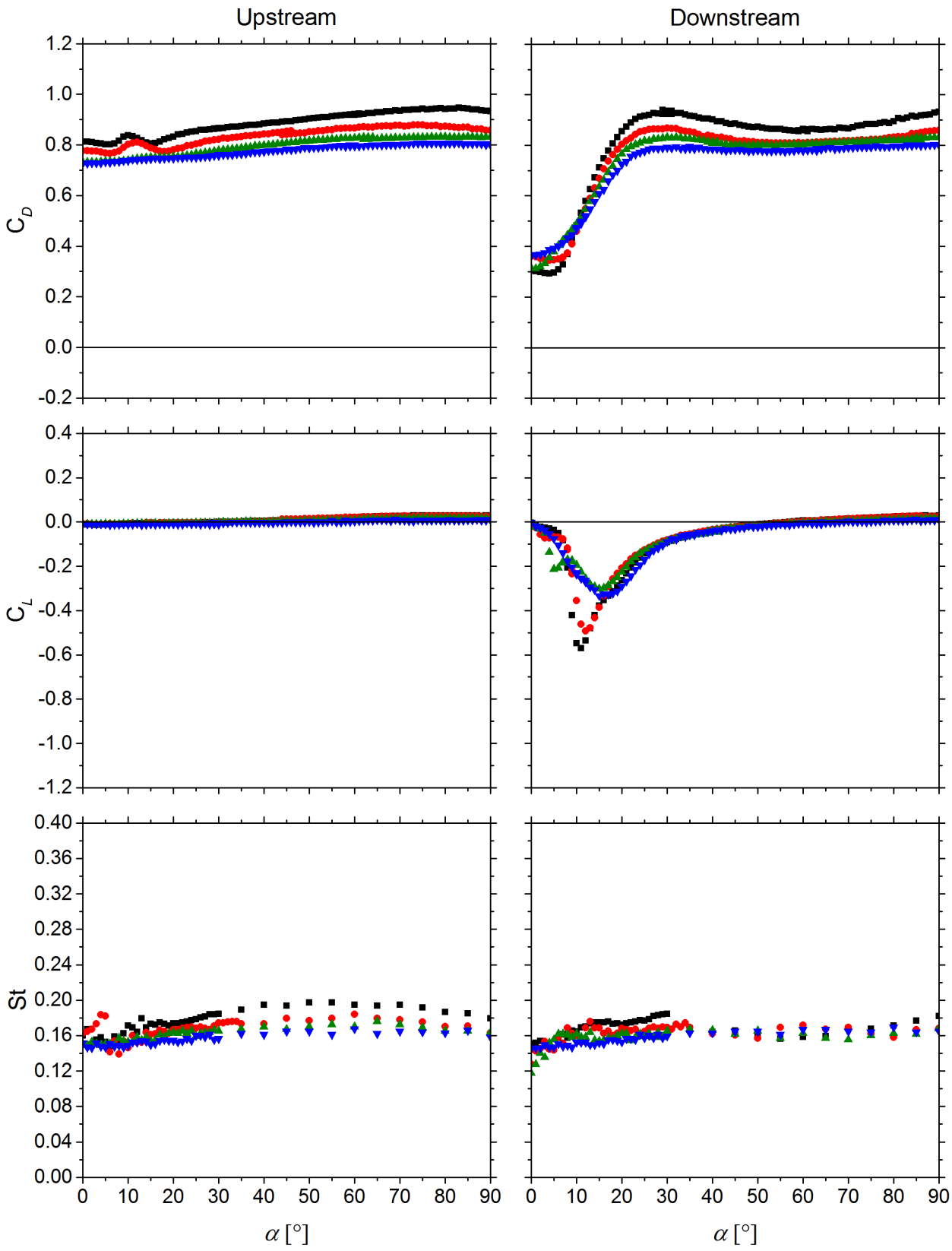

Figure B.11: P/D = 4.0 data for C_L, C_D, and St.

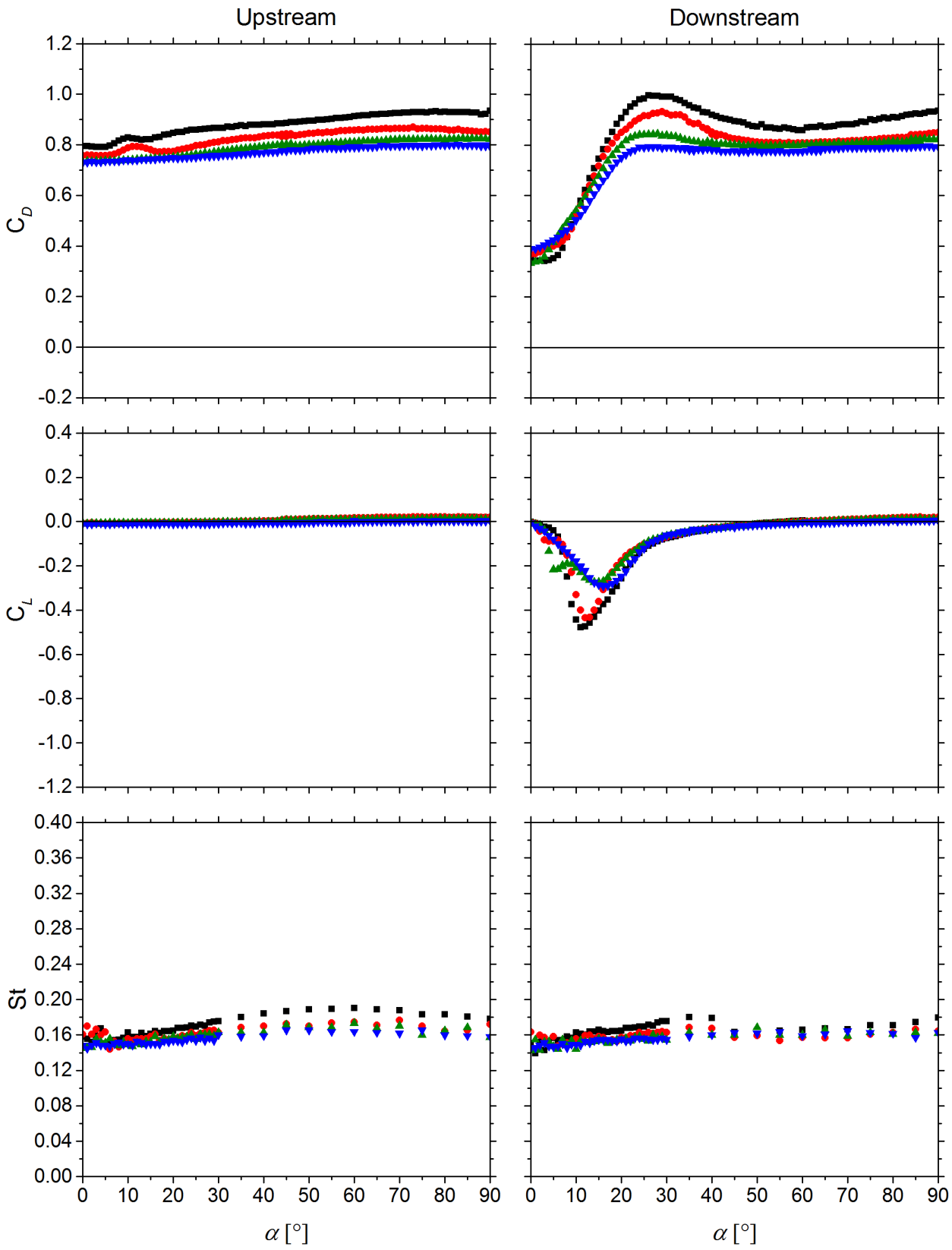

Figure B.12: P/D = 4.5 data for C_L, C_D, and St.

Appendix C Intermittent Gap Bias Switching for Moderately Spaced Surface-Mounted Finite-Height Cylinders in a Side-by-Side Configuration

Two cylinders in a side-by-side configuration at moderate pitch ratios (P/D = 1.5 to 3.0, although this range is dependent on Re) exhibit deflected gap flow, biased towards one of the cylinders. The biased flow regime produces leads to different wakes, wind loading, and vortex shedding frequencies for the two cylinders. As the cylinders are geometrically symmetric, it is equally likely that the gap flow may bias to either cylinder and may switch between the two intermittently. The lower the value of P/D, the more stable the gap flow becomes, allowing the deflected flow to remain biased towards one cylinder for a longer period of time (or perhaps permanently biased). Conversely, at higher P/D the reduced proximity interference reduces the gap deflection angle and its ability to maintain a preferred direction. At a critical P/D (that is a function of AR and Re) the cylinders no longer exhibit a deflected gap flow, the asymmetry in the flow disappears, and two identical parallel vortex streets are formed.

Force balance measurements represented an average of 10,000 instantaneous samples over 10 seconds. The time duration of the wake state was likely less than the sample time, resulting in an average of the two wake states effectively being measured for moderate P/D at α = 90°. For P/D that did could not maintain a single preferential gap deflection for the entire 10-second sampling time, the direction of the gap bias was manually influenced in order to approximate C_D for both discrete wake states throughout the intermittent bias switching range of P/D. By using the data at α = 90° ± 5° (at α = 85° and 95° to obtain both gap bias directions), the gap bias was found to be deflected to one cylinder for the majority of the 10-second sample time while still maintaining a geometry very close to the side-by-side-configuration. Using this information the two wake states could be approximated from the averaged data at α = 90°; if the difference in the two C_D values was greater than 5 %, the P/D was considered to fall within the biased flow regime. Following this criterion, the boundary between the biased and co-shedding flow regimes for AR = 9, 7, 5, and 3 was found at critical pitch ratios of P/D = 3.0, 2.75, 2.25, and 2.0, respectively (Table 4.1). Figure C.1 and Figure C.2 show the C_D and C_L values at α = 85° and 95° to further exemplify the difference in wind loading between the two wake states. Figure C.3 shows all power spectra peaks between α = 85° and 90° for both hot-wire probes to show the intermittent wake state switching caught over the biased flow regime range.

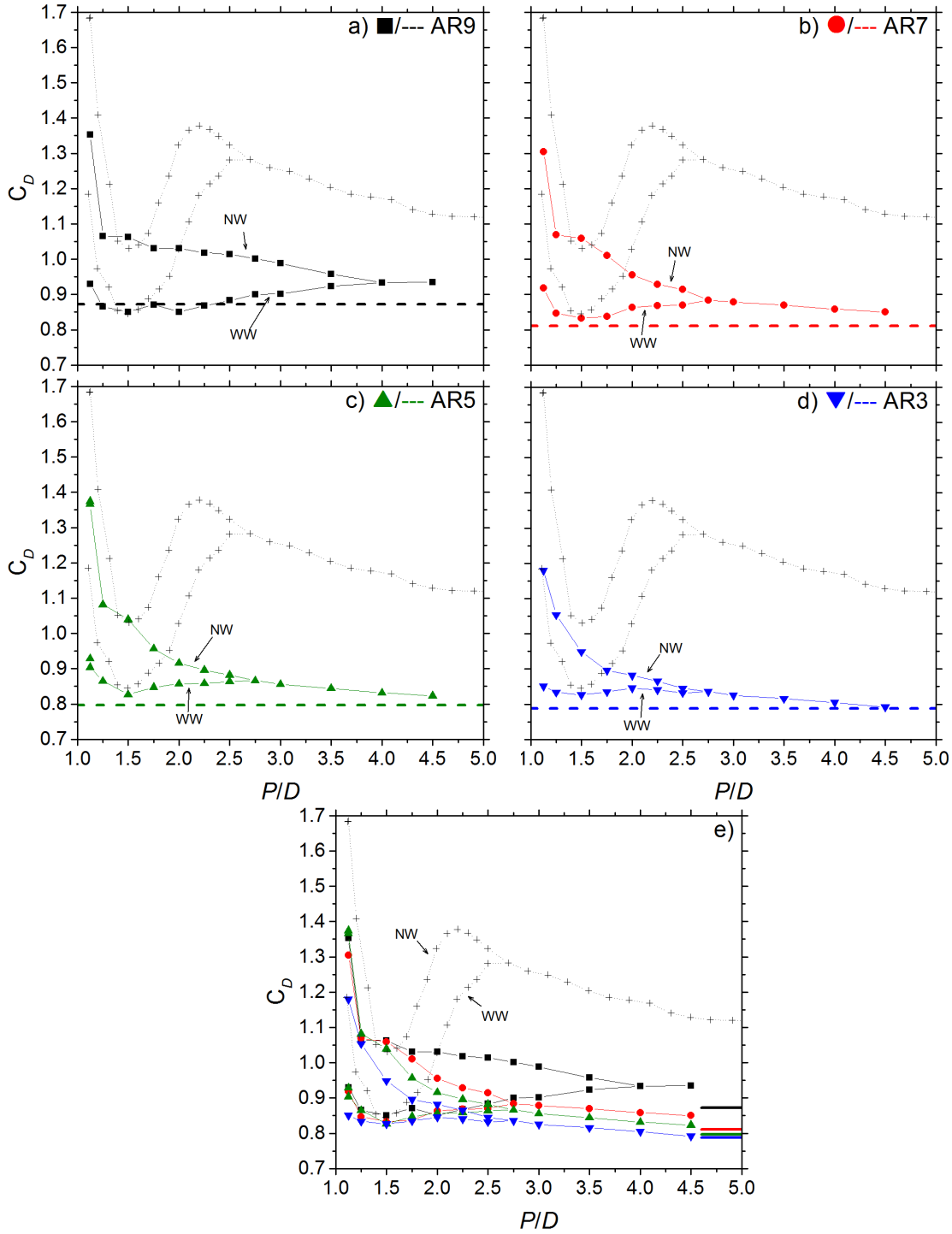

Figure C.1: Mean drag coefficient, C_D, data for side-by-side finite-height (solid symbols), isolated finite-height (dashed line), and infinite (+ data from Alam et al., 2003a) cylinders as function of P/D and a) AR: ■/– AR = 9, b) ●/– AR = 7, c) ▲/– AR = 5, d) ▼/– AR = 3, and e) all data combined. Data taken from α = 85° and 95°. High C_D is narrow wake state (NW); low C_D is wide wake state (WW).

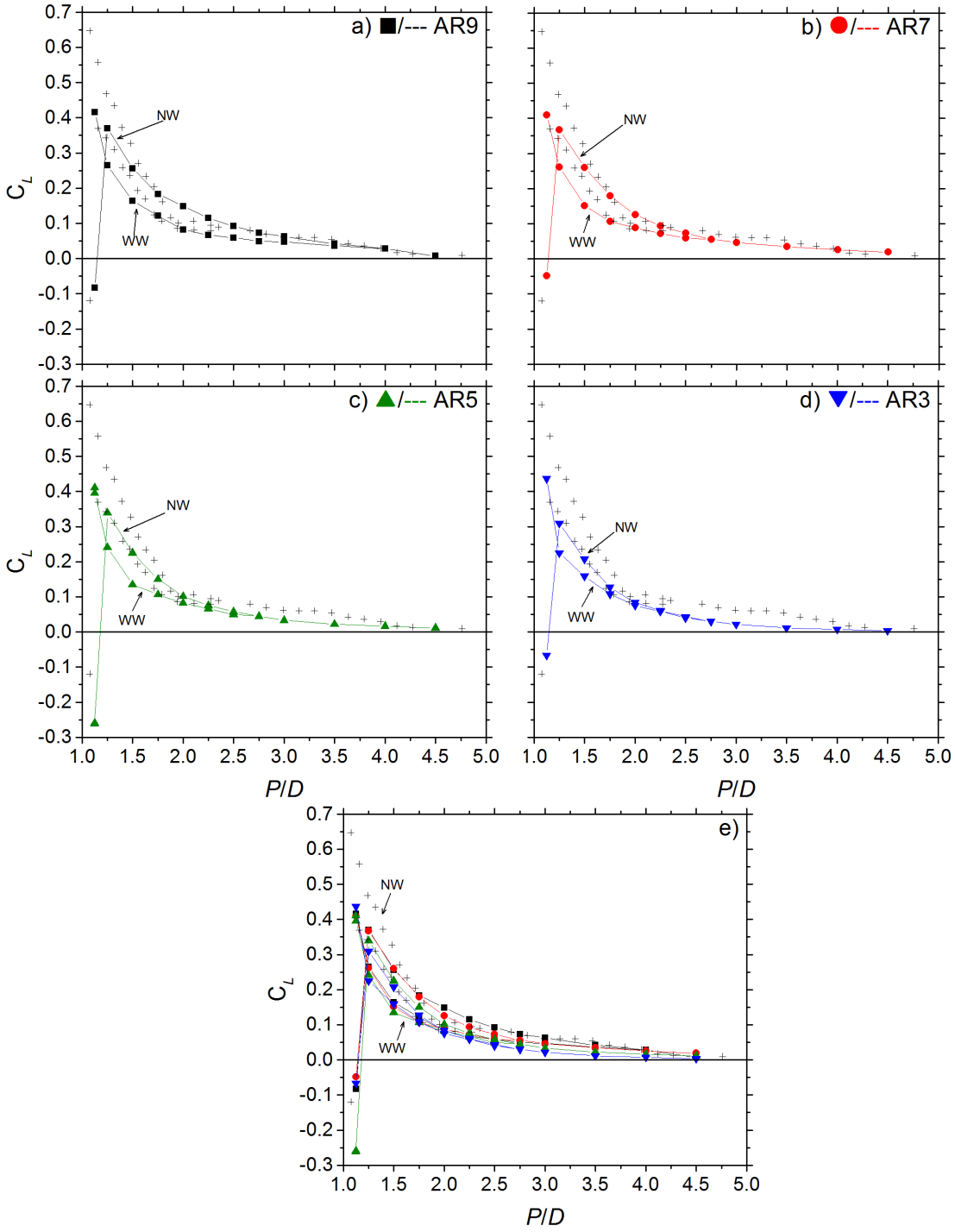

Figure C.2: Mean lift coefficient, C_L, data for side-by-side finite-height (solid symbols), isolated finite-height (dashed line), and infinite (+ data from Alam et al., 2003a) cylinders as function of P/D and AR: a) ■/– AR = 9, b) ●/– AR = 7, c) ▲/– AR = 5, d) ▼/– AR = 3, and e) all data combined. Data taken from α = 85° and 95°. For $P/D \geq 1.25$, high C_L is narrow wake state (NW); low C_L is wide wake state (WW).

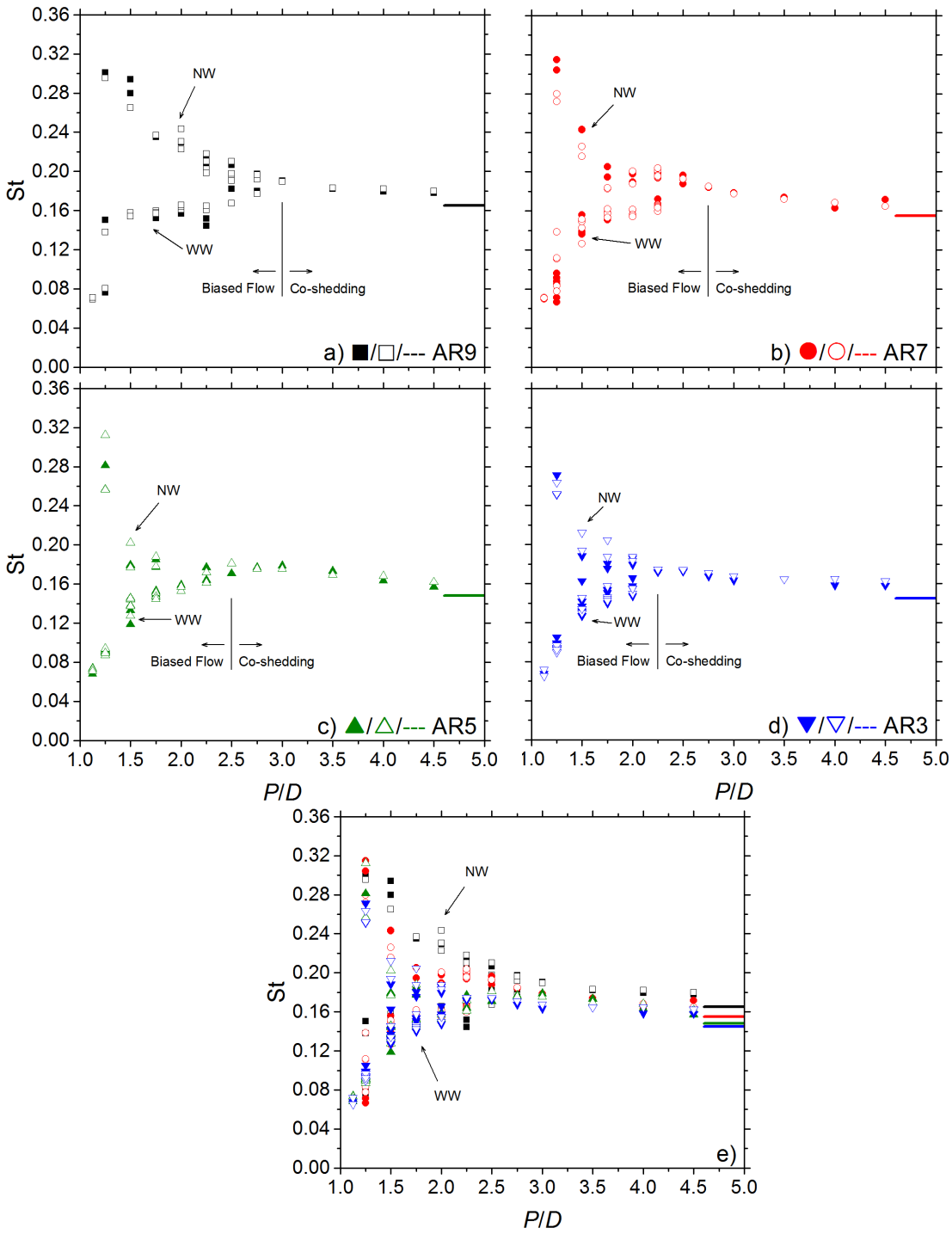

Figure C.3: Side-by-side configuration mid-span Strouhal number, St, data as a function of *P*/*D* and AR measured by the traversing (solid symbols) and stationary hot-wire probe (open symbols) with isolated cylinder (dashed line) as reference. a) ■/□/– AR = 9, b) ●/○/– AR = 7, c) ▲/△/– AR = 5, d) ▼/▽/– AR = 3, and e) all data combined. Data taken between α = 85° and 90° from both probes to show bias switching behaviour. High St is narrow wake state (NW); low St is wide wake state (WW).

Appendix D Discussion of Alam et al. (2003a) Narrow and Wide Wake State Designations for Side-by-Side Cylinders

This Appendix discusses the narrow wake state and wide wake state designations offered by Alam et al. (2003a), with a focus on the interpretation with regard to the mean lift coefficient, C_L. In the article the authors describe (at a given P/D) the narrow wake state (mode NW) as having a universally *higher* C_D and St than the wide wake state (mode WW). The narrow wake state (mode NW) was also associated with a *lower* C_L than the wide wake state (mode WW) as shown in Figure D.1. Additionally, time-averaged pressure coefficient, C_P, data as a function of circumferential angle was presented for cylinders at P/D = 1.5 (Figure D.2; Alam et al., 2003a) and P/D = 1.2 (Figure D.3; Alam and Zhou, 2007).

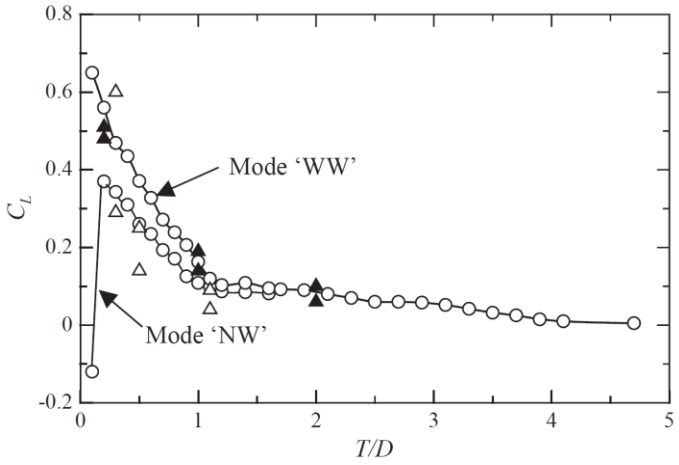

Figure D.1: Lift coefficient, C_L, and corresponding wake stated designations offered by a) Alam et al. (2003a) (figure taken from Alam et al. (2003a)).

The finite cylinder data from this thesis and the infinite cylinder data from Sumner et al. (2005) show that high values of C_D and St also correspond to a high value of C_L within the biased flow regime. This contradicts the finding of Alam et al. (2003a), which showed the opposite tendency for C_L. The C_P data for P/D = 1.5 and 1.2 were digitized and integrated for both the narrow wake and wide wake designations given in the original pressure data figures (Figure D.2 and Figure D.3, respectively) using the following equation.

$$C_L = -0.5 \int_0^{2\pi} C_P sin(\theta) d\theta \quad \text{(D.1)}$$

It was found for both P/D = 1.5 and 1.2 that the narrow wake state produced the *higher* magnitude of C_L with integrated pressure data where the wide wake state produces the *lower* magnitude of C_L as summarized in Table D.1. This would indicate that for the biased flow regime found at $P/D \geq 1.15$ the "Mode 'NW'" and "Mode 'WW'" designations given in Figure D.1 should be reversed.

Table D.1: Comparison of narrow and wide wake state C_L using directly measured values and integrated pressure distribution values. All data taken from Alam et al. (2003a) and Alam and Zhou (2007).

	Direct C_L (Figure D.1)		C_P Integration (Figure D.2 and Figure D.3)	
Wake State Designation from Original Graph	Narrow	Wide	Narrow	Wide
P/D = 1.5 (Alam et al., 2003a)	0.236	0.327	0.432	0.305
P/D = 1.2 (Alam and Zhou, 2007)	0.343	0.468	0.590	0.379

When using the designations for C_L as defined by the C_P data, the biased flow regime ($P/D \geq 1.15$) exhibits a narrow wake state characterized by a *higher* C_D, C_L, and St and a wide wake state characterized by a *lower* C_D, C_L, and St. With new designations, the data for both the narrow wake state and wide wake state across all P/D in the context of C_D, C_L, and St would all align with the present data and the data from Sumner et al. (2005).

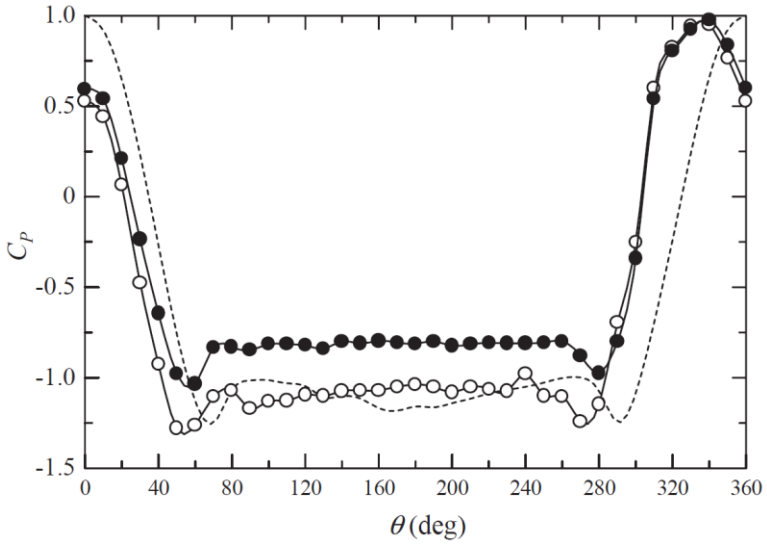

Figure D.2: Time-averaged pressure coefficient, C_P, data for wide wake (solid symbols) and narrow wake (open symbols) states for side-by-side infinite cylinders at P/D = 1.5. Isolated cylinder (dashed line) for reference. Figure taken from Alam et al. (2003a).

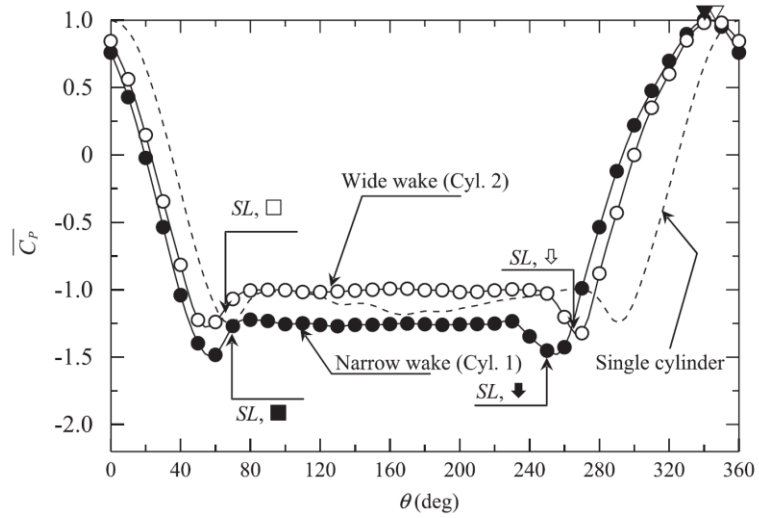

Figure D.3: Time-averaged pressure coefficient data for wide wake (open symbols) and narrow wake (solid symbols) states for side-by-side infinite cylinders at P/D = 1.2. Isolated cylinder (dashed line) for reference. Figure taken from Alam and Zhou (2007).

Appendix E Hysteresis for AR = 7 and AR = 5

The following Appendix provides the data for the hysteresis in wind loading found at low P/D near $\alpha = 90°$. Behaviour as a function of P/D for AR = 7 may be found in Figure E.1a, and AR = 5 in Figure E.1b below. In depth discussion on this phenomenon may be found in Section 4.3.4, and similar curves for AR = 9 and AR = 3 may be found in Figure 4.9. For the effect of AR on hysteretic behaviour at P/D = 1.125 and 1.25, see Figure 4.10.

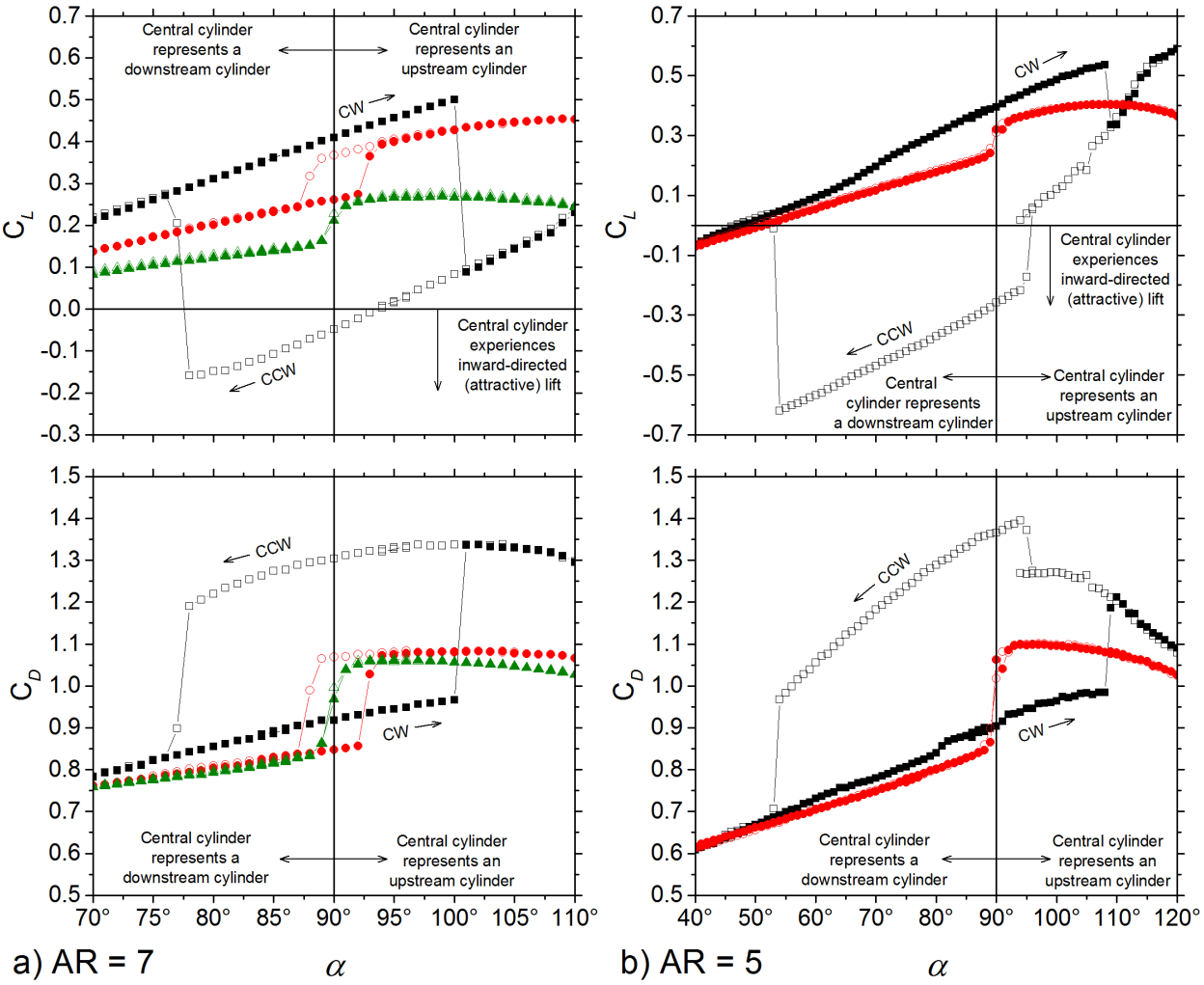

Figure E.1: C_D and C_L data for the central cylinder for a) AR = 7 and b) AR = 5. Solid symbols: CW movement of the outer cylinder. Open symbols: CCW movement of the outer cylinder. ■, □: P/D = 1.125; ●,○: P/D = 1.25; ▲,△: P/D = 1.5.

Appendix F Permission of Use Agreements

This appendix contains the permission of use documentation for figures used in this thesis.

ELSEVIER LICENSE TERMS AND CONDITIONS	
	Aug 30, 2018
This Agreement between University of Saskatchewan -- Hayden Reitenbach ("You") and Elsevier ("Elsevier") consists of your license details and the terms and conditions provided by Elsevier and Copyright Clearance Center.	
License Number	4418960491486
License date	Aug 30, 2018
Licensed Content Publisher	Elsevier
Licensed Content Publication	Journal of Fluids and Structures
Licensed Content Title	Aerodynamic characteristics of two side-by-side circular cylinders and application of wavelet analysis on the switching phenomenon
Licensed Content Author	Md. Mahbub Alam,M. Moriya,H. Sakamoto
Licensed Content Date	September–October 2003
Licensed Content Volume	18
Licensed Content Issue	3-4
Licensed Content Pages	22
Start Page	325
End Page	346
Type of Use	reuse in a thesis/dissertation
Intended publisher of new work	other
Portion	figures/tables/illustrations
Number of figures/tables/illustrations	2
Format	both print and electronic
Are you the author of this Elsevier article?	No
Will you be translating?	No
Original figure numbers	Figure 7 and Figure 10
Title of your thesis/dissertation	FINITE EFFECTS ON TWO STAGGERED CYLINDERS IN A CROSS-FLOW
Expected completion date	Sep 2018
Estimated size (number of pages)	150
Requestor Location	University of Saskatchewan 69 Campus Drive Saskatoon, SK S7N 5B1 Canada Attn: University of Saskatchewan
Publisher Tax ID	GB 494 6272 12

ELSEVIER LICENSE
TERMS AND CONDITIONS

Aug 30, 2018

This Agreement between University of Saskatchewan -- Hayden Reitenbach ("You") and Elsevier ("Elsevier") consists of your license details and the terms and conditions provided by Elsevier and Copyright Clearance Center.

License Number	4418960591898
License date	Aug 30, 2018
Licensed Content Publisher	Elsevier
Licensed Content Publication	Journal of Fluids and Structures
Licensed Content Title	Flow around two side-by-side closely spaced circular cylinders
Licensed Content Author	Md. Mahbub Alam,Y. Zhou
Licensed Content Date	Jul 1, 2007
Licensed Content Volume	23
Licensed Content Issue	5
Licensed Content Pages	7
Start Page	799
End Page	805
Type of Use	reuse in a thesis/dissertation
Intended publisher of new work	other
Portion	figures/tables/illustrations
Number of figures/tables/illustrations	2
Format	both print and electronic
Are you the author of this Elsevier article?	No
Will you be translating?	No
Original figure numbers	Figure 1 and Figure 2
Title of your thesis/dissertation	FINITE EFFECTS ON TWO STAGGERED CYLINDERS IN A CROSS-FLOW
Expected completion date	Sep 2018
Estimated size (number of pages)	150
Requestor Location	University of Saskatchewan 69 Campus Drive Saskatoon, SK S7N 5B1 Canada Attn: University of Saskatchewan
Publisher Tax ID	GB 494 6272 12

ELSEVIER LICENSE
TERMS AND CONDITIONS

Aug 30, 2018

This Agreement between University of Saskatchewan -- Hayden Reitenbach ("You") and Elsevier ("Elsevier") consists of your license details and the terms and conditions provided by Elsevier and Copyright Clearance Center.

License Number	4418960381515
License date	Aug 30, 2018
Licensed Content Publisher	Elsevier
Licensed Content Publication	Journal of Fluids and Structures
Licensed Content Title	A review of flow-induced noise from finite wall-mounted cylinders
Licensed Content Author	Ric Porteous,Danielle J. Moreau,Con J. Doolan
Licensed Content Date	Nov 1, 2014
Licensed Content Volume	51
Licensed Content Issue	n/a
Licensed Content Pages	15
Start Page	240
End Page	254
Type of Use	reuse in a thesis/dissertation
Intended publisher of new work	other
Portion	figures/tables/illustrations
Number of figures/tables/illustrations	1
Format	both print and electronic
Are you the author of this Elsevier article?	No
Will you be translating?	No
Original figure numbers	Figure 7
Title of your thesis/dissertation	FINITE EFFECTS ON TWO STAGGERED CYLINDERS IN A CROSS-FLOW
Expected completion date	Sep 2018
Estimated size (number of pages)	150
Requestor Location	University of Saskatchewan 69 Campus Drive Saskatoon, SK S7N 5B1 Canada Attn: University of Saskatchewan
Publisher Tax ID	GB 494 6272 12

ELSEVIER LICENSE
TERMS AND CONDITIONS

Aug 30, 2018

This Agreement between University of Saskatchewan -- Hayden Reitenbach ("You") and Elsevier ("Elsevier") consists of your license details and the terms and conditions provided by Elsevier and Copyright Clearance Center.

License Number	4418960137954
License date	Aug 30, 2018
Licensed Content Publisher	Elsevier
Licensed Content Publication	Journal of Fluids and Structures
Licensed Content Title	Two circular cylinders in cross-flow: A review
Licensed Content Author	D. Sumner
Licensed Content Date	Aug 1, 2010
Licensed Content Volume	26
Licensed Content Issue	6
Licensed Content Pages	51
Start Page	849
End Page	899
Type of Use	reuse in a thesis/dissertation
Portion	figures/tables/illustrations
Number of figures/tables/illustrations	3
Format	both print and electronic
Are you the author of this Elsevier article?	No
Will you be translating?	No
Original figure numbers	Figure 3, Figure 16, and Figure 34
Title of your thesis/dissertation	FINITE EFFECTS ON TWO STAGGERED CYLINDERS IN A CROSS-FLOW
Expected completion date	Sep 2018
Estimated size (number of pages)	150
Requestor Location	University of Saskatchewan 69 Campus Drive Saskatoon, SK S7N 5B1 Canada Attn: University of Saskatchewan
Publisher Tax ID	GB 494 6272 12

ELSEVIER LICENSE
TERMS AND CONDITIONS

Aug 30, 2018

This Agreement between University of Saskatchewan -- Hayden Reitenbach ("You") and Elsevier ("Elsevier") consists of your license details and the terms and conditions provided by Elsevier and Copyright Clearance Center.

License Number	4418960300958
License date	Aug 30, 2018
Licensed Content Publisher	Elsevier
Licensed Content Publication	Journal of Fluids and Structures
Licensed Content Title	Flow above the free end of a surface-mounted finite-height circular cylinder: A review
Licensed Content Author	D. Sumner
Licensed Content Date	Nov 1, 2013
Licensed Content Volume	43
Licensed Content Issue	n/a
Licensed Content Pages	23
Start Page	41
End Page	63
Type of Use	reuse in a thesis/dissertation
Intended publisher of new work	other
Portion	figures/tables/illustrations
Number of figures/tables/illustrations	1
Format	both print and electronic
Are you the author of this Elsevier article?	No
Will you be translating?	No
Original figure numbers	Figure 11
Title of your thesis/dissertation	FINITE EFFECTS ON TWO STAGGERED CYLINDERS IN A CROSS-FLOW
Expected completion date	Sep 2018
Estimated size (number of pages)	150
Requestor Location	University of Saskatchewan 69 Campus Drive Saskatoon, SK S7N 5B1 Canada Attn: University of Saskatchewan
Publisher Tax ID	GB 494 6272 12